Ball Milled Si-W Alloy Anode Materials for Lithium Ion Batteries

by

Yijia Liu

Submitted in partial fulfilment of the requirements
for the degree of Master of Science

at

Dalhousie University
Halifax, Nova Scotia
March 2018

TABLE OF CONTENTS

LIST OF TABLES ..... **iv**

LIST OF FIGURES ..... **v**

ABSTRACT ..... **viii**

LIST OF ABBREVIATIONS AND SYMBOLS USED ..... **ix**

ACKNOWLEDGEMENTS ..... **xi**

CHAPTER 1 INTRODUCTION **1**

1.1 LITHIUM-ION BATTERIES 2
1.2 NEGATIVE ELECTRODE MATERIALS 5
1.3 ALLOY ANODE MATERIALS 5
1.4 SI-BASED ANODE MATERIALS 13
1.4.1 Electrochemical Properties of Pure Si *13*
1.4.1.1 Alloying Mechanism of Li-Si 13
1.4.1.2 Fade Mechanism of Silicon 17
1.4.1.3 Two-Phase Regions 18
1.4.2 Si-containing Alloys *19*
1.5 MECHANICAL ALLOYING 20

CHAPTER 2 EXPERIMENTAL METHODS **22**

2.1 SAMPLE PREPARATION 22
2.1.1 Ball Milled Alloy Preparation *22*
2.2 CHARACTERIZATION TECHNIQUES 22
2.2.1 X-Ray Diffraction *22*
2.2.1.1. Theory 22
2.2.1.2 XRD Measurements 26
2.2.1.3 Quantitative Phase Analysis in XRD 26
2.2.1.4 XRD Quantification Method Used in The Current Study 28
2.2.2 Scanning Electron Microscopy and Energy Dispersive X-ray Spectroscopy *31*
2.2.3 Electrochemical Methods *32*
2.2.3.1 Cell Construction 32
2.2.3.2 Electrochemical Tests 34

CHAPTER 3 BALL MILLED SI-W ALLOYS **37**

3.1 INTRODUCTION 37
3.2 XRD CHARACTERIZATION 37

3.2.1 X-Ray Diffraction Patterns *37*
3.2.1.1 XRD Patterns of Si-W Alloys as A Function of Milling Time 37
3.2.1.2 Caking Investigation Using XRD 39
3.2.2 Quantitative X-Ray Phase Analysis *40*
3.2.3 Model *43*
3.2.4 Simulation Results *50*
3.3 SEM IMAGES 53
3.4 CONCLUSION 55
CHAPTER 4 SI-W ALLOY ANODE MATERIALS FOR LITHIUM ION BATTERIES. 56
4.1 AN OVERVIEW OF THE ELECTROCHEMICAL PERFORMANCE OF SI-W ALLOYS 56
4.2 ELECTROCHEMICAL PERFORMANCE OF ALLOYS AT FIXED MILLING TIME 61
4.3 ELECTROCHEMICAL PERFORMANCE OF ANNEALED SAMPLES 65
4.4 CONCLUSION 72
CHAPTER 5 CONCLUSIONS AND FUTURE WORK 73
5.1 CONCLUSION 73
5.2 FUTURE WORK 74
5.2.1 Comparisons to Other Si-M Systems *74*
5.2.2 Investigation of Contamination *78*
5.2.3 $Si_{100-x}W_x$ Alloy Optimization *79*
5.2.4 Furthering the Understanding of Si Alloy Electrochemistry *80*
REFERENCES 82
APPENDIX I 89
APPENDIX II 103

LIST OF TABLES

Table 3.1 Fitting parameters used in the simulation for $Si_{100-x}W_x$ alloys. 53

LIST OF FIGURES

Figure 1.1 Schematic of electrochemical process in a Lithium ion cell, with a $LiMO_2$ (metal oxide material) positive electrode and a graphite negative electrode. 3

Figure 1.2 Specific and Volumetric capacities of Li alloys compared to LiC_6. The volumetric capacities were calculated based on the fully lithiated volume. 6

Figure 1.3 The volumetric energy density (vs a 3.75 V cathode) of Li alloys at a 100% volume expansion.. 7

Figure 1.4 Structural model of Sn-Co-C material. 9

Figure 1.5 Left panel: Specific capacity versus cycle number for $Sn_{30}Co_{30}C_{40}$ electrodes: (a) combinatorially sputtered film, (b) attritor milled $CoSn_2$ + Co + graphite, and (c) attritor milled CoSn + graphite. 11

Figure 1.6 First discharge, charge, and second discharge for a cell made from ground pure silicon. 14

Figure 1.7 Voltage curve of a crystalline silicon electrode cycled in a way to illustrate the electrochemical conversion of crystalline silicon to amorphous silicon, amorphous silicon to crystalline $Li_{15}Si_4$, and $Li_{15}Si_4$ back to amorphous silicon. 15

Figure 1.8 Voltage vs. composition plot for a Si/Li cell undergoing pre-conditioning cycles and CCCV cycling as described in Reference [15] 16

Figure 1.9 Cell failure mechanism of silicon. 18

Figure 2.1 Schematic diagram of the Bragg-Brentano diffractometer, shown with divergent slits, antiscatter slits and receiving slits. 25

Figure 2.2 Schematic diagram of Bragg diffraction from crystalline planes in a solid.. .. 25

Figure 2.3 XRD pattern of the 4 h milled $Si_{80}W_{20}$ sample and the fitted pattern with contributions from amorphous Si, Si_2W, and W phases indicated. 29

Figure 2.4 Flow chart of the quantitative XRD pattern analysis procedure. 30

Figure 2.5 A Schematic diagram of 2325-type coin cell assembly. 33

Figure 3.1 XRD patterns of ball milled $Si_{85}W_{15}$, $Si_{80}W_{20}$, $Si_{75}W_{25}$, and $Si_{70}W_{30}$ as a function of milling time. 38

Figure 3.2 Example of caking in the $Si_{70}W_{30}$ sample. 40

Figure 3.3 The amount of constituent alloy phases (error bars based on the standard deviation of 3 - 6 replicates of fitting) for different Si-W alloys as a function of milling time as determined by quantitative XRD phase analysis. 42

Figure 3.4 Average crystallite size calculated by Scherrer equation of the Si-W alloys as a function of milling time. 43

Figure 3.5 Scheme diagram of proposed model of mechanical alloying. 45

Figure 3.6 Simulated Si phase evolution curves using same impact zone size (N = 20), same energy gained per hit: reaction energy barrier ratio ($\Delta E/E^* = 0.5$), but with different hit event frequencies ($\nu = 500\ h^{-1}$, $1000\ h^{-1}$, $3000\ h^{-1}$, $5000\ h^{-1}$ and $20000\ h^{-1}$). 47

Figure 3.7 Simulated Si phase evolution curves using same impact zone (N = 20) and same frequency of each hit event ($\nu = 1000\ h^{-1}$), but with different energy gained per hit: reaction energy barrier ratios ($\Delta E/E^* = 0.10, 0.15, 0.20, 0.50$ and 1.00). 48

Figure 3.8 Simulated Si phase evolution curves using the same frequency of each hit event ($\nu = 1000\ h^{-1}$) and same energy gained per hit: reaction energy barrier ratio ($\Delta E/E^* = 0.5$), but with different impact zone sizes (N = 9, 20, 50, 100, and 2000). 49

Figure 3.9 The volume percent Si phase as a function of milling time for different Si-W compositions as determined experimentally and calculated from the model described in the text. 52

Figure 3.10 SEM images of $Si_{85}W_{15}$ at different milling times. (a) 1 h, (b) 2 h, (c) 4 h and (d) 8 h. 54

Figure 3.11 (a) SEM image of the 4 h milled $Si_{80}W_{20}$ sample and corresponding EDS compositional mapping images of (b) Si and (c) W. 54

Figure 4.1 Voltage versus capacity curves of ball milled $Si_{85}W_{15}$, $Si_{80}W_{20}$, $Si_{75}W_{25}$ and $Si_{70}W_{30}$ at different milling times. 57

Figure 4.2 The first lithiation and delithiation capacities (error bars based on the standard deviation of 3-6 replicates) of all $Si_{100-x}W_x$ alloy compositions prepared at different milling times. 58

Figure 4.3 Differential capacity curves of the cells shown in Figure 4.1. 60

Figure 4.4 Specific capacity of ball milled $Si_{100-x}W_x$ versus cycle number, milling hours are indicated in different colors. 61

Figure 4.5 Volumetric capacity of ball milled $Si_{100-x}W_x$ versus cycle number, milling hours are indicated in different colors. 61

Figure 4.6 Voltage and differential capacity curves of 4 h ball milled $Si_{100-x}W_x$ (x = 15, 20, 25 and 30) alloys. 63

Figure 4.7 The first lithiation and delithiation capacities (error bars based on the standard deviation of 3-6 replicates) of 4 h milled $Si_{100-x}W_x$ (x = 15, 20, 25 and 30) alloys as measured in coin cells. 64

Figure 4.8 Specific (top) and volumetric (bottom) capacity of 4 h ball milled $Si_{100-x}W_x$ (x = 15, 20, 25, and 30) versus cycle number. 64

Figure 4.9 XRD patterns of 4 h milled $Si_{85}W_{15}$, $Si_{80}W_{20}$, $Si_{75}W_{25}$, and $Si_{70}W_{30}$ alloys as milled and after thermal annealing at 600°C and 800°C. Known phase peak positions and intensities are indicated by vertical lines. 66

Figure 4.10 Voltage curves of 4 h milled $Si_{85}W_{15}$, $Si_{80}W_{20}$, $Si_{75}W_{25}$, and $Si_{70}W_{30}$ alloys as milled and after thermal annealing at 600°C and 800°C. 67

Figure 4.11 Differential capacity as a function of voltage for the alloys shown in Figure 4.10 68

Figure 4.12 The first lithiation and delithiation capacities (error bars based on the standard deviation of 3-6 replicates) of Si-W alloys under different temperature treatments as measured in coin cells. 70

Figure 4.13 Specific capacity versus cycle number of alloys as milled and after annealing to 600°C and 800°C 71

Figure 4.14 Cycling performance (volumetric capacity) of alloys as milled and after annealing to 600°C and 800°C 71

Figure 5.1 XRD patterns of unheated, 600°C annealed and 800°C annealed 4 h milled $Si_{80}Fe_{20}$. 75

Figure 5.2 XRD patterns of unheated, 600°C annealed and 800°C annealed 4 h milled $Si_{80}W_{20}$. 76

Figure 5.3 Electrochemical performance of 4 h milled $Si_{80}Fe_{20}$, 600°C annealed and 800°C annealed 4 h milled $Si_{80}Fe_{20}$ (From left to the right: voltage curves, differential curves, and cycling performance). 77

Figure 5.4 Electrochemical performance of 4 h milled $Si_{80}W_{20}$, 600°C annealed and 800°C annealed 4 h milled $Si_{80}W_{20}$ (From left to the right: voltage curves, differential capacity curves, and cycling performance). 77

ABSTRACT

Si-based materials are excellent alternatives to conventional graphite anodes because of their high theoretical capacity and high earth abundance. This thesis explores the electrochemical and structural characteristics of Si-W alloy anode materials prepared by ball milling. X-Ray diffraction was used to characterize the microstructure of the Si-W alloys and for quantitative phase characterization during the ball milling process. Analysis of phase behavior allowed for a model to be developed to explain the milling process. Electrochemical measurements were used to investigate if the addition of W to Si improves cycling performance and suppresses $Li_{15}Si_4$ formation. The voltage and differential capacity curves of the $Si_{100-x}W_x$ alloys were typical of Si-based alloys, and Si was determined to be the only active phase. Measured capacities agreed with those predicted from quantitative X-ray analysis. The Si-W alloys were found to have high thermal stability, which enables high-temperature processing while maintaining a nanostructured morphology.

LIST OF ABBREVIATIONS AND SYMBOLS USED

a-Si	Amorphous Silicon
at. %	Atomic Percent
BSE	Backscattered Electrons
C	C as in C-rate
CCCV	Constant Current, Constant Voltage
CE	Coulombic Efficiency
d	Atomic Plane Spacing
DEC	Diethyl Carbonate
DMC	Dimethyl Carbonate
EC	Ethylene Carbonate
EDS	Energy Dispersive Spectrometry
f	Fraction of W Unavailable for the Reaction
FEC	Fluoroethylene Carbonate
FWHM	Full Width at Half Maximum
h	Hours
I	Intensity
Kα	Relative Intensity Ratio Value of α phase
LiPAA	Lithium Polyacrylate Acid
MA	Mechanical Alloying
Mα	Weight Fraction of α phase
N	Size of the Impact Zone

RIR	Relative Intensity Ratio
SE	Secondary Electrons
SEI	Solid Electrolyte Interface
SEM	Scanning Electron Microscopy
t	Time
V	Voltage
ν	Frequency
V_{si} %	Volume Percent of Silicon
W*	Inactive Tungsten
wt.%	Weight Percent
XRD	X-Ray Diffraction
Xα	Mole Fraction of α phase
λ	Wavelength of Radiation
θ	Scattering Angle in XRD
ρ	Density
ΔE/E*	Energy Gain Per Hit : Reaction Energy Barrier Ratio

ACKNOWLEDGEMENTS

Completing this thesis was one the most challenging things I've ever done, so I have so many people I want to acknowledge.

First, I would like to acknowledge my parents in China for their endless support in the past two and a half years.

I wish to express my very great appreciation to my thesis supervisor and coworkers:

To Dr. Mark Obrovac, for his valuable and constructive suggestions during the planning and development of this thesis project. His willingness to offer his time so generously has been very much appreciated.

To Dr. Timothy David Hatchard for being kind and supportive to me. His willingness to help me fix the SPEX mill and the X-ray machine was much appreciated.

To Dr. Jeff Dahn, for using his instruments and being an inspirational professor. His battery lectures were always amazing and helpful.

To Simeng, Yidan, Yukun, and Ben for constructive discussions of alloys projects.

To my friends Quan Kong and Yingda Guo, for helping me with the programming.

To 3M company and NSERC for funding.

Finally, I would like to thank all my coworkers in the Obrovac lab.

CHAPTER 1 INTRODUCTION

Batteries are devices that convert chemical energy into electrical energy through electrochemical redox reactions. There are two major types of batteries, primary and secondary. Primary batteries are based on an irreversible electrochemical redox reaction. They cannot be reused once fully discharged. That's why they also are known as disposable batteries. Alkaline batteries and zinc/air batteries are examples of this type of battery. They have been applied in hearing aids, lighting, digital cameras, toys, global positioning system devices, and other applications [1]. Secondary batteries, however, can be reused via reversible reactions. Many applications of the primary batteries have been rapidly replaced by secondary batteries (such as cameras and global positioning system devices). Active materials can be regenerated via charging so that the battery can be discharged again. Lithium-ion, lead-acid and nickel-metal hydride batteries are currently the most common rechargeable batteries that are commercially available. Applications of secondary batteries are grid energy storage, hybrid electric vehicles, and some portable devices such as cell phones, laptop computers, and power tools [1]. The lithium-ion battery will be discussed in this thesis with a particular focus on anode materials. Si-based anode materials are promising candidates as alternatives to graphite because of their higher theoretical capacity and high earth abundance. However, Si-based alloys suffer from huge volume changes during the lithiation/delithiation process, which can result in capacity fade. With the hope to suppress the volume expansion and further increase the energy density at a given volume, $Si_{100-x}W_x$ alloys were studied in this thesis. $Si_{100-x}W_x$ alloys were also expected to have good thermal stability because of the high melting point of tungsten disilicide (2164°C) [2].

This thesis describes the preparation, characterization, and use of ball milled $Si_{100-x}W_x$ negative electrodes in Li-ion batteries. As an outline of the thesis: Chapter 1 gives a brief introduction to lithium-ion batteries, mainly focusing on negative electrode materials. Chapter 2 outlines the experimental techniques used in this work, including material preparation and characterization. Chapter 3 describes the phase evolution, phase composition and grain size of Si-W alloys during the ball milling process. This milling process was simulated by using a constant volume element model in which the milling reactions are assumed to be activated processes in which energy is accumulated after every collision. Chapter 4 focuses on the electrochemical performance and thermal stability of the ball-milled $Si_{100-x}W_x$ system in detail. Finally, Chapter 5 summarizes the negative electrode materials examined in this thesis and future work in the related area is suggested.

1.1 Lithium-Ion Batteries

Secondary lithium-ion batteries are utilized worldwide. They have significant advantages over other battery types, such as high energy density (~700 Wh/L), long cycle life (>1000 cycles), rapid charge capability, low self-discharge rate and high coulombic efficiency [3–6]. Typical applications of lithium-ion batteries include power sources in cell phones, laptops, digital cameras, power tools, electric bikes, and military devices.

Lithium-ion batteries are comprised of a cathode and an anode separated by an electrolyte containing separator, as shown in Figure 1.1. Lithium transition metal oxides, such as the spinel phase $LiMn_2O_4$, layered $LiCoO_2$, $LiNi_xMn_yCoO_2$ (NMC), and $LiNi_{0.8}Co_{0.15}Al_{0.05}O_2$ (NCA), or lithium metal phosphates, such as $LiFePO_4$, are commonly used cathode materials, while graphite is the most common anode material [1][7,8]. A porous membrane separator is typically used to

separate the positive and negative electrodes. The use of a separator prevents electric short circuits, minimizes the electrolyte usage and increases the structural integrity of the batteries. Non-aqueous liquid electrolytes are commonly used in lithium-ion cells. These are solutions of a lithium salt in organic solvents, typically carbonates [9]. Lithium hexafluorophosphate ($LiPF_6$) is commonly used as the lithium salt due to its high ionic conductivity (10^{-2} S/cm) in carbonate solvents and high lithium ion transference number ($\approx$ 0.35) [1] [10]. Organic electrolyte solvents normally consist of ethylene carbonate (EC) and a linear carbonate, such as diethyl carbonate (DEC) or dimethyl carbonate (DMC). The electrolyte works as a medium to transport lithium ions back and forth between the positive electrode and the negative electrode.

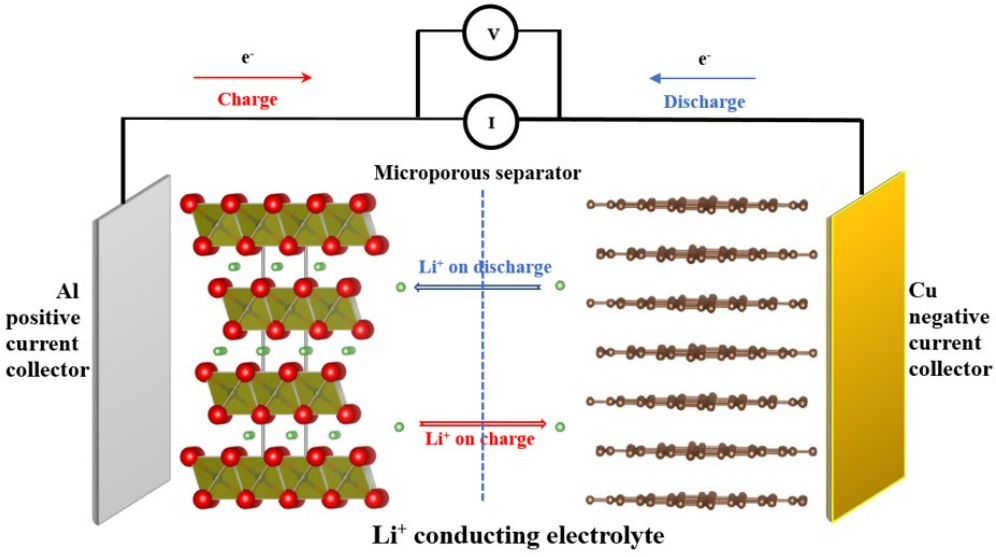

Figure 1.1 Schematic of electrochemical process in a Lithium ion cell, with a $LiMO_2$ (metal oxide material) positive electrode and a graphite negative electrode. Red, blue, green, and brown spheres represent oxygen, transitional metal, lithium, and carbon atoms, respectively.

In Figure 1.1 graphite and $LiMO_2$ are active materials. $LiMO_2$ represents a metal oxide positive material, where M is typically Co or combinations of Co, Ni, and Mn. Besides, M can also contain some Al or Li. In these active materials, lithium ions can be reversibly incorporated in an intercalation/deintercalation process. When a Li-ion battery is charged, the active positive electrode is oxidized, the Li-ions are removed from the cathode, and together with electrons, flow into the anode through different routes. The active negative material gets reduced due to the flow of electrons. In this process, Li ions are extracted from $LiMO_2$ and insert into graphite. Upon discharge, Li-ions travel from a higher energy state in the graphite anode to a lower energy state in the cathode, through the electrolyte while transition metal ions in the cathode are reduced. The electrons released from the anode transfer through the external circuit to the cathode to balance the charge. The resulting current flow in the external circuit can be used to do useful work. In the intercalation/deintercalation process, no significant structural change occurs in the $LiMO_2$ or graphite hosts because graphite negative electrode materials have a layered structure and $LiMO_2$ positive electrode materials have either a tunneled or a layered structure that can incorporate lithium ions without significant structural distortion. These spontaneous reactions are driven by a chemical potential difference between the negative and positive electrodes. The resulting working potential, V, can be expressed as:

$$V = -\frac{(\mu_{cathode} - \mu_{anode})}{ne}$$

where e is the charge of an electron, n is the number of electrons taking part in the reaction, and $\mu_{cathode}$ and μ_{anode} are the chemical potentials of the positive and the negative electrodes with respect to lithium, respectively, in electron volts (eV).

Developments in lithium-ion batteries have been focused on improvements in performance (cycle life, rate capability, coulombic efficiency (CE), safety properties, etc.) and increased energy density, mainly via improvements in electrodes and electrolytes. Properties, such as high capacity, a stable structure where lithium could reversibly insert/extract, low production cost, high electronic conductivity, high lithium ion diffusivity, and compatibility with other components, are desired when developing new electrode materials. This thesis' focus is on negative electrodes.

1.2 Negative Electrode Materials

Lithium metal was used as the negative electrode in the 1980s because of the high capacity of lithium metal. However, safety issues have essentially stopped the use of lithium metal as a rechargeable battery electrode. In addition, changes in the morphology of lithium during cycling increases its surface area, leading to poor columbic efficiency [1].

On the other hand, graphite offers stable surface morphology, together with high specific capacity, high volumetric capacity, low average voltage, low voltage hysteresis, good rate capability, low volume expansion, good cycle life, high coulombic efficiency, good electronic conductivity, high abundance and affordable cost. These properties make it an almost ideal anode material [11]. For these reasons, graphite plays a major role in today's lithium-ion battery industry.

1.3 Alloy Anode Materials

In order to improve Li-ion batteries, extensive research has been on anode material to find good alternatives to carbonaceous electrodes. Alloy anodes used as alternatives to carbonaceous electrodes are expected to increase the energy density of lithium-ion batteries and are anticipated to be incorporated the next generation of Li-ion batteries.

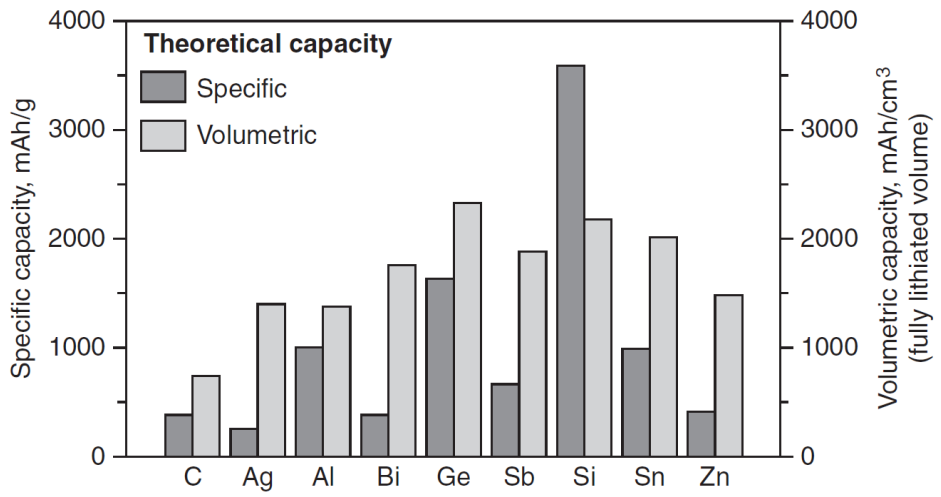

Figure 1.2 Specific and Volumetric capacities of Li alloys compared to LiC_6. The volumetric capacities were calculated based on the fully lithiated volume. Reproduced with permission from Reference [1], Copyright 2011 McGraw-Hill.

Figure 1.2 shows the specific and volumetric capacities of various Li-metal alloys compared to graphite. This figure illustrates why alloy-based negative electrode materials are promising and list some good candidate elements to be studied. Concerning specific capacity, Si is far ahead of the other metals and the next is Ge with a gravimetric capacity of around 1600 mAh/g. Si is abundant in the Earth's crust, giving it a significant advantage over others. However, the difference amongst the elements is less with respect to volumetric capacity. Ge is slightly higher in volumetric capacity than Si, while Si is the next highest, with a volumetric capacity around 2194 Ah/L, Sn and Sb are not far behind the volumetric capacity of Si. Therefore, in the search for higher volumetric and gravimetric capacities, Sn and Si seem to be the main elements to focus on. Each of the alloys shown in Figure 1.2 has higher volumetric capacity than graphite. High capacity,

abundance, cost, voltage window and low toxicity are also of great importance when selecting the right elements to study [12].

It is worth noting that because all alloys undergo large volume expansion (up to 280%) during lithiation, it is essential to consider the tradeoff between the benefit of having increased energy density vs. alloy volume expansion in a full cell. Figure 1.3 shows the energy density at 100% volume expansion for selected elements calculated in a full cell. The energy density for each element in this figure is about the same at the given volume expansion [13]. The maximum improvement in the energy density of full cells with alloy anodes compared to graphite is about 20% [11]. This energy increase is deemed a significant enough incentive to encourage researchers to solve the problems associated with alloy volume expansion.

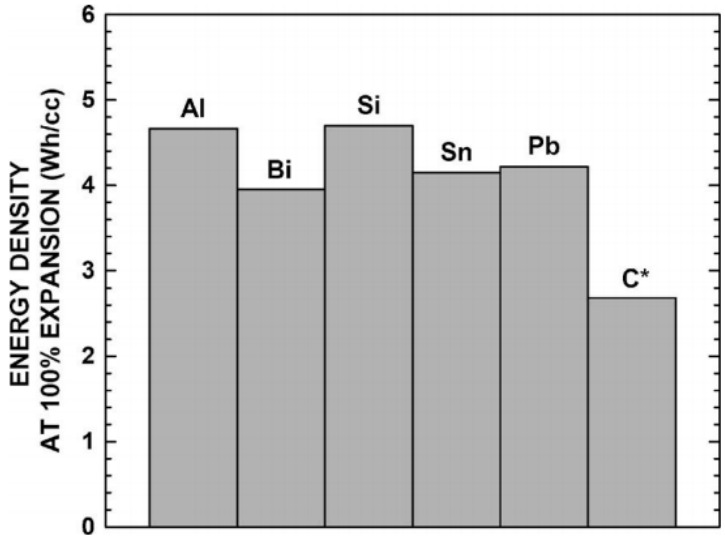

Figure 1.3 The volumetric energy density (vs a 3.75 V cathode) of Li alloys at a 100% volume expansion. *Carbon expands by 10% during lithiation, it is included for comparison. Reproduced with permission from Reference [13], Copyright 2007 The Electrochemical Society.

Issues regarding electrode material design and electrode design need consideration to accommodate the volume expansion problem. A review from Todd *et al.* [14] and papers by Obrovac et al. [11,13,15] provide approaches to optimize electrode materials and electrodes using Sn-based Si-based alloys, respectively. Silicon suboxide (SiO_x) is another promising material being widely studied because of its high capacity. SiO_x is composed of nano-silicon grains in a matrix of SiO_2 [16]. The drawback of SiO_x is its high irreversible capacity loss (~50%) which is due to the formation of lithium silicates during its initial lithiation [17]. As a pre-lithiation method, stabilized lithium metal powder (SLMP) can be added to the negative electrode to compensate first-cycle irreversible capacity loss from materials like SiO_x [18].

Nanometer-sized Si and Sn-based negative electrode materials suffer from the high specific surface area and thus cause large irreversible capacity and related safety issues. The high surface area of nanosized Si materials increases the possibility of chemical reactions with electrolytes. For example, after the decomposition of a commonly used electrolyte $LiPF_6$, the resulting HF can react with Si, making the active Si network become electrochemically inactive, which is undesired in a good anode material [19][20]. Instead, nanostructured materials, such as alloys or SiO_x, which comprise micron-size particles made up of nanometer-size grains of electrochemically active and inactive materials, are found to be very useful [1]. Two commonly used approaches in optimizing negative electrode are (1) to incorporate single element alloys (Si, Sn) with carbon (carbon could provide electronic conductivity and further buffer volume expansion); (2) make Si or Sn-based $M_xSn(Si)/C$ composites, forming a nanocomposite that is made of electrochemically active species surrounded by inactive phases. The second method was applied in the commercialized Nexelion battery. Nexelion utilizes a carbon negative electrode with a high portion of the Co-Sn-based

material. The Nexelion battery achieved a 25% increase in volumetric energy compared to conventional cells with graphite negative electrodes [12].

The Sony Nexelion cell utilized a nanostructured alloy material. Figure 1.4 shows the proposed nanostructure of the Sn-Co-C negative electrode material, which is considered to comprise nanometer-size Co-Sn grains dispersed in a carbon matrix [1]. This proposed nanostructure has been confirmed by TEM [21] and small angle neutron scattering studies [22].

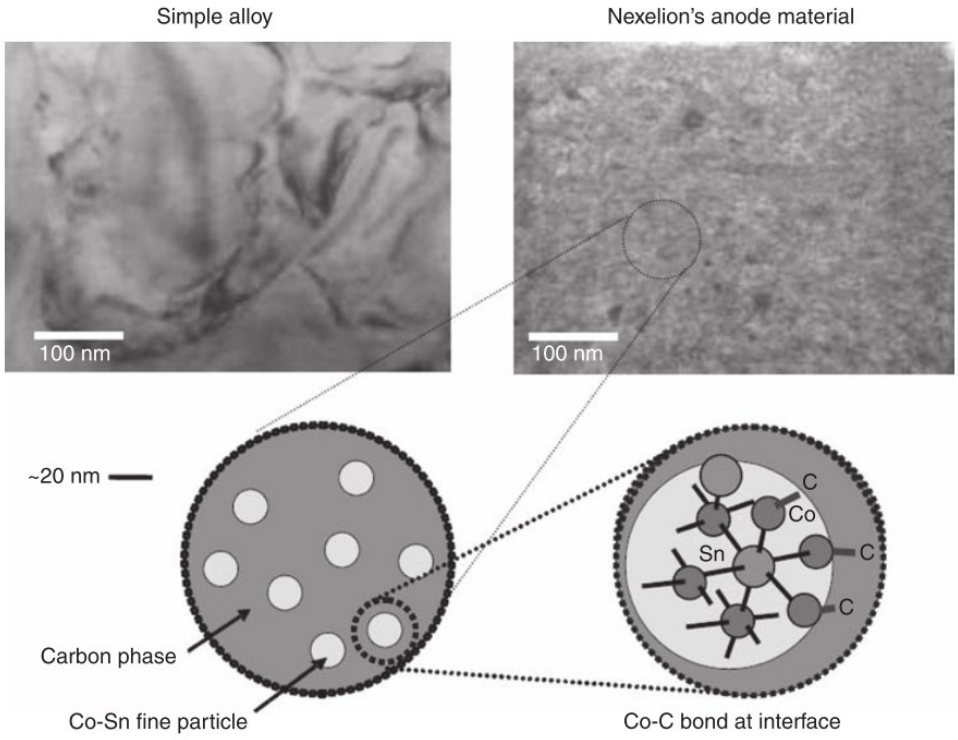

Figure 1.4 Structural model of Sn-Co-C material. Reproduced with permission from Reference [1], Copyright 2011 McGraw-Hill.

Although Sony did not reveal the exact composition of the Sn-Co-C composite, Todd *et al.* used magnetron sputtering or mechanical attrition to prepare $Sn_{30}Co_{30}C_{40}$, which had a

nanostructure similar to the commercial one [14]. The choice of Sn and C is obvious and easy to understand, while the choice of cobalt is interesting. Co is an expensive raw material. Thus there must be a reason behind this use in commercial cells [11]. Co is considered as the ideal transition metal for the Sn-TM-C composition system [23]. According to Todd's study on sputtered Sn-M (M = Ti, V, Cr, Mn, Fe, Co, Ni, Cu) libraries, only Ti, V, Cr, and Co result in amorphous structures [24]. Amorphous microstructures are desirable during alloy cycling, and transition metals which could not give amorphous regions are thus less desirable [11]. The aggregation of Sn during cycling can occur in all Sn-TM alloys. Carbon was introduced to inhibit Sn aggregation, resulting in ternary $Sn_{1-x-y}M_xC_y$ (M = Ti, V, and Co) ($0<x<0.5$ and $0<y<0.5$) combinatorial libraries [20]. However, it was found from the XRD studies that when M = Ti and V, the addition of carbon will cause the precipitation crystalline Sn. When M = Co, no formation of crystalline Sn could be observed after the addition of carbon. Sn-Co-C alloys were found have stable differential capacities during cycling, and their amorphous microstructures were maintained with no Sn agglomeration observed. Furthermore, the phase diagrams of the M-C systems indicate that Co is the only transition metal that does not form stable carbides among Ti, V, Cr, and Co. Cobalt in the Sn-Co-C composites helps to keep the amorphous structure (no formation crystalline Sn and carbides) while diluting the volume expansion. The presence of carbon offers a stable matrix and adds some extra capacity as well [23].

Figure 1.5 shows cycling results of three Li/$Sn_{30}Co_{30}C_{40}$ coin cells and potential versus specific capacity curves of the same cells. The $Sn_{30}Co_{30}C_{40}$ materials were prepared by three different methods as specified in the caption. The material prepared by sputtering has a grain size about 1 nm and provide a reversible capacity of about 610 mAh/g [14]. Materials prepared by mechanical

methods can have a specific capacity of about 400 to about 500 mAh/g and good capacity retention, depending on the preparation method, as shown in Figure 1.5. The attrited materials have densities (measured by He pycnometry) of about 6.5 g/mL and have high volumetric capacity. The difference in the observed capacities for the three cells correlate with the grain size of the Co-Sn grains prepared through different synthesis methods. The voltage curves of all three cells are characteristics of single-phase lithiation/delithiation.

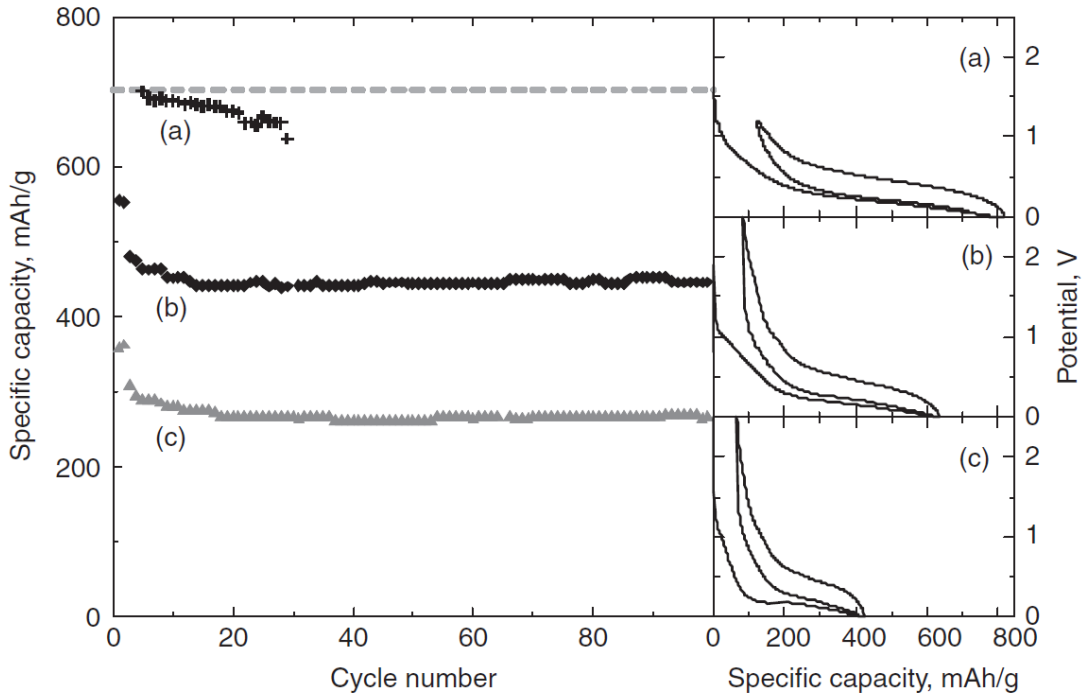

Figure 1.5 Left panel: Specific capacity versus cycle number for $Sn_{30}Co_{30}C_{40}$ electrodes: (a) combinatorially sputtered film, (b) attritor milled $CoSn_2$ + Co + graphite, and (c) attritor milled CoSn + graphite. Right panel: Potential versus specific capacity of the first cycle for samples described in the left panel of this figure. Electrodes formulations were: 80% attrited powder, 12% conductive carbon black, and 8% binder. Testing was done at 30°C. Reproduced with permission from Reference [14], Copyright 2010 Wiley.

Tian *et al.* reported that the volume expansion of $Sn_{30}Co_{30}C_{40}$ during lithiation is about 150% at its full theoretical specific capacity [25]. It is believed that Sony adds about 50% by weight of graphite to the negative electrodes to further dilute this large volume change. In addition, special electrolyte additives, like fluoroethylene carbonate (FEC), and special binder materials are required to form a solid electrolyte interphase (SEI) that is stable on the $Sn_{30}Co_{30}C_{40}$ particle surfaces under such large volume changes [26]. Ferguson et al. indicated that it is possible to replace about 50% of the Co by Fe in these materials without having negative effects on cell performance. The production cost could be therefore reduced by partially replacing the expensive Co raw material [27].

3M company has claimed that their Si-based anode material can increase the energy density of commercial cells by more than 20% and show long cycle life with paired cathodes and optimized cell designs [11,28]. The main challenge for researchers who work on alloy negative materials is to exploring better alloy negative electrode materials, not to mention the development in other battery components, including better binders, better conductive additives, better electrolytes and better electrolyte additives. There are lots of possible elements that could be alloyed with Si and/or Sn, with lots of possible resulting nanostructures. Maintaining a low production cost is also key to make alloy anode material competitive with graphite. The Si-W alloys studied here are worth exploring in order to gain a better understanding of all Si-M systems.

1.4 Si-Based Anode Materials

1.4.1 Electrochemical Properties of Pure Si

1.4.1.1 Alloying Mechanism of Li-Si

Unlike the intercalation/ deintercalation process between graphite and Li, the reaction between Li and Si follows an alloying mechanism, Li forms alloys with Si, involving bond breaking between host atoms and drastic structural changes [29]. This results in large volume expansion/contraction during lithiation/delithiation. Alloys may also undergo multiple crystallographic phase transitions during lithiation. As a result, large amounts of capacity fade can occur in just a few cycles, as shown in Figure 1.6. Pure Si can reach a capacity close to 3000 mAh/g during the first lithiation, with a low average voltage, large hysteresis, and low delithiation capacity [30].

The electrochemistry of bulk Si has been studied by Obrovac *et al.* [15,31]. In 2004, Obrovac and Christensen performed a detailed *ex situ* X-ray diffraction (XRD) study on the electrochemical reaction of lithium with silicon [31]. They confirmed the transition from crystalline Si to an amorphous structure upon lithiation and discovered the formation of crystalline $Li_{15}Si_4$ below 50 mV. This was an important finding because $Li_{15}Si_4$ is a metastable phase not present in the Li-Si phase diagram and only appears during electrochemical cycling. In a later study, Li and Dahn performed an *in-situ* XRD study on crystalline Si negative electrodes to study the electrochemical alloying mechanism of crystalline and amorphous Si with lithium and provided a detailed phase diagram during lithiation and delithiation [32]. Li *et al.* utilized ^{119}Sn Mössbauer spectroscopy to further understand the electrochemical reaction between a-Si and Li using Sn as probe atom [33]. It was found that the two sloping plateaus in the discharge profile correspond to two arrangements of Li atoms in the host structure. The higher voltage plateau is a result of Li-ions being inserted

into environments where each Li has Si neighbors primarily. While at lower voltages, the Li atoms have Li neighbors primarily, meaning that their insertion voltage will be closer to that of Li-plating (occurring at 0 V vs. Li). The current understandings of Li-Si electrochemistry could be summarized in a Si voltage curve in Figure 1.7.

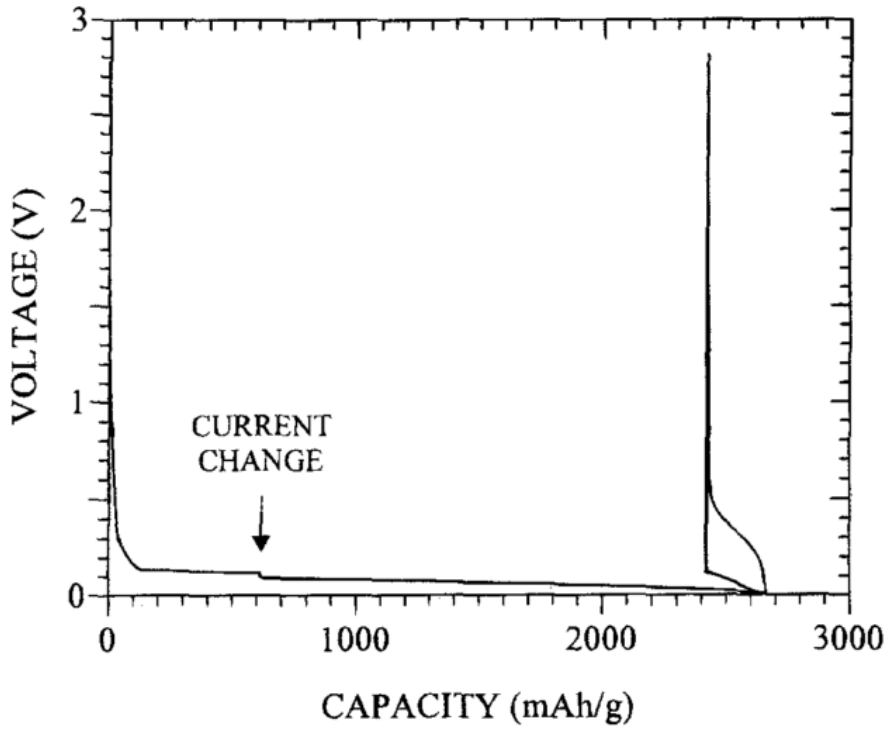

Figure 1.6 First discharge, charge, and second discharge for a cell made from ground pure silicon, Reproduced with permission from Reference [34], Copyright 1995 The Electrochemical Society.

As crystalline silicon is lithiated, it turns into amorphous Li_xSi (*a*-Li_xSi, I in Figure 1.7) in a two-phase region with a potential of about 70 mV, if the voltage proceeds below 50 mV, the *a*-Li_xSi will crystallize to form $Li_{15}Si_4$ (II in Figure 1.7). During the first charge, $Li_{15}Si_4$ is delithiated to form amorphous Li_xSi, a plateau at about 0.43 V is observed because of this two-phase region. At higher voltages, the amorphous Li_xSi is completely delithiated to form a-Si. In the following discharge, if the cut-off voltage is above 50 mV, silicon will remain amorphous, and a single phase

region was observed (IV in Figure 1.7), the reversible process is observed as V in Figure 1.7, showing the delithiation process of amorphous lithiated silicon [31][32]. VII and VII in Figure 1.7 are the two sloping plateaus during the lithiation of amorphous Si, as carefully studied by Mössbauer spectroscopy in Reference [33], the first sloping plateau at higher potential represents the Li-Si neighbors filling while the second corresponds to Li-Li neighbors filling. Again, if the lithiation voltage goes below 50 mV, crystalline $Li_{15}Si_4$ forms and a plateau will appear during the next delithiation voltage curve.

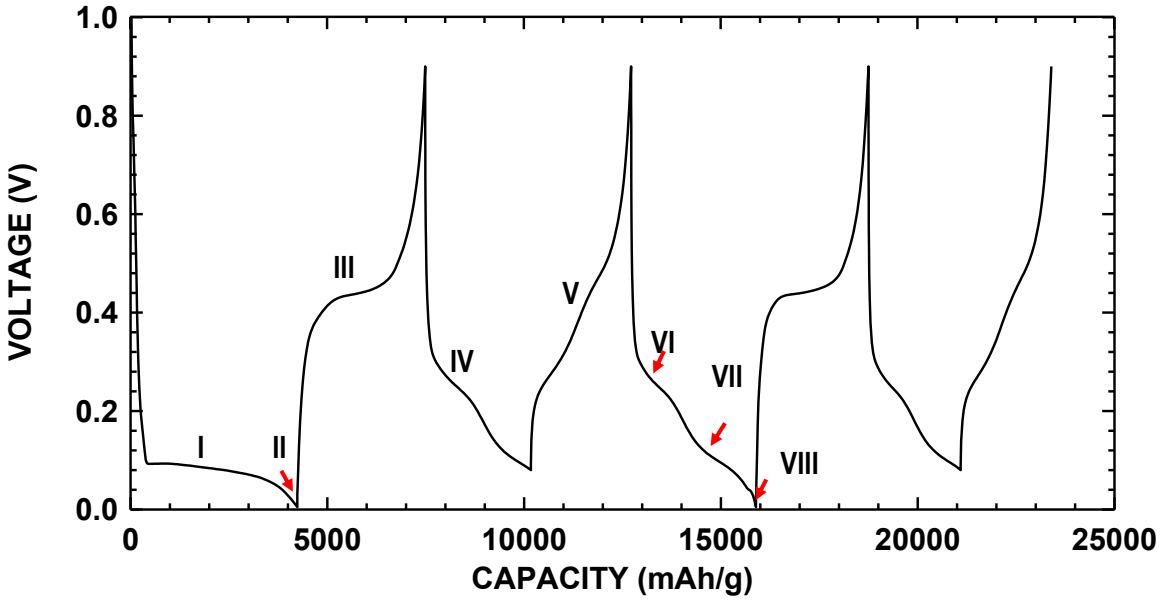

Figure 1.7 Voltage curve of a crystalline silicon electrode cycled in a way to illustrate the electrochemical conversion of crystalline silicon to amorphous silicon, amorphous silicon to crystalline $Li_{15}Si_4$, and $Li_{15}Si_4$ back to amorphous silicon. Reproduced with permission from Reference [15]. Copyright 2013 The Electrochemical Society.

The significant volume expansion (fully lithiated Si expands by 280%) of alloy negative electrodes upon lithiation makes it difficult to implement them in commercial cells. Active alloys undergo mechanical stress during lithiation with huge and repeated volume changes during

subsequent cycling. As a result, alloy particles can become pulverized with repeated cycling, leading to cell fade [15]. Obrovac and Krause demonstrated that a discharge voltage limit (0.17 V *vs.* Li^+/Li^0) of bulk crystalline Si can limit the amount of reacted Si [15]. The non-reacted Si remains crystalline during the following lithiation/delithiation process, and the volume expansion of the reacted Si part can be limited to values at which advanced polymeric binders can withstand, so that electrical contact between particles and the current collector can be maintained. This voltage limit also restricts cycling to only occur in a single-phase region. Good cycling performance was observed (900-1000 mAh/g) over 100 cycles (Figure 1.8). This approach was considered as the *in situ* creation of non-reacted substrate (inner crystallized Si) that limits the loss of integrity of an active Si layer [12]. This cycling strategy is useful, illustrating that large crystallized Si particles can still maintain good cycling performance [12].

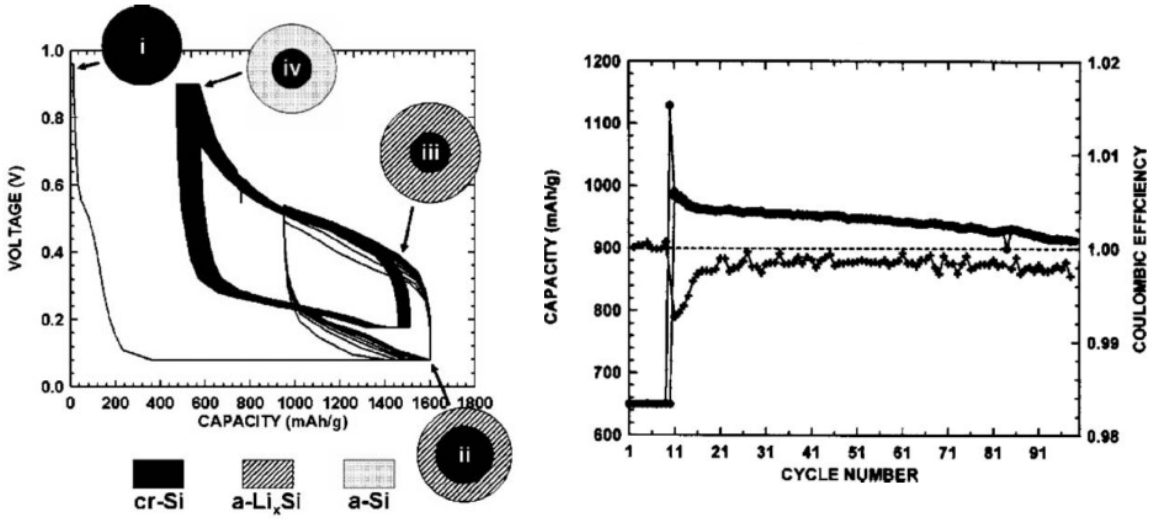

Figure 1.8 Voltage vs. composition plot for a Si/Li cell undergoing pre-conditioning cycles and CCCV cycling as described in Reference [15] and corresponding capacity (circles)/coulombic efficiency (cross) as

a function of the cycle number. Reproduced with permission from Reference [15]. Copyright 2013 The Electrochemical Society.

1.4.1.2 Fade Mechanism of Silicon

It is essential to understand the fade mechanism of Si anodes. Reference [35] proposes three possible mechanisms to explain the cell failure initiating from volume expansion, including pulverization, delamination and an unstable SEI layer. A schematic diagram of the cell failure mechanism is shown in Figure 1.9 and is explained in greater detail below.

Pulverization of Si: Large stress generated from the huge volume change during lithiation/delithiation could cause pulverization, which results in loss of electrical contact and eventual capacity fade. This fade mechanism is mainly observed in early studies of bulk Si or Si films [36][37].

Delamination and morphology change of electrodes: As shown in Figure 1.9, a loss of contact can happen between the active materials and current collector upon cycling, which means the entire electrode integrity can suffer from volume changes during cycling.

Unstable solid electrolyte interphase: Besides the mechanical failure of cells, the irreversible consumption of Li ions is a major cause of fade. During cell operation, an SEI layer is formed on the electrode surfaces. This passivating SEI layer mainly consists of Li_2CO_3, various lithium alkyl carbonates ($ROCO_2Li$), LiF, Li_2O, and nonconductive polymers [30][38]. The SEI conducts ions and insulates electrons, therefore protecting active materials from further side chemical reactions [30]. However, for a Si-based anode, its large volume changes may affect the stability of the SEI. The SEI is likely to be disturbed by the volume changes of the active material, and fresh alloy surfaces will be exposed to the electrolyte during cycling. This may lead to continuous consumption of the electrolyte and the formation of a thick heterogeneous SEI layer with high

resistance. The properties of the SEI layer directly determines an electrode's coulombic efficiency and electrochemical impedance. A stable and dense layer is a vital factor for better cycle life of silicon anodes.

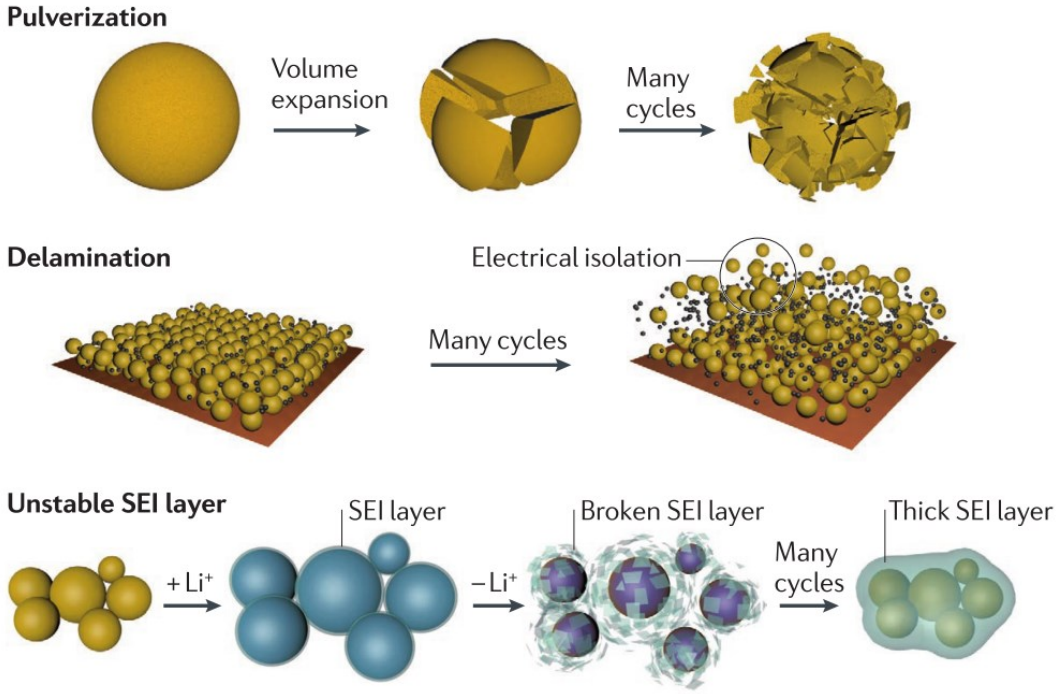

Figure 1.9 Cell failure mechanism of silicon. Reproduced with permission from Reference [35], Copyright 2016 Springer Nature.

1.4.1.3 Two-Phase Regions

A two-phase region might be observed in some cases during alloy lithiation/delithiation. This will cause a voltage plateau. Phase boundaries encountered during two-phase regions can result in additional particle damage due to inhomogeneous volume changes, while lithiation in a single-phase region results in more homogeneous volume change [11][29][32][39] [40]. In the case of Si, the formation of crystalline $Li_{15}Si_4$ is indicative of a two-phase region. Since fade and two-phase regions are often coincident, it is thought that two-phase regions should be avoided during cycling [11].

1.4.2 Si-containing Alloys

As mentioned in 1.3, forming an active-inactive alloy is one of the common methods to deal with volume expansion. Si-based alloys are designed to be made of active Si surrounded by inactive phases. Active/inactive composites are normally made to be nanostructured or amorphous because nanostructured and amorphous particles expand homogeneously, but crystalline materials experience structural transitions to phases with different lattice constants, leading to inhomogeneous expansion [41]. Nano-particle sizes can also reduce fracturing and improve cycling by decreasing the mechanical stress generated during cycling [15][42].

Nanostructured Si-M alloys, such as Si-V [43], Si-Cr, Si-Mn [44], Si-Fe [45], Si-Co [46], Si-Ni [47], Si-Ti [48] have been extensively studied. According to the studies on Ni-Si thin films by Du *et al*., Ni was found to suppress the lithiation voltage, resulting in a reduction in capacity. They attribute this voltage suppression to internal stress in the thin film during lithiation from the presence of Ni [49]. In the study of the Si-Ti system, inactive $TiSi_2$ phase was found effectively suppress the formation of $Li_{15}Si_4$ during cycling with no noticeable change in the average voltage (in contrast to Si-Ni alloys), resulting in relatively low polarization cycling. They claimed that the $Li_{15}Si_4$ phase suppression was coincident with good cycling performance and good electrode structure maintenance upon lithiation/delithiation [48].

Besides refining the electrode material, the optimization of binders is also of great importance. In addition, advanced electrolyte additives can further enhance the overall performance. Together with pre-lithiation methods (to reduce irreversible capacity during the first cycle), optimization of all these methods is required for enabling Si-containing alloy anodes for Lithium-ion batteries.

1.5 Mechanical Alloying

Nanostructured Si-M (M = transition metal) ball milled alloys are studied extensively for use as negative electrode materials in Li-ion batteries [46–48,50–56]. This application requires such alloys to have a nano-grained structure in order to achieve long charge/discharge cycle life. However, the ball milling reaction itself has received little attention. This is important since alloys that can be processed easily would be much more attractive from a commercial point of view.

Despite the widespread use of MA methods, the involved chemical and physical processes are not yet clearly understood, and many questions remain unresolved. Milling parameters such as rotation speed, ball-powder ratio, charge ratio and the milling ball composition and radius may affect the rate of amorphization and compositions in the final milled product [57]. Experimental optimization is still the main approach to find ideal conditions for the MA of a new alloy composition. Towards a full understanding of MA process, the following considerations need to be taken, such as (a) the ball kinetics during milling (quantification of the interactions between the milling balls and the powder during MA); (2) deformation phenomena (fracture, welding) when powder particles interact with the milling balls; (3) physical phenomena (diffusion, heating, work hardening, recovery, etc.) that occurs within the powder particles [58]. A number of these aspects have been studied previously for different systems (see References [58–63]). For a given set milling parameters, a quantitative description of the ball milling process is of great interest as it could provide a way optimize and predict the outcome of possible MA processes.

Miani et al. have studied the kinetics behavior of $Fe_{75}C_{25}$ during ball milling with the aid of XRD and ^{57}Fe Mössbauer spectroscopy. The crystal size, l, of iron obtained from X-ray diffraction was found to fit a sigmoid type function

$$l\ (nm) = 38\ [\ 1 - e^{(-\frac{1.14}{t^2})}] \qquad (1)$$

where t is the milling time in hours. They also found that the iron conversion rate follows a sigmoid-type curve as well, which could be expressed as:

$$X_{Fe} = K\ e^{(-bt^n)} \qquad (2)$$

where X_{Fe} is the mole fraction of metallic Fe phase in the sample, k, b, and n are empirical constants. The constant n is related to impact energy and b is referred to as the "working condition". K is used to set the scale. This equation could describe the amount of metallic Fe phase in the milled powders very well [64]. Vasconcelos and Figueiredo applied a modified version of this model to the Fe-Cu and Fe-N systems:

$$V(t) = K\ e^{(-bt^n)} + R \qquad (3)$$

Here $V(t)$ is the transformed phase volume, R is used to represent the volume of unreacted reactant, while k, b, and n are defined as previously. This modified equation works well to explain milling behavior in both the Fe-Cu and Fe-N alloy systems. Four stages occurring during the milling process of the Fe-Cu system were observed: (1) energy storage, (2) initiation of reaction and reaction rate increase, (3) decrease of the reaction rate, and (4) steady state [65]. These four stages could be well identified by the model proposed in Reference [65].

CHAPTER 2 EXPERIMENTAL METHODS

2.1 Sample Preparation

2.1.1 Ball Milled Alloy Preparation

Silicon (325 mesh, 99%, Aldrich) and tungsten (12 μm, 99.9%, Aldrich) powders in several stoichiometric ratios ($Si_{100-x}W_x$, x = 15, 20, 25, 30) were ball milled under Ar gas in a SPEX 8000-D mill (SPEX Certiprep, Metuchen, N.J.) using the optimized conditions for high energy ball milling described in Reference [57]: 180g of 1.6mm 440C stainless steel balls, 65mL hardened steel container, 0.5 mL total volume of sample powders. Milling time was varied from 1 hour to 16 hours in order to observe the kinetics of the Si-W alloying process. Ethanol (99.89%, containing 0.10% H_2O, Commercial Alcohols) was used for sample recovery. Sample vials were half filled with ethanol and milled for five more minutes. The resulting ethanol slurry was then collected in a pan and then dried in a solvent oven at 120°C in air. Some samples were subsequently heated in a tube furnace at 600°C and 800°C for 3 hours under an argon flow.

2.2 Characterization Techniques

2.2.1 X-Ray Diffraction

2.2.1.1. Theory

X-ray diffraction (XRD) is one of the most useful methods to study materials' crystal structure. X-radiation has a wavelength between 0.01 and 10 nm and was first discovered by Wilhelm Röntgen in 1895 [66]. X-rays can provide structural and compositional information after interacting with materials. X-rays can be generated in a vacuum tube by the interaction of high energy electrons with a heavy metal target. Copper K_α radiation is a common type of X-radiation used for XRD. A

high voltage (~45 kV) is applied in a copper X-ray tube which consists of tungsten filament cathode and a copper anode under vacuum. Electrons from the cathode are accelerated towards the anode and strike atoms in the copper anode. The core shell electrons of copper can be knocked out, and the resulting vacancies are then filled with electrons from higher energy levels. As a result, photon emission occurs in characteristic X-radiation wavelengths. The energy of the characteristic X-radiation equals to the difference between the initial and final energy states of the electron.

Due to the spin-orbit interaction, two energy levels exist within the Cu 2p orbital: the $2p_{1/2}$ and $2p_{3/2}$ orbitals. As a result, K_α radiation consists of $K_{\alpha1}$ and $K_{\alpha2}$ radiations. The $K_{\alpha1}$ transition is generated from the doubly degenerate L_3 ($2p_{3/2}$) to the K (1s) orbital, the energy difference between these two states is 8.048 keV [67], which corresponds to a photon with a wavelength of 1.542 Å. The $K_{\alpha2}$ transition is from the L_2 ($2p_{1/2}$) to the K (1s) energy level, with an energy of 8.028 keV, resulting in the emission of a photon with a wavelength of 1.546 Å. Radiation with lower intensity such as K_β radiation can be filtered out with a monochromator. It is difficult to separate $K_{\alpha1}$ and $K_{\alpha2}$ with a monochromator because their wavelengths are too similar. However, for crystalline samples, $K_{\alpha2}$ radiation may be subtracted numerically after the XRD pattern is collected. Nanocrystalline or amorphous samples have broad peaks, and the presence of $K_{\alpha2}$ radiation has little effect on their XRD pattern.

Figure 2.1 shows a schematic of a Bragg-Brentano diffractometer. Once X-rays leave the X-ray tube, they pass a divergence slit, which defines the size of the X-ray beam. The X-rays then interact with the powder sample and get scattered from the electrons in the sample [68]. When the scattered X-rays are in phase, constructive interference occurs. The angles at which constructive interference may occur are given by：

$$2d \sin\theta = n\lambda \qquad (2.1)$$

This equation is known as Bragg's law, where n is an integer, λ is the wavelength of the incident radiation (1.54 Å for CuKα), and θ is the angle of the incident radiation to the sample. This relationship can be derived from trigonometry, as shown in Figure 2.2. Beam 1 and 2 are two parallel incident beams, and beam 1' and 2' are the corresponding diffracted beams. When the difference in the distance travelled by beam 1 and beam 2 (AD + BD in Figure 2.2) is equal to an integer multiple of its wavelength, the photons will be in phase, and the amplitudes of their waves will add (constructive interference), resulting in radiation with increased intensity. In a Bragg-Brentano diffractometer, such as the one used in this study, the diffracted beam then passes through anti-scatter slits followed by a receiving slit and then a diffracted beam monochromator to filter out any radiation other than Cu-K_α radiation (e.g., Cu-K_β radiation and radiation from sample fluorescence). Finally, the filtered radiation is converted to an electronic signal by a detector. XRD patterns are often plotted as the intensity of the scattered radiation vs. the scattering angle, 2θ. At values of 2θ which give constructive interference, peaks in the scattered X-ray intensity will be observed.

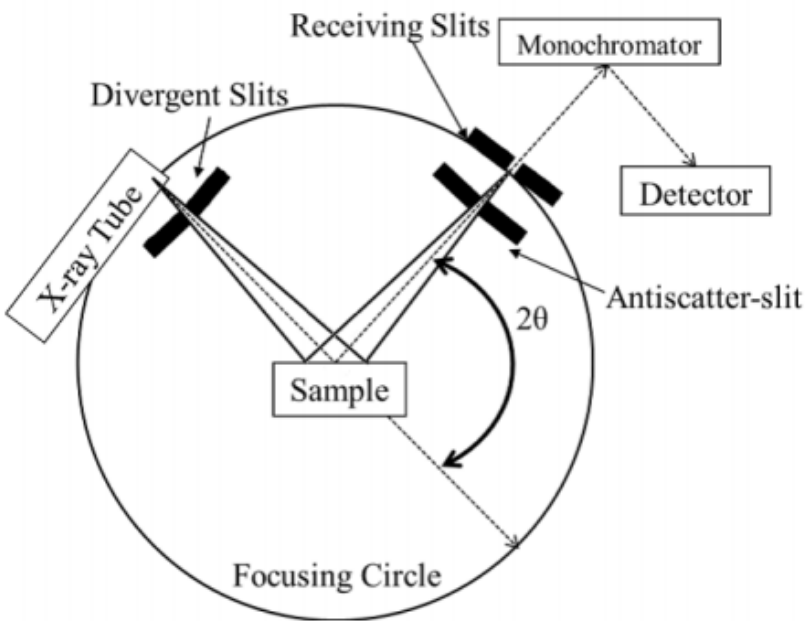

Figure 2.1 Schematic diagram of the Bragg-Brentano diffractometer, shown with divergent slits, antiscatter slits and receiving slits. Reproduced with permission from Reference [68], Copyright 2015 Camardese, J.

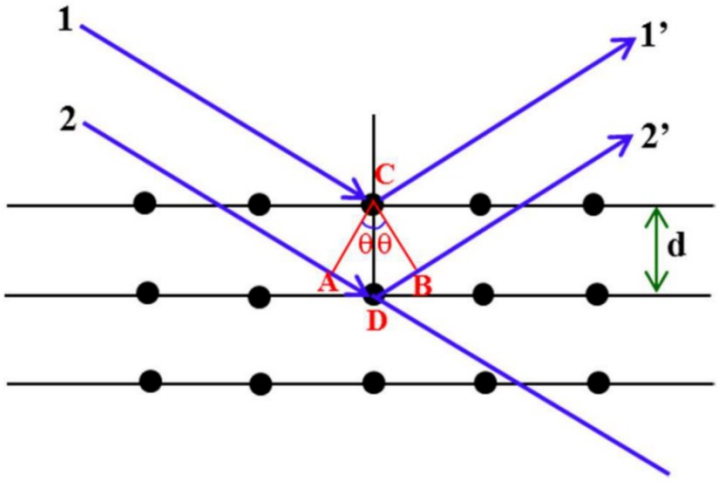

Figure 2.2 Schematic diagram of Bragg diffraction from crystalline planes in a solid. Reproduced with permission from Reference [69], Copyright 2016 Li, J.

2.2.1.2 XRD Measurements

XRD patterns were collected with a Rigaku Ultima IV diffractometer equipped with a CuKα radiation, a dual position diffracted graphite monochromator and a scintillation counter detector. A filament current of 40 mA and an accelerating voltage of 45 kV were used to generate X-rays. Powder samples were loaded into a stainless-steel sample well with dimensions of 25 mm × 20 mm × 3 mm on a stainless-steel plate and pressed flat with a glass slide to ensure a flat upper surface that was coplanar with the top of the sample holder before measurement. Measurements were taken in 0.05° steps with a count time of 3 seconds per step, in the range of 20° to 60° 2θ. The collected XRD patterns were compared with the ICDD PDF2 database for phase identification [70].

2.2.1.3 Quantitative Phase Analysis in XRD

The main principle of quantitative X-ray diffraction analysis is that the intensities of diffraction peaks from a phase of interest are proportional to the fraction of this phase in a mixture. However, many sample-related and instrumental-related factors make it difficult to directly compare peak intensities from a phase in a mixture with peaks from the pure phase prepared and run under similar conditions.

The reference intensity ratio (RIR) method [71] has been one of the most popular methods for general quantitative phase analysis. The traditional RIR method compares the intensity of one or more diffraction peaks from a phase with the peak intensity of a standard in a 50:50 mixture by weight [72]. If the measured RIR values are known for all phases in a sample, the weight fraction can be determined for each phase in the mixture. Using an internal standard could help eliminate

absorption and matrix effects [73]. The RIR method is straightforward and easy to conduct. RIR values using corundum as an internal standard are compiled in databases. For example, the ICDD power diffraction file includes I/I_c values (intensity of the phase peak divided by the peak of corundum), which enables quick semi-quantitative analysis of XRD patterns [70]. However, entries in such databases commonly only use the most intense peak, and the selected pure phases normally have well-defined crystal structures. Therefore, the use of RIR database is limited and often the phases used do not resemble the actual phases in MA samples. A series of more accurate measurements of RIR values is required for such samples.

The Rietveld method [74] is another good approach for quantitative XRD analysis [75,76]. Rietveld quantitative analysis involves calculating diffraction patterns of every component of a mixture using a crystal structure model. The calculated pattern is then fitted to an experimental pattern by varying parameters of the model, such as lattice constants, atom positions, atom occupancies, preferred crystal orientation, grain size, and phase fractions. The Rietveld method is very powerful. Besides phase quantification, some important information, such as unit-cell parameters, atomic occupancies, and information on crystallite size/strain can be obtained [73]. However, Rietveld refinement requires the crystal structure of all component phases to be known and be in a crystalline state, which excludes the ball milled samples in this study [73]. Ball milled materials might be amorphous, disordered or nanostructured. Amorphous materials lack long-range order, leading to incoherent scattering and broad diffuse peaks corresponding to average atomic arrangements. Disordered or nanostructured materials contain ordered regions which are on the order of 10-1000 times the wavelength of X-rays. This leads to decreased scattering intensity and peak broadening, resulting in difficult/inaccurate refinements.

Another alternate method based on fitting full XRD patterns has been proposed to realize quantitative analysis [77–81]. The full-pattern fitting method applies a similar principle as the RIR method, but instead of using a single diffraction peak, full diffraction patterns are used. It is noted that quantities of amorphous or partially ordered materials can be directly determined if the amorphous/disordered phases are considered as distinct phases in the peak fitting procedure. This full pattern method compensates for preferred orientation and chemical variability (averaging reflections that are too strong with reflections that are too weak). The method can be applied to any materials system and requires little crystallographic information, only that suitable standards exist [73].

2.2.1.4 XRD Quantification Method Used in The Current Study

The methodology used in this study takes advantage of the RIR method, full-pattern fitting and the idea of Rietveld refinement to identify phases in MA Si-W alloys quantitatively. Like Rietveld refinement, full-pattern XRD patterns are fitted using least-squares minimization. XRD patterns were fit from 20° to 60° using Pseudo-Voigt peak shape functions. Figure 2.3 shows an example of a fitted XRD pattern. The fitted Si, W, Si_2W, and background fitting components are shown. In the fits, the integrated peak area ratios of each phase were fixed to those found in the ICSD database. Lattice constants of each phase were allowed to vary, which determined peak positions. The resulting fits were used to identify the amount of each phase present quantitatively. Quantitative XRD analysis was based on the principle that the intensities of a phase in a given XRD pattern are proportional to the fraction of that phase in a mixture. To determine the proportionality constant, TiN was used as a standard to determine the relative intensity of each

phase. TiN was selected for this purpose because of its stability and because it has a simple crystalline diffraction pattern in the studied scattering angle range.

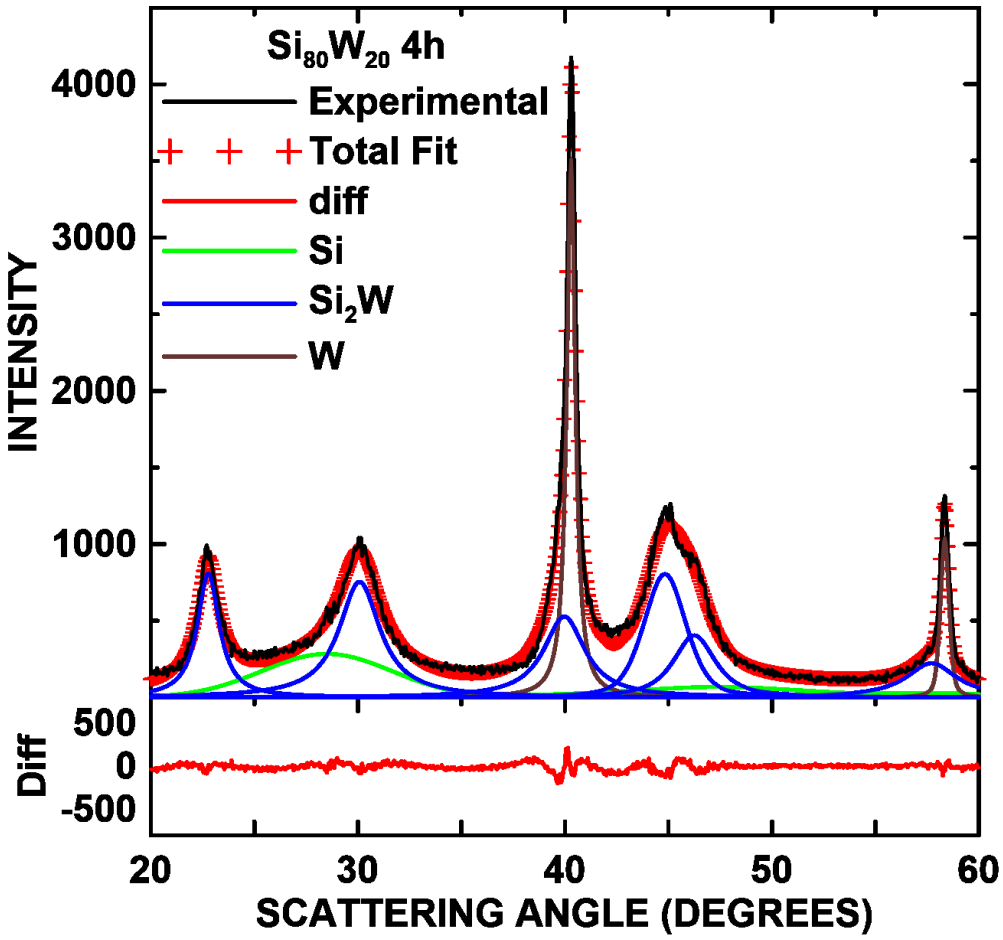

Figure 2.3 XRD pattern of the 4 h milled $Si_{80}W_{20}$ sample and the fitted pattern with contributions from amorphous Si, Si_2W, and W phases indicated. The difference between the experimental and fitted patterns is also shown.

Figure 2.4 shows a flowchart of the steps used to perform phase quantification from the XRD patterns, based on the methods described in Reference [71]. First, the reference intensity ratio (RIR), K_α, of each phase, α, was determined with respect to TiN from mixtures of TiN with known amounts of pure Si, W, and Si_2W. At least four different sample/TiN mixture ratios were used to

determine each value of K_α. All the powder mixtures were mixed for 30 minutes in a Retsch PM200 planetary mill at 100 rpm with one 13 mm tungsten carbide ball. The total integrated intensities (I_α) of each phase in the Si-W alloy XRD patterns were then determined using the fitting technique shown in Figure 2.3. These total integrated intensities were then converted to quantitative atomic ratios of each phase by using the pre-determined K_α values.

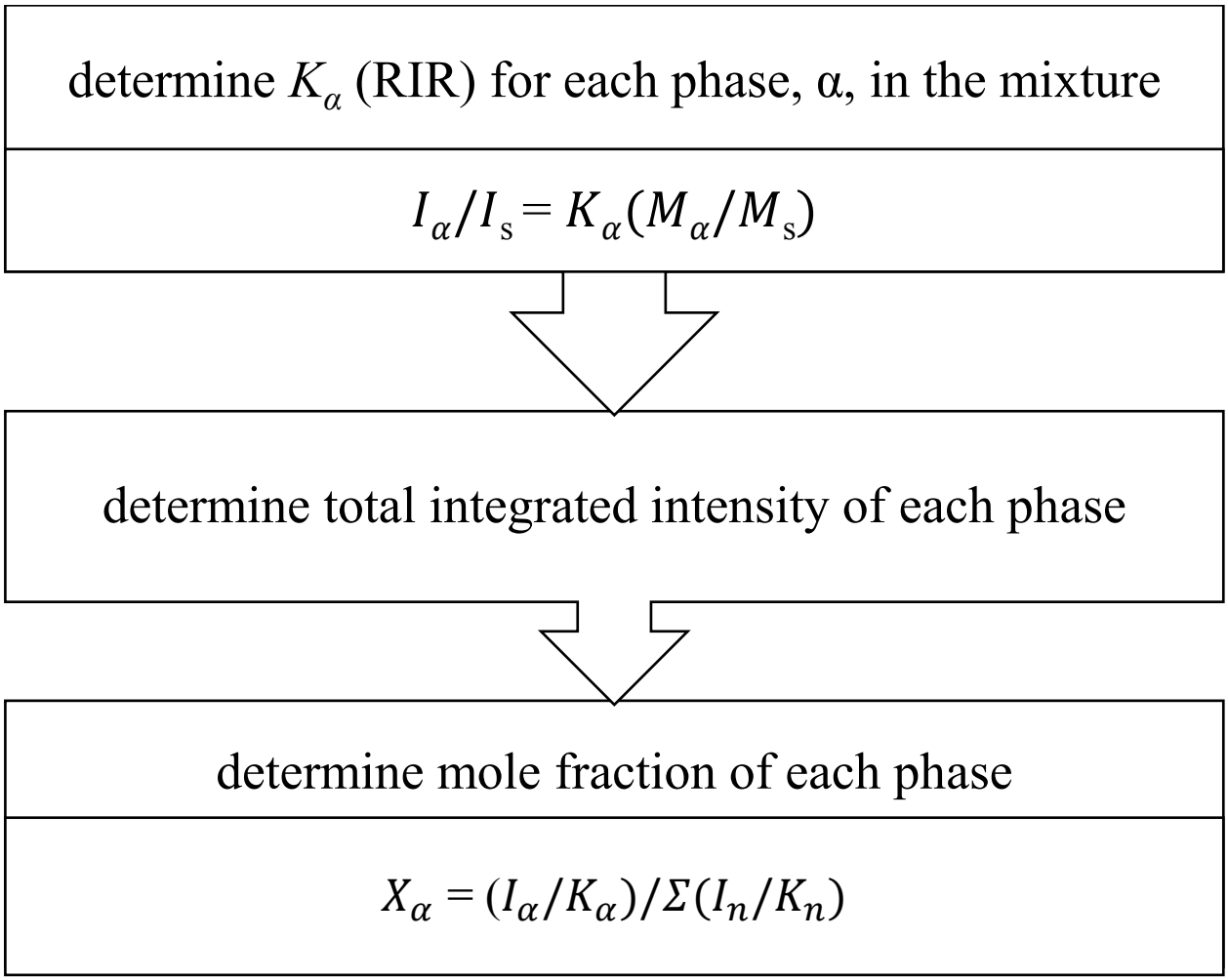

Figure 2.4 Flow chart of the quantitative XRD pattern analysis procedure.

2.2.2 Scanning Electron Microscopy and Energy Dispersive X-ray Spectroscopy

Scanning electron microscopy is a useful technique for investigating the surface morphology of materials. When a high energy electron beam interacts with the specimen in the scanning electron microscope (SEM), both elastic scattering and inelastic scattering can happen. Elastic scattering occurs when there is a change in the direction of the incident electron, but with negligible energy loss [82]. Backscattered electrons (BSE) are incident electrons elastically deflected back out of the specimen surface, BSEs can have an energy range from 50 eV to nearly the incident beam energy [82]. More electrons can be back scattered from an element with higher atomic number, which shown as a brighter color in images. Therefore, SEM images produced from BSEs can show atomic contrast, to obtain chemical composition information [82,83]

When inelastic scattering occurs, energy can be transferred from the primary beam electron to the atom, resulting in an ejection of an electron. This generates secondary electrons (SE) with energies that are normally less than 50 eV [82,83]. Secondary electrons are used principally for topographic contrast in SEM images, such as surface texture and roughness [82,83]. SEs are mostly generated from regions near the surface of a specimen and BSEs are generated from regions that are generally deeper [82]. Thus, SE images can provide better lateral resolution than BSE images [82].

During the interaction between the primary electron beam and the specimen, if a vacancy due to the ejection of a SE is filled by an outer shell electron, a characteristic X-ray will be generated [82,84]. Since each element has unique atomic structure, the X-rays generated are characteristic of

each element. This characteristic X-ray emission spectrum enables both quantitative and quantitative elemental analysis in energy dispersive spectroscopy (EDS) [82,84].

In this work, SEM images, as well as EDS spectra, were obtained using a TESCAN MIRA 3 field-emission electron microscope. This instrument is equipped with a backscattered electron detector.

2.2.3 Electrochemical Methods

2.2.3.1 Cell Construction

Powders of Si-W alloys were mixed with carbon black (Super C65, Imerys Graphite and Carbon) and a 10 wt.% aqueous solution of lithium polyacrylate (LiPAA) at a volumetric ratio of 70/5/25 in distilled water using a planetary ball mill (Retsch PM 200) with two 11 mm WC balls at 100 rpm for 1 hour. A thin layer of slurry was coated on Cu foil (Furukawa Electric, Japan) using a 0.1 mm coating bar. The coating was then dried in air at 120°C for 1 hour. Typical active loadings were 2.32 mg/cm^{2}or 2.38 mAh/cm^2 for a sample with 1025 mAh/g specific capacity. The Si-W electrodes were incorporated into 2325 type coin cells with Li metal as the counter/reference electrode and 1M $LiPF_6$ (BASF) in a solution of FEC: EC: DEC (1:3:6 by volume) electrolyte. The electrodes were separated by two layers of Celgard 2300 separators.

Figure 2.5 shows a general schematic of a 2325-type lithium coin cell made in this thesis. Cells were made in an argon atmosphere glovebox. First the electrodes and separator were wet with excess electrolyte in a stainless steel can. Spacers were added to apply an appropriate pressure on the electrodes, to maintain good electrical contact. The bottom and top casings were separated by a plastic gasket, to prevent electrical contact. Cells were crimped twice to ensure a good seal.

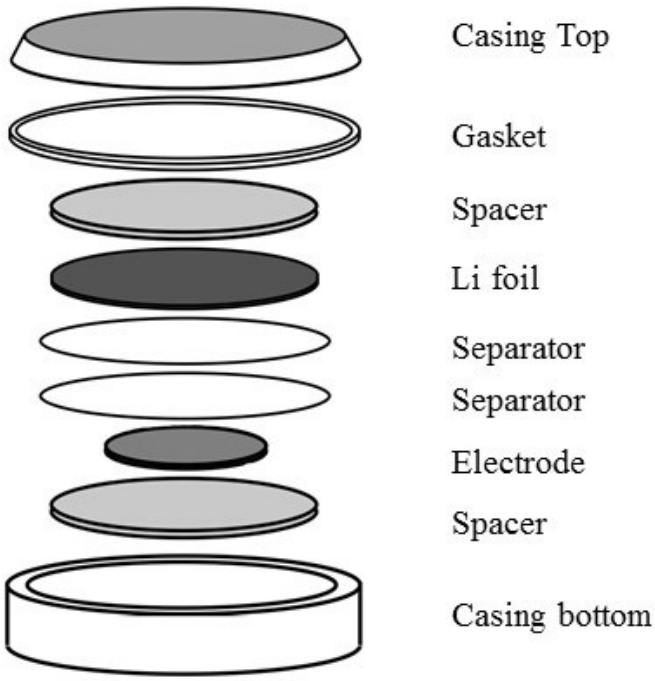

Figure 2.5 A Schematic diagram of 2325-type coin cell assembly.

Half-cells are easy to make and easy to understand as a first evaluation step. All materials as prepared in this thesis were tested in half-cells. Lithium foil was used as the counter electrode so that the amount of lithium is not limited. Assuming the counter electrode impedance is small, changes in the measured voltage in a half-cell may be attributed solely to changes from the working electrode, to a good approximation. This allows properties such as the capacity of a single electrode to be measured. Combined with excess electrolyte, the improved or worsened performance of tested half cells can be directed related to the alloy material.

2.2.3.2 Electrochemical Tests

Electrochemical techniques were used to test the performance of electrode materials. Electrochemical tests were performed using a Neware Test System. Coin cells were cycled at 30°C, between 5 mV and 0.9 V at a rate of C/20 and signature discharged (lower currents in steps with a relaxation time between each current change) to C/40 for the first cycle; and at a C/10 and signature discharged to C/20 for following cycles. Cells were charged and discharged with a constant current until the upper cut-off voltage (0.9 V) or the lower cut-off voltage limit was reached. 'C-rate' is used to describe the constant current that used in cycling conditions. It is defined as the theoretical capacity of a cell (in mAh) over the desired charge/discharge (in h). For instance, C/10 means with this charge/discharge current rate, it would take 10 h for a cell to be fully charged/discharged to reach its theoretical capacity. In this thesis, a signature discharge, which simulates the cycling conditions of commercial lithium-ion cells, were performed on all candidate anode materials to mimic the constant current, constant voltage charging protocol that is typically used in full cells [11].

Electrochemical measurements can provide important information, such as the working voltage window, capacity, energy density, rate capability and cycle life. Phase changes and diffusion behavior can also be interpreted from appropriate electrochemical measurements. Those properties are crucial parameters when evaluating the commercial potential of electrode materials.

Voltage curves are one of the most important electrochemical measurements. The measured voltage is plotted versus the gravimetric capacity. The voltage curve shows changes in the chemical potential as the discharge/charge proceeds. According to the Gibbs phase rule, the

degrees of freedom in a closed system at equilibrium is defined as f = C - P + N, where C is the number of independent components, P is the number of phases existing in the system, and N is the number of any additional system variables [85]. For the Li-Si binary system at constant temperature and pressure, plateaus occur in the voltage curves when there is a two-phase region. This is because C = 2, P = 2, and N = 0 corresponds to zero degrees of freedom. In such a region, the potential does not change with the Li concentration. In contrast, a sloping region in the voltage curve indicates the existence of a single-phase region. In this case, only one phase exists. Therefore the number of degrees of freedom is one and thus the potential can change with Li concentration [86].

Differential capacity curves (dQ/dV vs. V, where Q = capacity and V = cell potential) allow small changes in voltage curves to be observed more easily. For example, plateaus in a voltage profile (presence of two-phase regions) correspond to sharp peaks in a differential capacity curve, while sloping regions in a voltage curve (single phase region) result in broad peaks in the differential capacity. These characteristics are very useful. For example, the formation of two-phase regions during the cycling of alloys is undesirable, as two-phase regions cause inhomogeneous volume expansion and high internal stresses, which can result in rapid capacity fade. During the alloying process between Si and Li, a sharp peak at 0.43 V during delithiation will be observed if $Li_{15}Si_4$ is formed during cycling. However, the differential capacity plot of amorphous Si without formation of $Li_{15}Si_4$ during cycling shows two broad peaks during delithiation [87]. In this thesis, alloying Si with inactive W is expected to result in suppression of $Li_{15}Si_4$ formation. Thus dQ/dV plots are of great importance to verify this expectation.

Additionally, cycling performance plots, which show the capacity versus cycle number, are very useful as well. Information including charge/discharge capacity at each cycle, irreversible capacity, coulombic efficiency (CE), and cycling stability can be directly obtained.

This chapter has introduced experimental techniques that are utilized in this present study. The following chapters will discuss results that are obtained from those studies as well as some supplemental experiment details.

CHAPTER 3 BALL MILLED Si-W ALLOYS

3.1 Introduction

Nanostructured Si-M (M = transition metal) ball milled alloys have been studied extensively for use as negative electrode materials in Lithium ion batteries [46–48,50–56]. Alloys with a nano-grained structure are expected to achieve long charge/discharge cycle life. However, the ball milling reaction itself has received little attention. This is important since alloys that can be processed easily would be much more attractive from a commercial point of view. In this chapter, the microstructure of ball milled silicon-tungsten alloys ($Si_{100-x}W_x$, x = 15, 20, 25, 30) and the ball milling process are discussed in detail. The phase evolution was quantitatively followed during milling, allowing for a detailed understanding of the ball milling process. A volume element model of the process was proposed that suggests energy accumulates after every ball collision, eventually overcoming the activation energy for the reaction of Si and W to form Si_2W. The kinetics of these processes and the tendency for reactants to cake in the mill are important parameters to consider for the practical synthesis of different Si-metal alloy materials.

3.2 XRD Characterization

3.2.1 X-Ray Diffraction Patterns

3.2.1.1 XRD Patterns of Si-W Alloys as A Function of Milling Time

In this present study, X-ray diffraction was used as a major method to study the structure and phase constitution of each material. Figure 3.1 shows powder XRD patterns of ball milled $Si_{100-x}W_x$ (x = 15, 20, 25, 30) alloys at different milling times. XRD peaks of known phases are indicated. With increasing milling time, crystalline Si peaks disappear, and amorphous Si is formed. After 4 h

milling time, no crystalline Si peaks could be observed. Peaks from Si_2W are present after 1 h milling time. The intensity of Si_2W peaks increases as milling time increased, suggesting the reaction of Si with W to produce Si_2W as milling progresses. However, peaks from W are dominant features in all XRD patterns in Figure 3.1, and exists regardless of milling time, despite there being an excess of Si present in all samples. From these results, it can be concluded that these ball-milled $Si_{100-x}W_x$ alloys are composed of amorphous Si, nanocrystalline Si_2W and a residual crystalline W phase that remains unreacted regardless of milling time. Excepting the presence of residual W, these results agree with the phases expected from the equilibrium Si-W phase diagram.

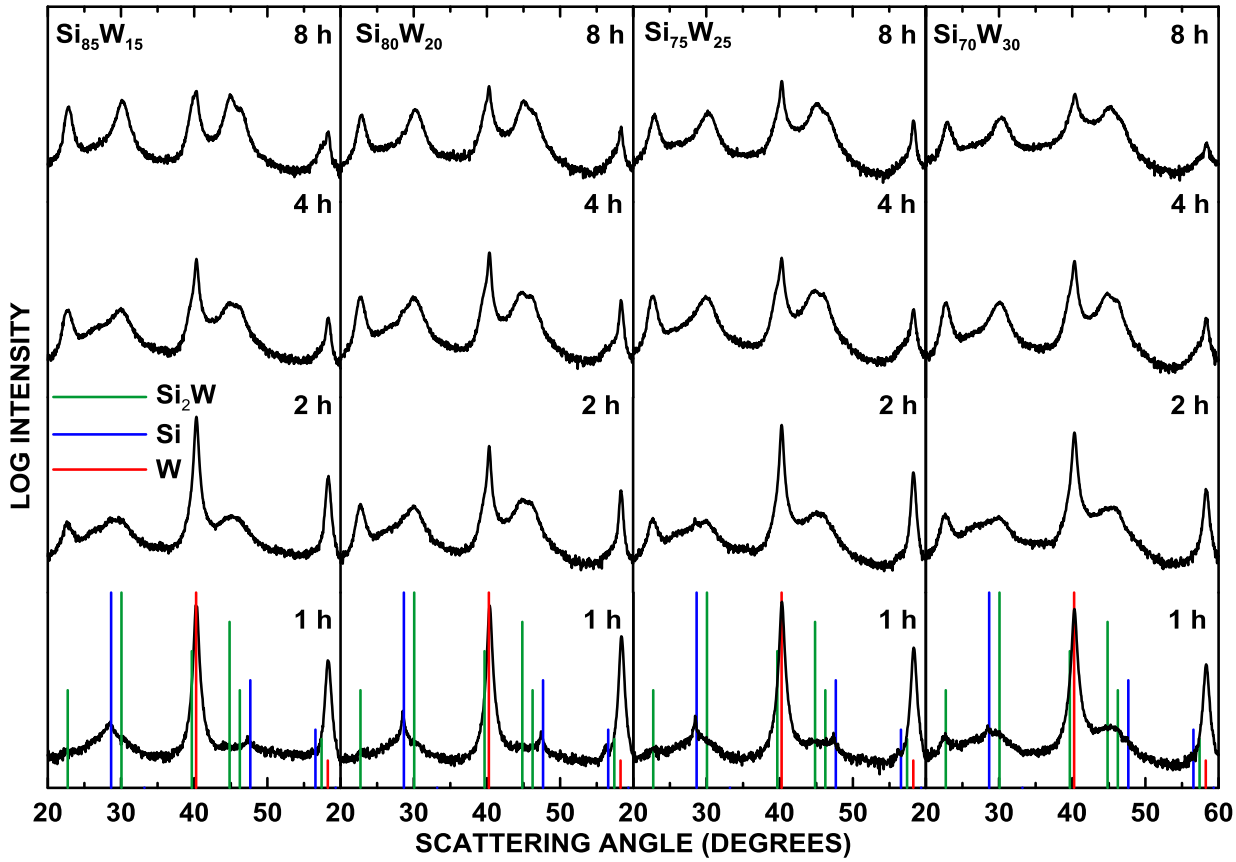

Figure 3.1 XRD patterns of ball milled $Si_{85}W_{15}$, $Si_{80}W_{20}$, $Si_{75}W_{25}$, and $Si_{70}W_{30}$ as a function of milling time.

3.2.1.2 Caking Investigation Using XRD

During the sample recovery process, a hard cake was sometimes found on the side of the milling vessel. X-ray diffraction was used to investigate changes in phase distribution caused by caking during SPEX milling by examining samples collected from different parts of milling vial. Figure 3.2 shows an example of this caking problem. Figure 3.2(a) shows the result of milling the $Si_{70}W_{30}$ sample for 16 hours. The amount of cake increased with milling time and could approximately account for up to 10% volume fraction of the originally loaded starting material.

Figure 3.2(b) shows XRD patterns of $Si_{70}W_{30}$ 16 h samples collected from different parts of the milling vial. The top panel in Figure 3.2(b) shows an XRD pattern of a sample collected by following the regular sample recovery procedure. This procedure recovers all of the sample, and therefore the XRD pattern is a mixture of samples collected from the cake on the vial wall and from the milling balls. The middle panel shows an XRD pattern of the cake only. Diffraction peaks from W are higher in sample powder collected from the cake, indicating that the cake is W-rich. The bottom panel shows an XRD pattern of the sample collected from powder loosely adhered to the milling balls. Only broad peaks from Si are visible. As expected, the XRD pattern of the complete sample shown in the top panel is consistent with being composed of a combination of sample from the balls and from the cake. The tendency for W to become sequestered in a cake in the side of the milling vessel accounts for its presence in all the samples, even after long milling time. This effect is much less pronounced when the W content was below 25 at.%. For these samples, caking was rare, and the residual tungsten content was very small (as shown in Figure 3.4).

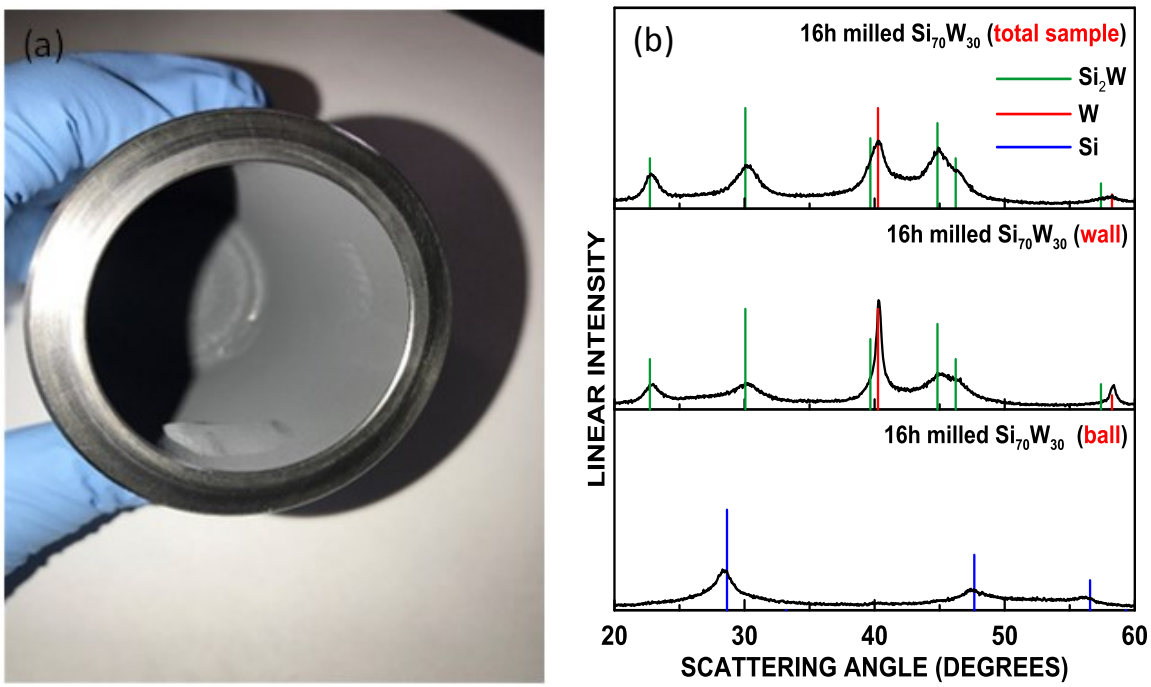

Figure 3.2 Example of caking in the $Si_{70}W_{30}$ sample. (a) Picture of cake on milling vial. (b) XRD patterns of powders collected from different parts of the milling vial.

3.2.2 Quantitative X-Ray Phase Analysis

As described in section 2.2.1.3, full XRD patterns were fitted to conduct quantitative analysis. XRD patterns were fit from 20° to 60° using Pseudo-Voigt peak shape functions. An example of a fitted XRD pattern is in Figure 2.3. In the fits, the integrated peak area ratios of each phase were fixed to those found in the ICSD database. Lattice constants of each phase were allowed to vary, which determined peak positions. The resulting fits were used to quantitatively identify the amount of each phase. Quantitative XRD analysis was based on the principle that the intensities of a phase in a given XRD pattern are proportional to the fraction of that phase in a mixture. Detailed steps to perform phase quantification from the XRD patterns are shown in Figure 2.4.

Figure 3.3 shows quantitative phase evolution in $Si_{100-x}W_x$ (x = 15, 20, 25, 30) compositions as a function of milling time as determined from quantitative XRD phase analysis. For $Si_{70}W_{30}$ and $Si_{75}W_{25}$ samples, Si and W are immediately consumed during milling and Si_2W is produced, while at higher Si contents, the reaction between Si and W only initiates after 1 h. All compositions reach steady state after about 8 hours. However, residual W remains in all samples, even after 16 hours milling. The amount of residual W was found to correlate with the tendency of the sample to form a hard cake on the side of the milling vessel, as shown in Figure 3.2 (a).

Peak broadening associated with small crystallite size is described by the Scherrer equation:

$$FWHM = \frac{K\,\lambda}{L\,cos\theta}$$

where FWHM is the full width at half maximum of the peak in radians, *K* is a constant (here taken as 0.9) and *L* is the average dimension of the crystallites perpendicular to the plane defined by the Miller indices of the peak in Å.

Grain sizes of each phase were calculated from the Scherrer equation are shown in Figure 3.4 for different compositions and milling times. As with previous studies [57], it was found that the peak width of amorphous of Si does not change with increased milling time. Instead, the crystalline Si peaks increased in width only slightly and decreased in intensity, while the amorphous Si peaks only increased in intensity as milling progressed. Therefore, the peak width of amorphous Si was fixed for all the fits, and its value was taken from the peak width of a 16 h-milled pure Si sample. The grain size of W follows a sigmoidal shaped curve during milling. As previously explained, the W phase detected after 8 h milling time presumably gets introduced from the hard cake on the SPEX vial wall. This may limit the reduction in grain size during milling. The grain size of Si_2W

at 1 h is small, presumably because at this initial stage of reaction between Si and W only a small amount of Si_2W is formed. The grain size of Si_2W then increases between 1 h to 4 h as its amount increases as the milling reaction progresses. After 8 h of milling, no significant changes in the grain size of Si_2W could be observed. This is consistent with the phase transformation results shown in Figure 3.4, where the reaction has reached a steady state after 8 hours.

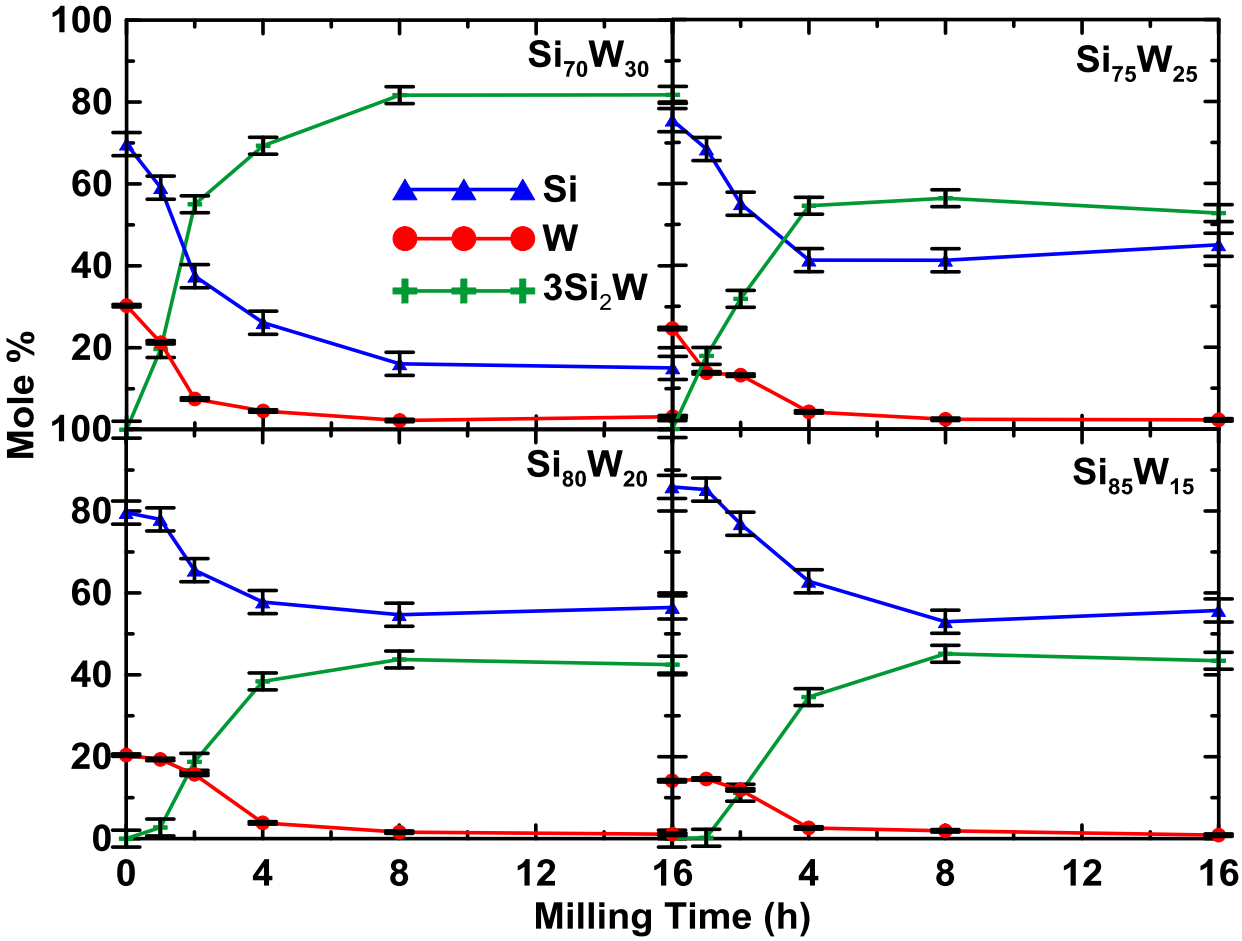

Figure 3.3 The amount of constituent alloy phases (error bars based on the standard deviation of 3 - 6 replicates of fitting) for different Si-W alloys as a function of milling time as determined by quantitative XRD phase analysis.

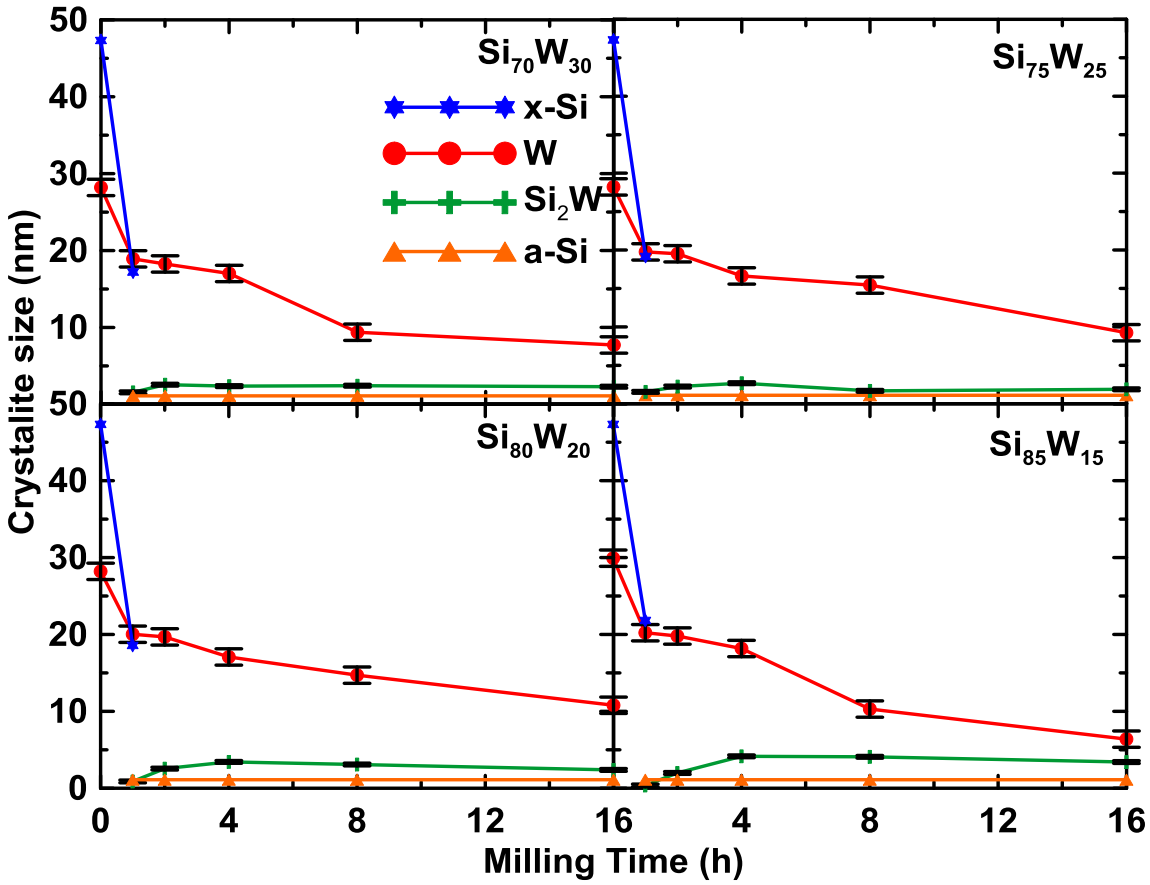

Figure 3.4 Average crystallite size calculated by Scherrer equation of the Si-W alloys as a function of milling time. Error bars based on the standard deviation of 3 - 6 replicates of fitting.

3.2.3 Model

Mechanical alloying is a discrete process where discrete energy transfers occur during each impact, which means only a small fraction of the powder is processed at each event [88]. In the ball milling process, ball-powder-ball collisions are the most frequent events. During such collisions, powder particles are trapped between colliding balls and undergo deformation and/or fracture processes [89]. After repeated deformation, pure elements can form nanocrystalline structures and energy can be stored in grain boundaries and defects [65] because atoms that reside in grain boundaries or other defects are in a higher energy state than atoms in the bulk of crystalline

grains. In this way, the severe deformation that occurs during milling increases the free energy of the pure metals. In addition, the interfacial energy arising from lattice defects and new grain boundaries also raises the free energy of solid solutions [90]. This gained energy could be the driving force for reactions that occur during mechanical alloying.

Here a model is proposed, based on the accumulation of energy during discrete impact events, to describe the ball milling process, which is shown schematically in Figure 3.5. An array of 10000 elements was used to represent the sample during milling. Each element represents a unit of volume that could be empty or filled with a single formula unit of Si, W or Si_2W. The volume units are initially filled with either Si or W, according to the initial stoichiometry used experimentally. A simulation is executed according to this model by first randomly selecting a number of volume elements (the impact zone). The impact zone is used to represent the small fraction powder volume trapped by the milling balls at each hit event. During the hit event the elements within the impact zone will gain some energy. After the hit event another set of volume elements is randomly chosen as the impact zone and the process is repeated.

A reaction will take place when the impact zone volume contains elements with correct stoichiometry and have enough accumulated energy to overcome a reaction energy barrier. As a result of this reaction, any Si and W available in stoichiometric amounts will be converted to Si_2W. This will cause some volume elements to be converted to Si_2W, and others to be converted to empty volume:

$$2\,\boxed{\text{Si}} + \boxed{\text{W}} \rightarrow \boxed{\text{Si}_2\text{W}} + \boxed{\phantom{\text{Si}}}$$

As the model proceeds random hit events continually cause the elemental Si and W to gain in energy and react until all the W has reacted with Si to form Si_2W.

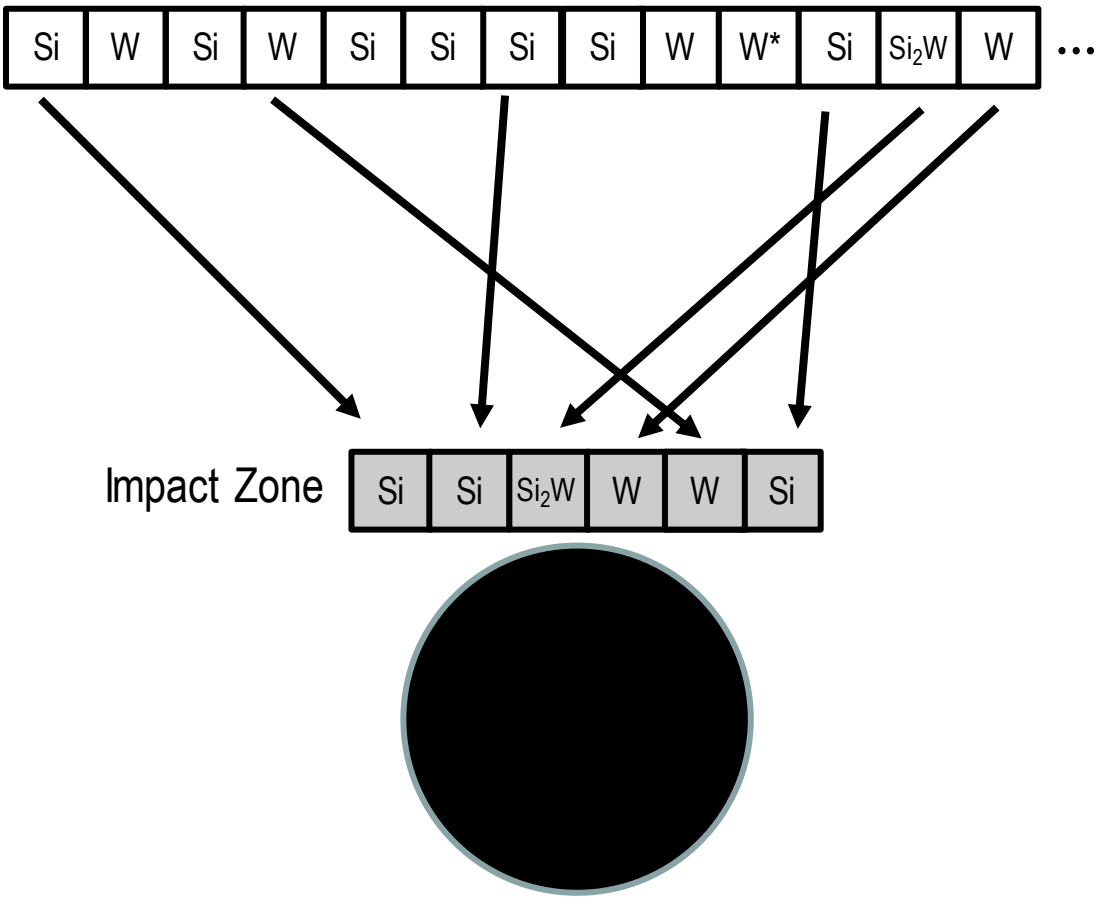

Figure 3.5 Scheme diagram of proposed model of mechanical alloying. W* represents volume elements containing tungsten that are unavailable for reaction due to caking.

In this model only three parameters are needed to describe the milling process: the size of the impact zone (N), the energy gained per hit: reaction energy barrier ratio ($\Delta E/E^*$), and the frequency of each hit event (ν). Another parameter, the fraction of W unavailable for the reaction (*f*), was added to account for caking. The fraction of unavailable W was determined from the amount of

unreacted W observed after 8 h milling. In this computer simulated milling process, the volume fraction of each phase (Si, W and Si_2W) was recorded after each hit event.

A computer program written in Java language was written to simulate the ball milling process using the proposed model. The program code is in Appendix I. Using $Si_{85}W_{15}$ as an example, Figure 3.6, Figure 3.7, and Figure 3.8 illustrate the influence of each parameter on the milling process. Figure 3.6 shows the volume fraction of Si resulting from simulations using the same impact zone size (N = 20), the same energy gained per hit: reaction energy barrier ratio ($\Delta E/E^* = 0.5$), but with different hit event frequencies ($\nu = 500\ h^{-1}$, $1000\ h^{-1}$, $3000\ h^{-1}$, $5000\ h^{-1}$ and $20000\ h^{-1}$). As the frequency increases, it takes a shorter time to reach a steady state for the reaction. When $\nu = 20000\ h^{-1}$, the volume fraction of Si quickly decreases within one hour and there is no significant change in the volume fraction after one hour of milling. However, when $\nu = 500\ h^{-1}$, the reaction of Si only initiates after four hours of ball mill and the volume faction of Si decreases more slowly than other curves simulated using higher frequencies. Therefore, the only effect of ν is to extend or shorten the amount of time required to complete the reaction, but besides this compression or expansion over time, the overall shape of the curve is not changed.

Figure 3.7 shows a series of simulated Si phase evolution curves using same impact zone (N = 20) and same frequency of each hit event ($\nu = 1000\ h^{-1}$) parameters, but with different energy gained per hit: reaction energy barrier ratios ($\Delta E/E^* = 0.10$, 0.15, 0.20, 0.50 and 1.00). It can be seen that a smaller value of $\Delta E/E^*$ can postpone the reaction of Si with W during milling. Such a postponed reaction was observed experimentally in for $Si_{85}W_{15}$ and $Si_{80}W_{20}$, where the reaction of Si and W only initiated after one hour of ball milling. According to this model, energy is accumulated during this initial milling time (e.g. in grain boundaries and defects) until a sufficient amount of accumulated energy is reached to exceed the reaction barrier. Therefore, an appropriate

value of ΔE/E* can be used to simulate the time required to accumulate energy during the initial stages of milling before the elements start to react. After the reaction commences, all the curves in Figure 3.7 have the same shape. Therefore ΔE/E* only affects the initial time to react, but does not affect subsequent reaction.

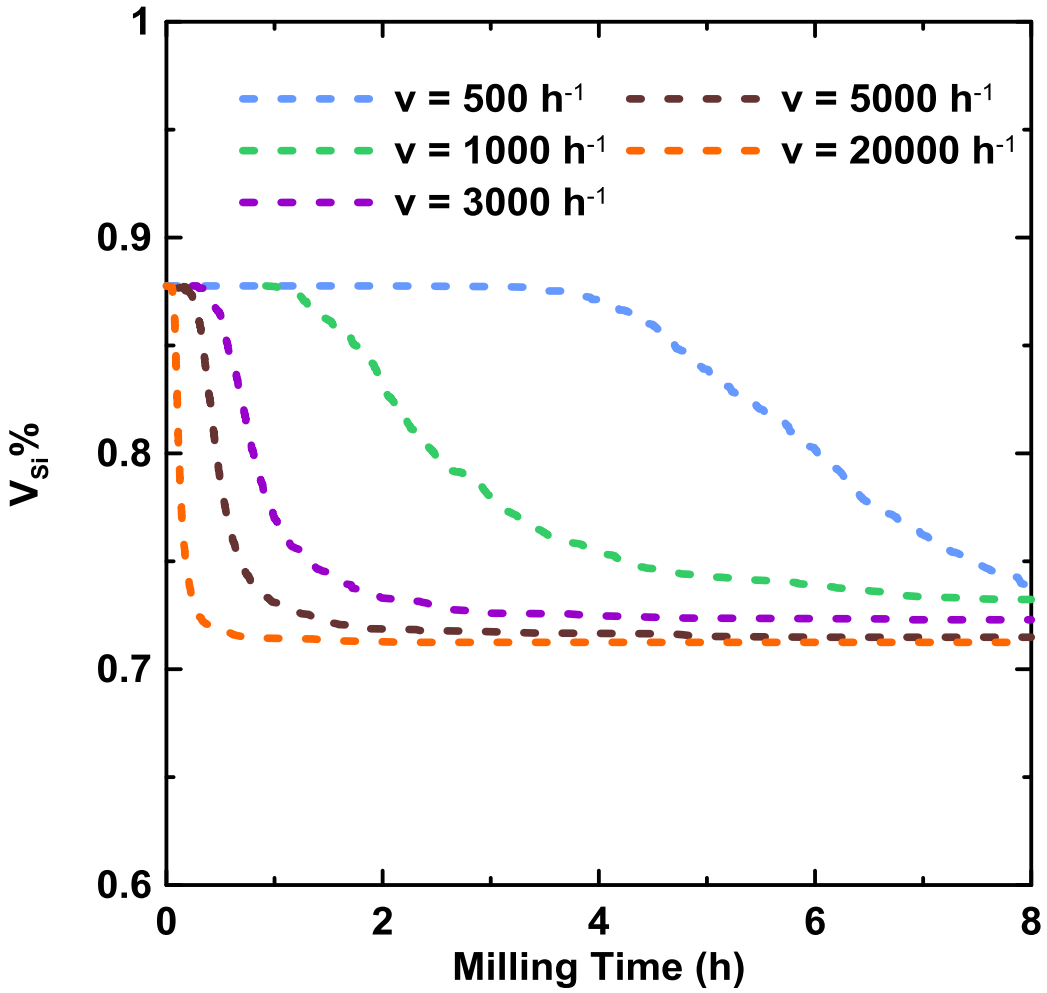

Figure 3.6 Simulated Si phase evolution curves using same impact zone size (N = 20), same energy gained per hit: reaction energy barrier ratio (ΔE/E* = 0.5), but with different hit event frequencies (ν = 500 h^{-1}, 1000 h^{-1}, 3000 h^{-1}, 5000 h^{-1} and 20000 h^{-1}).

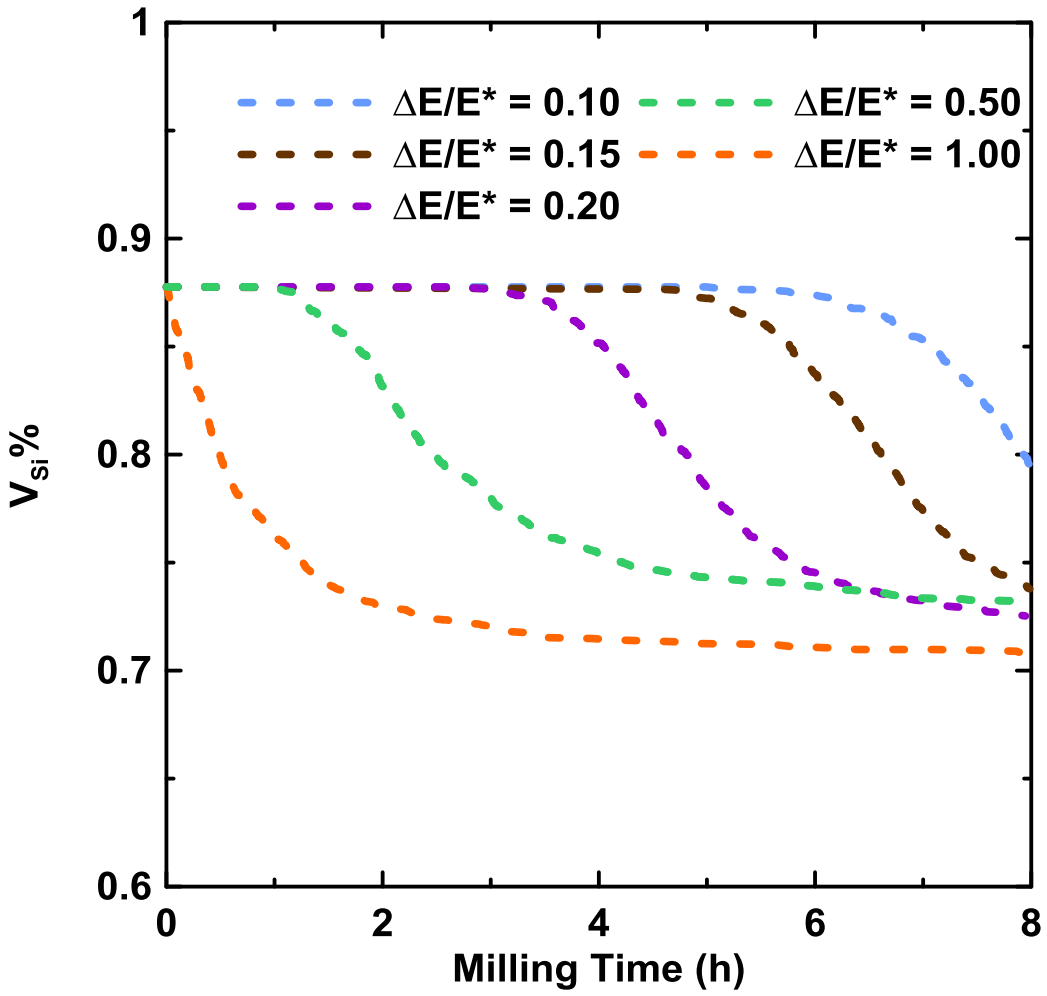

Figure 3.7 Simulated Si phase evolution curves using same impact zone (N = 20) and same frequency of each hit event ($\nu = 1000\ h^{-1}$), but with different energy gained per hit: reaction energy barrier ratios ($\Delta E/E^*$ = 0.10, 0.15, 0.20, 0.50 and 1.00).

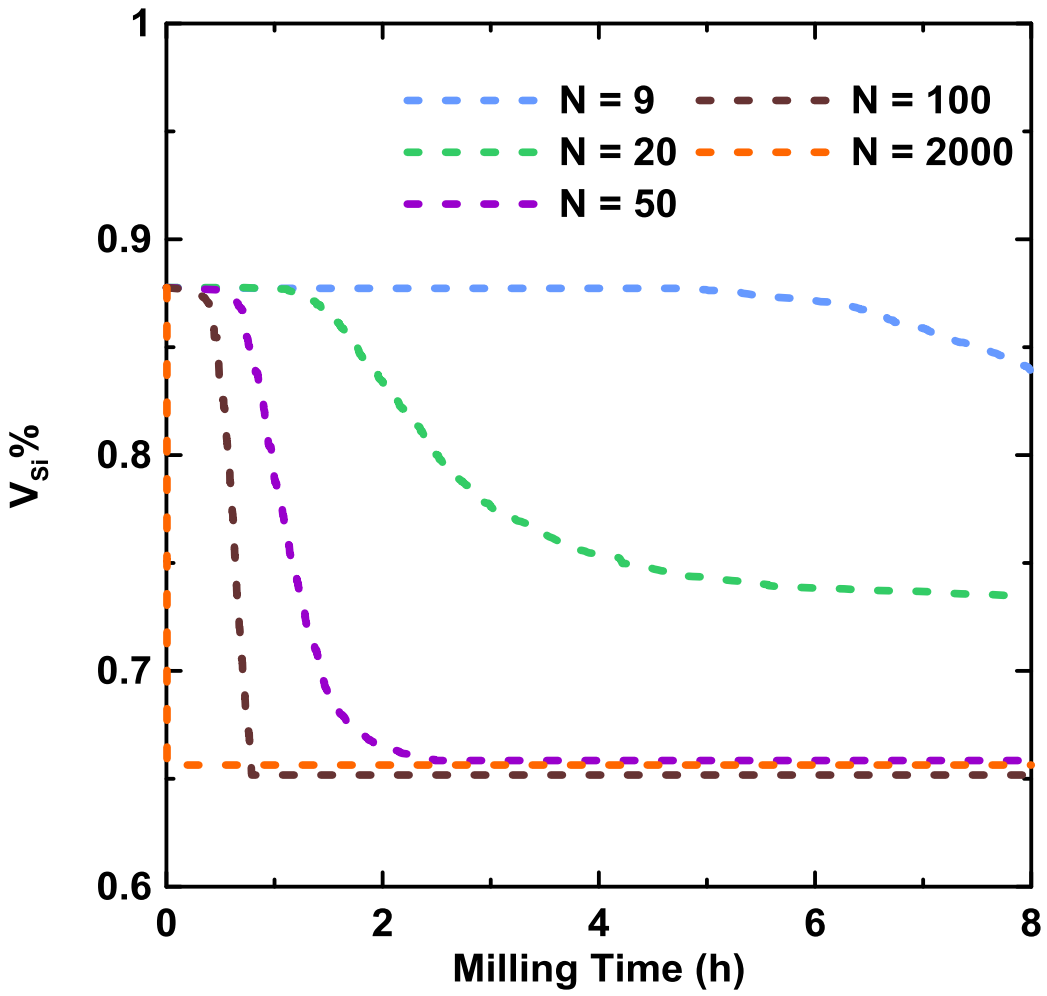

Figure 3.8 Simulated Si phase evolution curves using the same frequency of each hit event ($\nu = 1000\ h^{-1}$) and same energy gained per hit: reaction energy barrier ratio ($\Delta E/E^* = 0.5$), but with different impact zone sizes (N = 9, 20, 50, 100, and 2000).

Figure 3.8 shows a series of simulated Si phase evolution curves for $Si_{85}W_{15}$ alloy as a function of milling time. All Si phase evolution curves in Figure 3.8 were simulated using the same frequency of each hit event ($\nu = 1000\ h^{-1}$) and same energy gained per hit: reaction energy barrier ratio ($\Delta E/E^* = 0.5$) parameters, but with different impact zone sizes (N = 9, 20, 50, 100, and 2000). The size of the impact zone dictates how quickly the steady state composition is achieved. When the impact zone is large (comparable to the sample volume), the reaction will rapidly take place

and a steady is achieved within seconds. On the other hand, when the impact zone is much smaller than the sample volume (e.g. N = 9 in this case), it can take a very long time to reach a steady state. This is because little of the sample gains in energy per hit and, furthermore, when the impact zone is small the chances of the impact zone containing volume elements having the correct stoichiometry for reaction is also small. Thus, the impact zone changes the shape of the curve from a step (large impact zone) to sigmoidal (impact zone ~50 in this case) to a distorted sigmoidal curve in which steady state is reached only after a very long time for small impact zones.

3.2.4 Simulation Results

The volume fraction of Si after each hit was fit to the experimental phase compositions computed from XRD patterns as a function of milling time by the least squares fitting method. The fitting starts from an initial set of guesses for the N, $\Delta E/E^*$, and ν parameters. These parameters were then refined by using the Monte Carlo method. Given that Si-W alloys at different stochiometric ratios were prepared under the same SPEX milling conditions, N, $\Delta E/E^*$, and ν should be the same for all samples. Therefore, data for $Si_{100-x}W_x$ (x = 15, 20, 25) were fit simultaneously using the same N, $\Delta E/E^*$, and ν parameters, while f was allowed to vary between samples. The $Si_{100-x}W_x$ (x = 30) composition was fitted individually because the severe caking in this sample changed the milling conditions significantly compared to the other samples.

Figure 3.9 shows the simulation results and the fitting parameters are listed in Table 1. There is good general agreement between experimental data and simulated data, the general shape of the model fit all curves well. This allows for the interpretation of the milling process. Three reaction stages are observed for all samples and are roughly indicated for each composition in Figure 3.9. In Stage I (0-1 hours), the samples absorb collision energy and little reaction takes place.

According to the XRD results, during this stage, crystalline Si is converted to amorphous Si. In Stage II (1-2 or 3 hours) activated Si and W particles quickly react to form Si_2W. In Stage III (> 3 hours) steady state achieved. Similar observations of these mechanical alloying stages have been reported for Fe-Cu and Fe-N systems [88]. The effect of caking increases as the W content also increases, as expected, except for the $Si_{70}W_{30}$ sample.

For the $Si_{70}W_{30}$ sample, steady state is not achieved. Instead, Si continues to react with W for the entire 8 hour milling time. In addition, although the largest/thickest cake was formed by this sample, the caking fraction (Table 3.1) is reduced compared to other samples with lower W content. Considering the large amount of caking and continual presence of W, as shown by XRD and SEM, it seems that for this sample, the W that is caked on the wall is not entirely lost to the milling process as the model assumes. Instead, W seems to cake on the wall and then the cake becomes slowly eroded during the milling process, allowing the caked W to re-enter the active portion of the mill. This results in the amount of Si reacted after 8 h to be lower than the model predicts. It is suspected that when a large thickness of cake is formed on the wall, as observed for this sample, it then becomes vulnerable to fracture during milling and can therefore re-enter the mill volume as a reactant. When smaller thicknesses of cake form, as for the lower W content samples, the cake does not fracture and remains adhered to the wall, unavailable for reaction.

These results show that the possibility of caking should be taken into account in any milling model. Caking can alter the composition of alloys significantly from their initial constituents, even if the amount of caking is not visually obvious. Therefore, quantitative methods of analysis, such as quantitative XRD as done here, are necessary to determine product composition. Obviously, for practical production of alloys, it would be best to avoid caking all together. Application of the model to other Si-M systems may be useful for comparison of their characteristics during the

milling process, such as caking tendency, time for activation and the time needed to reach steady state. These are important parameters when determining which Si-M systems are useful for commercial production.

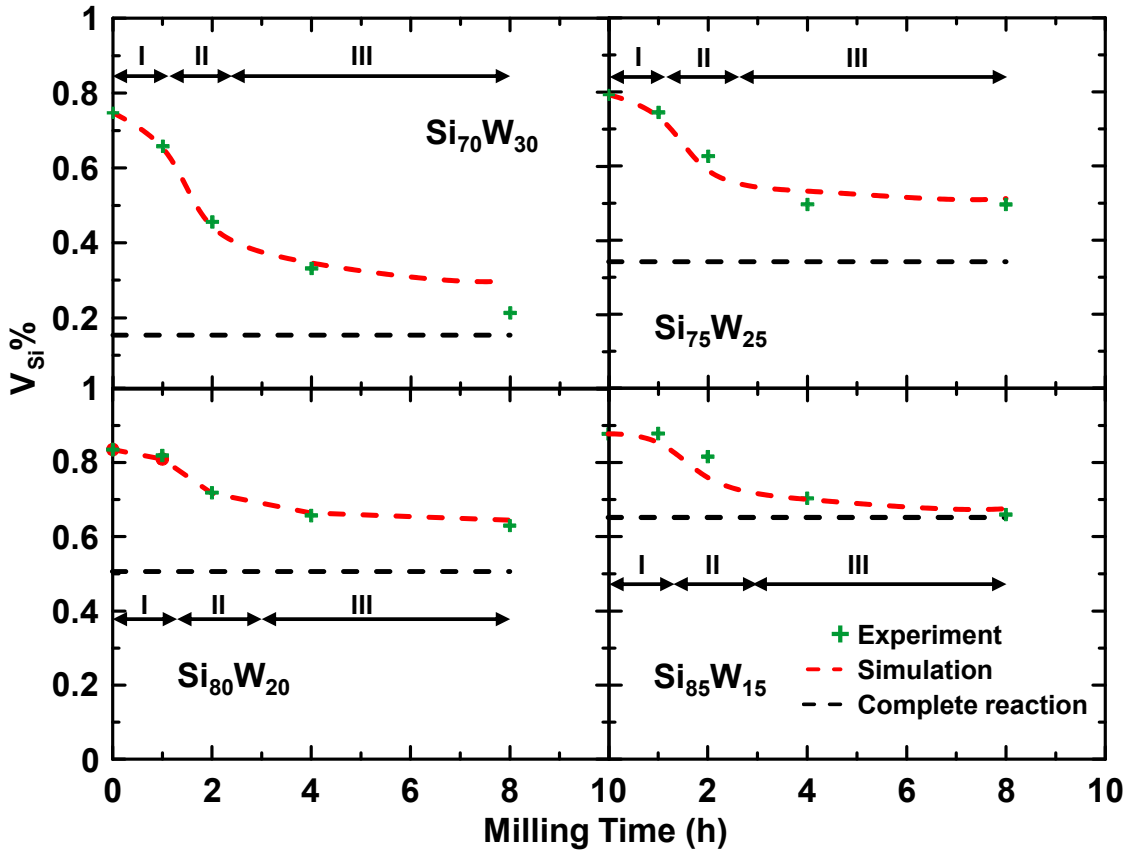

Figure 3.9 The volume percent Si phase as a function of milling time for different Si-W compositions as determined experimentally and calculated from the model described in the text. The black dashed line shows the composition corresponding to a complete reaction of all available (i.e., uncaked) W to form Si_2W. The three stages of the milling process discussed in the text are also indicated for each composition.

Table 3.1 Fitting parameters used in the simulation for $Si_{100-x}W_x$ alloys. ΔE/E* is the energy gained per hit: reaction energy barrier ratio, N is the size of the impact zone, ν is the frequency of each hit event, and *f* is the fraction of W unavailable for the reaction because of caking.

x in $Si_{100-x}W_x$	ΔE/E*	N	ν (hours^{-1})	$f \times 10000$
15	0.76	9	2751	40
20	0.76	9	2751	550
25	0.76	9	2751	613
30	0.86	11	2712	196

3.3 SEM Images

Figure 3.10 shows SEM images of $Si_{85}W_{15}$ at different milling times. Bright regions indicate the presence of W, while darker regions are Si-rich. As milling time increases, the particle size decreases as does the size of the different regions. However, W-rich regions are always present. This observation is consistent with XRD results which show the presence of pure W at all milling times.

The caking problem could also be observed from SEM images using a BSE detector. Figure 3.8 shows the SEM and its EDS mapping images of the 4 h milled $Si_{80}W_{20}$ composite. W is present in the bright regions of the BSE images. The large bright particle in Figure 3.11 (a) corresponds to unreacted W. These images confirm the presence of pure W in the sample, which presumably comes from the cake.

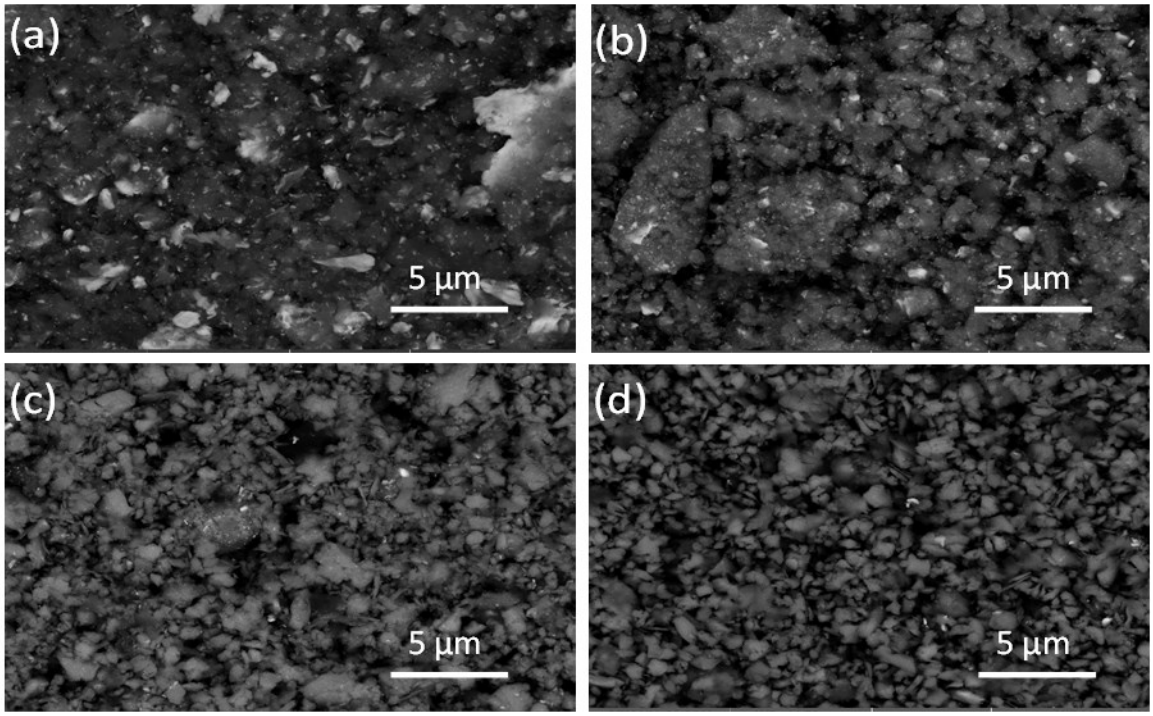

Figure 3.10 SEM images of $Si_{85}W_{15}$ at different milling times. (a) 1 h, (b) 2 h, (c) 4 h and (d) 8 h.

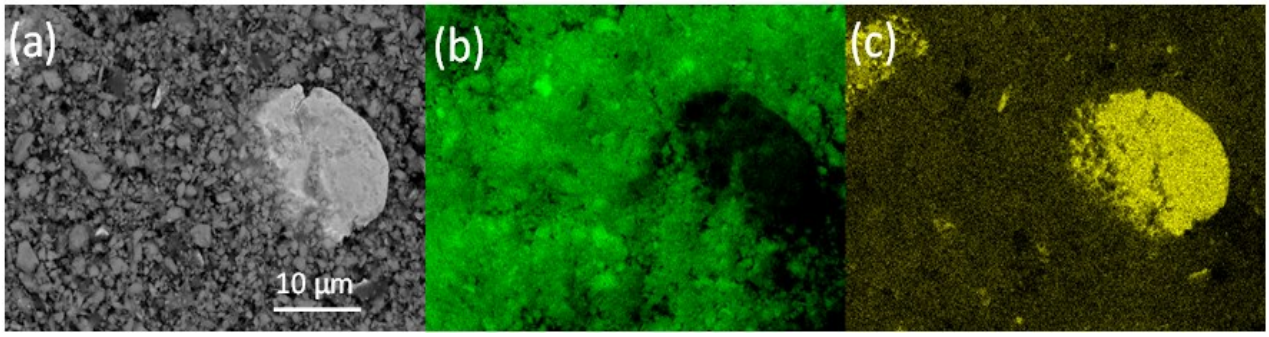

Figure 3.11 (a) SEM image of the 4 h milled $Si_{80}W_{20}$ sample and corresponding EDS compositional mapping images of (b) Si and (c) W.

3.4 Conclusion

The phase evolution, phase composition and grain size of ball milled Si-W alloys were quantitatively measured during the ball milling process. Ball milling was found to proceed in three stages with the amorphization of Si occurring after about 1 hour, followed by the reaction of Si with W to form Si_2W. After about 3 hours a steady state composition is reached. This milling process was successfully simulated by assuming constant volume element model and an activated process in which energy is accumulated after every collision. High W content Si-W alloys were found to form a W-rich cake at the side of the vial during the milling process, altering the final alloy composition. The milling kinetics of Si-W alloys should be compared in the future to other Si-M systems to assess manufacturability.

CHAPTER 4 Si-W ALLOY ANODE MATERIALS FOR LITHIUM ION BATTERIES

4.1 An Overview of the Electrochemical Performance of Si-W Alloys

It has been discussed in the introductory chapter that the massive volume changes that occur while cycling alloy materials may cause cell failure. Incorporating an inactive material and forming a nanocomposite particle is one method to increase the cycle life of alloy negative electrode materials. Here, $Si_{100-x}W_x$ alloys prepared by mechanical alloying are studied as anode materials for lithium-ion cells. Their electrochemical performance is discussed in this chapter.

Figure 4.1 shows the voltage curves of all $Si_{100-x}W_x$ alloy compositions prepared at different milling times. All compositions show the same general trend. It can also be seen in Figure 4.1 that the capacity becomes reduced as the W content is increased. The changes in the first reversible capacity of all compositions at all milling times are shown in Figure 4.2. Also shown are the capacities as predicted from the quantitative XRD analysis results of the previous chapter, assuming that Si is the only active phase in the alloys. The predicted capacity values are expected to be lower than the observed first lithiation capacities and greater than the observed first delithiation capacities. This is because the first lithiation normally includes electrolyte reduction processes, e.g., the formation of SEI layer, resulting in a higher capacity than the theoretical material's capacity. In contrast, a capacity lower than the actual alloy capacity is usually obtained during the first delithiation, which can be associated with the mechanical disconnection of alloy particles or alloy particle fraction as the electrode contracts.

In general, the agreement between observed and predicted capacities are good and follow the same trend. The reversible capacity decreases with milling time for all samples during the first four hours of milling. This agrees with the compositional analysis of the previous chapter, as most

of the reaction between Si and W occurs during this stage. After this, the reaction is nearly complete, and the capacity decreases by a lesser amount. The agreement between the predicted and observed capacity trends in this regard is very good. The observed capacities for long milling times and high W content samples are less than would be predicted from the amount of Si phase present. In these samples, the large amount of W might result in some of the Si phase to become totally encased in inactive Si_2W and W phases. Such Si would be inaccessible to Li, resulting in the reduced capacity.

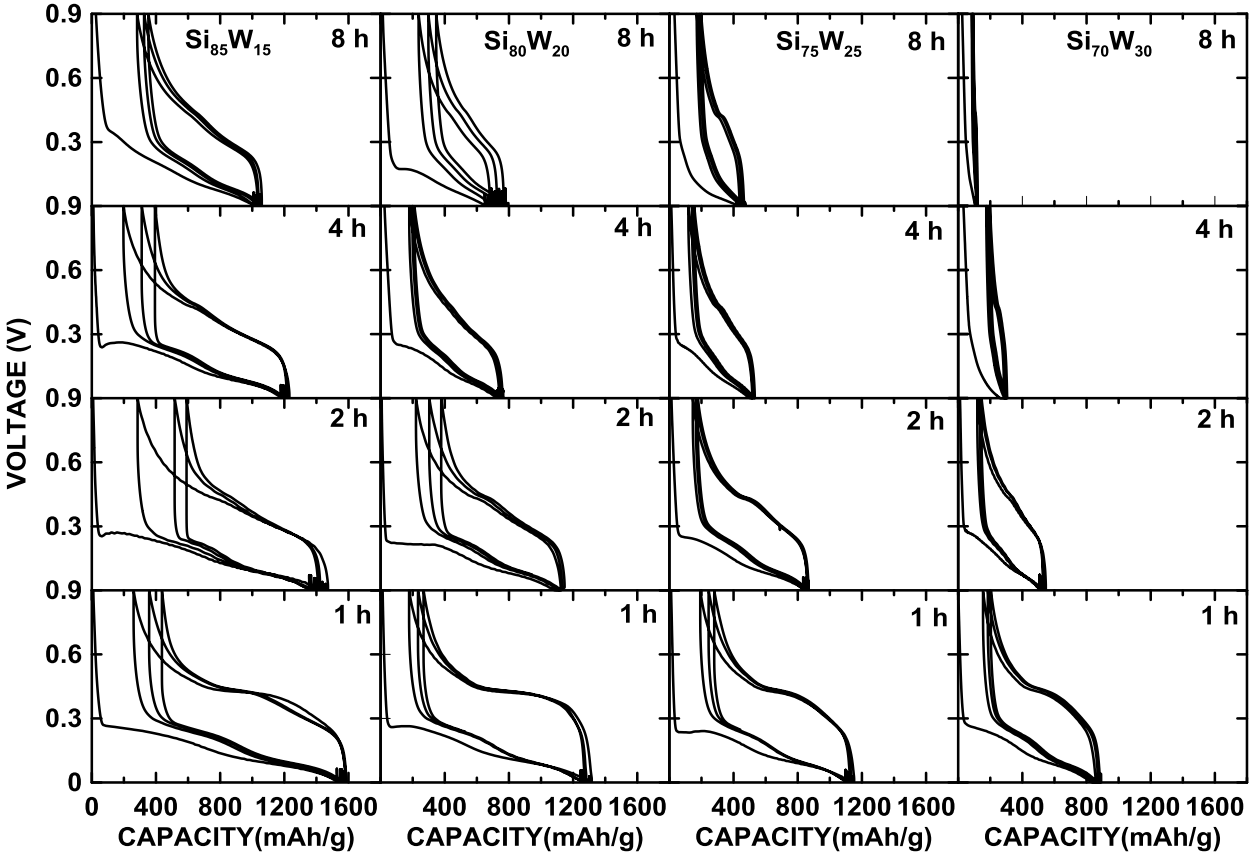

Figure 4.1 Voltage versus capacity curves of ball milled $Si_{85}W_{15}$, $Si_{80}W_{20}$, $Si_{75}W_{25}$ and $Si_{70}W_{30}$ at different milling times.

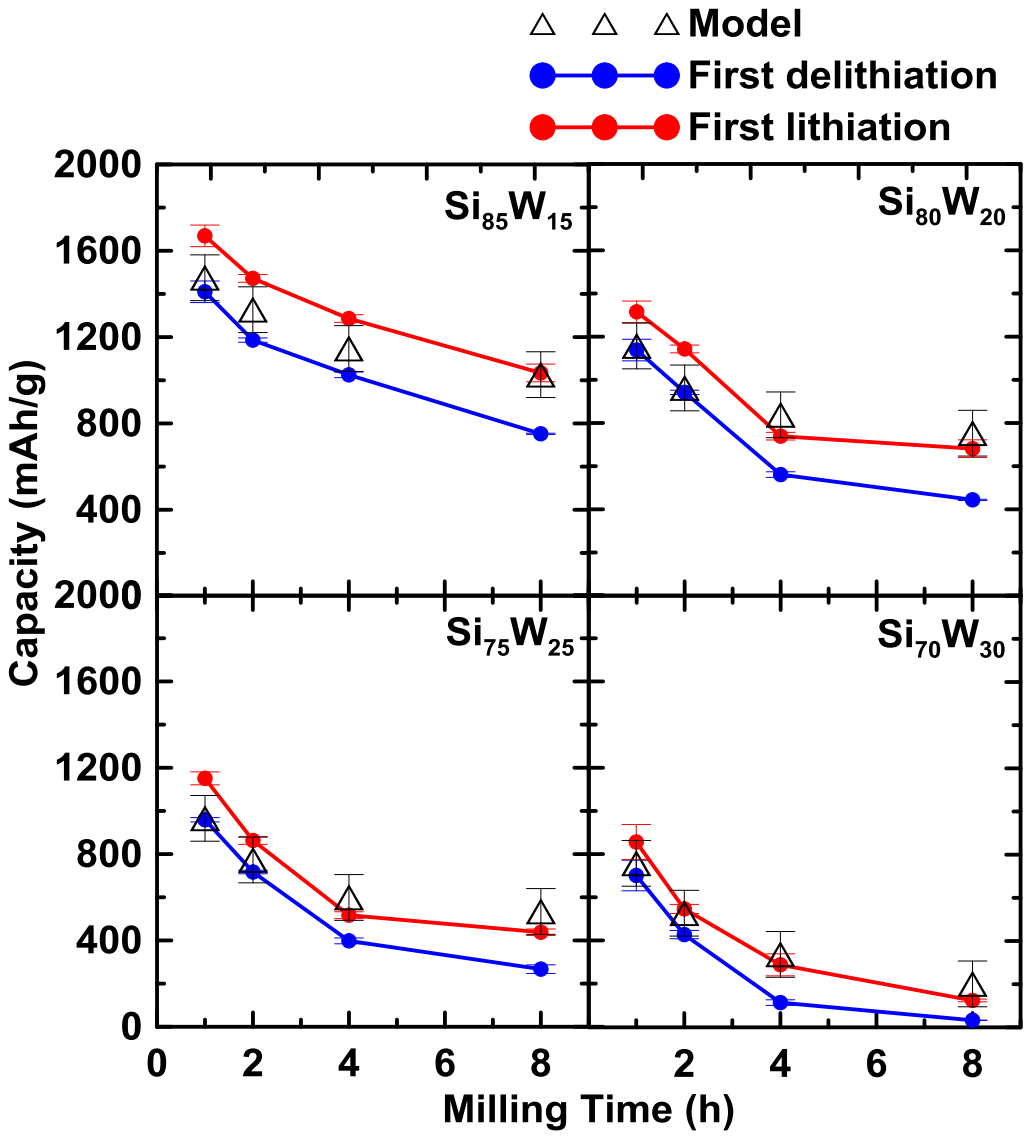

Figure 4.2 The first lithiation and delithiation capacities (error bars based on the standard deviation of 3-6 replicates) of all $Si_{100-x}W_x$ alloy compositions prepared at different milling times. Triangle symbol is representing the predicted capacities from XRD phase quantification.

Figure 4.3 shows the differential capacity curves derived from the voltage curves in Figure 4.1. In the differential capacity curves, a sharp peak occurs at about 0.28 V in some of the Si-W alloys during the first lithiation. This peak has been associated with a nucleation and growth process for

the initial lithiation step. As lithiation progresses, two broad peaks are then observed, corresponding to two single-phase lithiation processes that occur for amorphous Si. During delithiation, two corresponding broad peaks are observed which correspond to the delithiation of amorphous Si [15]. The two pairs of broad peaks indicate that amorphous Si is the only active phase in $Si_{100-x}W_x$ alloys. A sharp peak also appears at around 0.43 V during the delithiation of some samples. The 1 h milled $Si_{85}W_{15}$ alloy has the sharpest peak at 0.43 V during the first delithiation. This peak is associated with $Li_{15}Si_4$ formation. The peak is suppressed as milling time and W content are increased. Alloys with suppressed $Li_{15}Si_4$ formation are expected to exhibit improved electrochemical performance. It was reported that voltage shifts in the Si voltage profile occur in Si-Ni, Si-Fe, and Si-B active/inactive alloys [45][47][49][91]. These voltage shifts are thought to be induced by stress-voltage coupling between the active Si and the inactive phases. Such voltage shifts depend on the content of the inactive phase and could reach hundreds of millivolts. This is thought to result in the suppression of $Li_{15}Si_4$ formation in Si-M alloys. Here, no obvious voltage shift was observed in the Si-W system. Despite this, other characteristics are consistent with those reported Si-M active/inactive alloys.

Figure 4.4 shows specific capacities vs. cycle number of ball milled $Si_{100-x}W_x$ alloys (x = 15, 20, 25 and 30, milling time: 1 h, 2 h, 4 h, and 8 h). Capacity fade is observed for all 1 h ball milled alloys. As milling time increases, more stable cycling performance is observed. This might be ascribed to a more homogeneous microstructure where the Si regions and inactive phases are better dispersed. In addition, XRD patterns shown in Chapter 3 indicate that more inactive Si_2W is formed as milling time increases. The inactive Si_2W can buffer the volume expansion of Si-W alloys and better performance is therefore expected. In any case, the improved cycling performance is coincidental with the suppression of $Li_{15}Si_4$ formation. The 8 h milled alloys have the best

performance regarding capacity retention. However, the capacities of 8 h milled $Si_{75}W_{25}$ and $Si_{70}W_{30}$ are too low to be considered for practical application. Although the specific capacities of the 4 h and/or 8 h Si-W alloys made here (except the $Si_{85}W_{15}$ composition) are not an improvement over conventional graphite, some of the alloys exhibit far superior volumetric capacities because of their high density (4 h milled $Si_{80}W_{20}$ has a density of 5.80 g/cm^3). Volumetric capacities are shown in Figure 4.5. The 8 h ball milled $Si_{85}W_{15}$ and 4 h ball milled $Si_{80}W_{20}$ alloys can retain a high volumetric capacity of about 1500 Ah/L after 50 cycles.

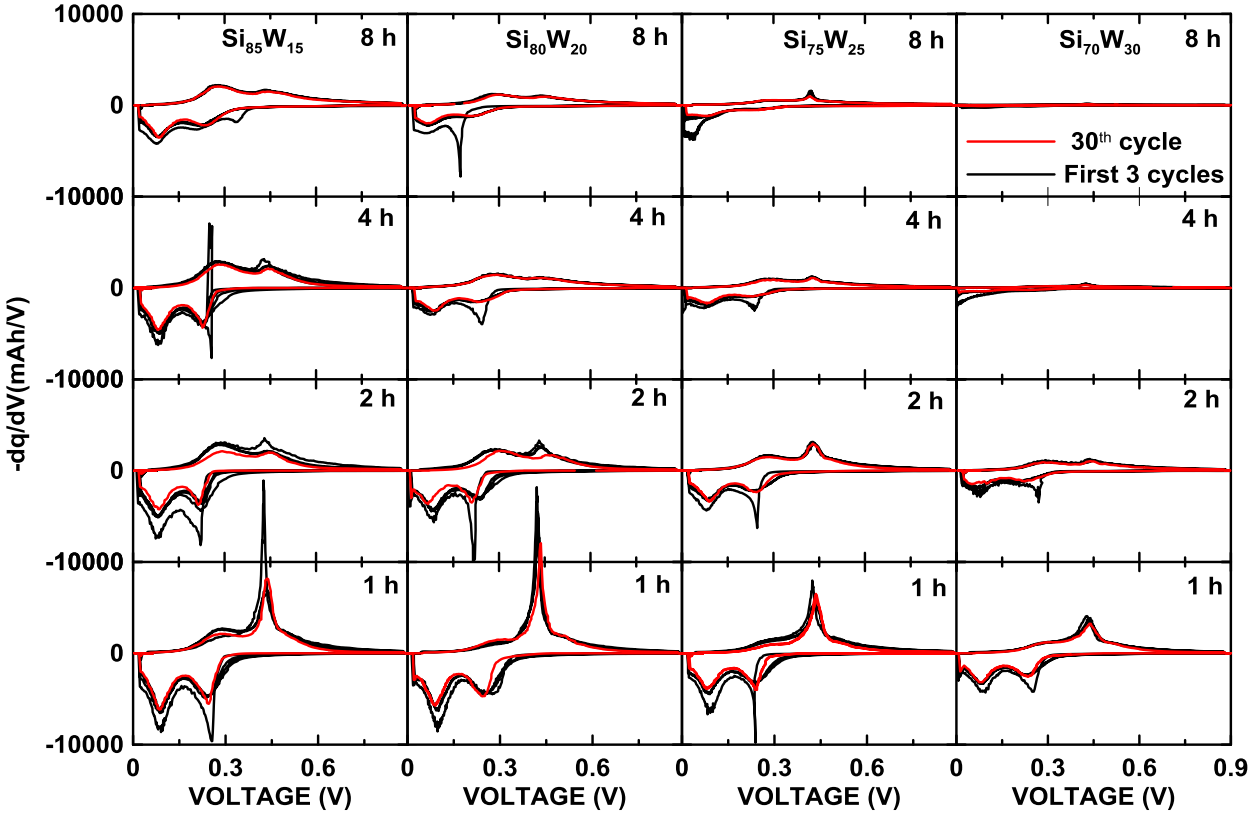

Figure 4.3 Differential capacity curves of the cells shown in Figure 4.1.

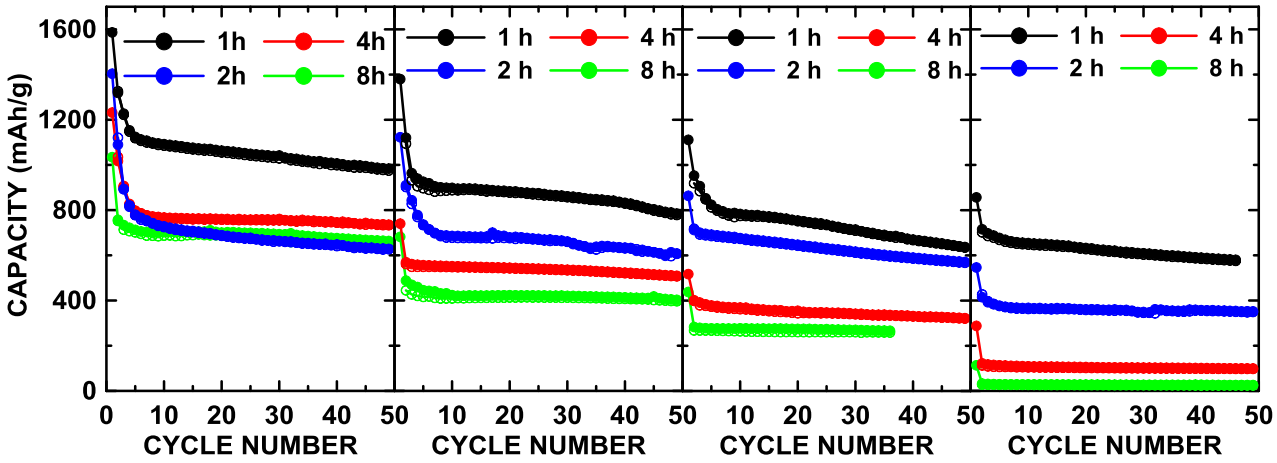

Figure 4.4 Specific capacity of ball milled $Si_{100-x}W_x$ versus cycle number, milling hours are indicated in different colors.

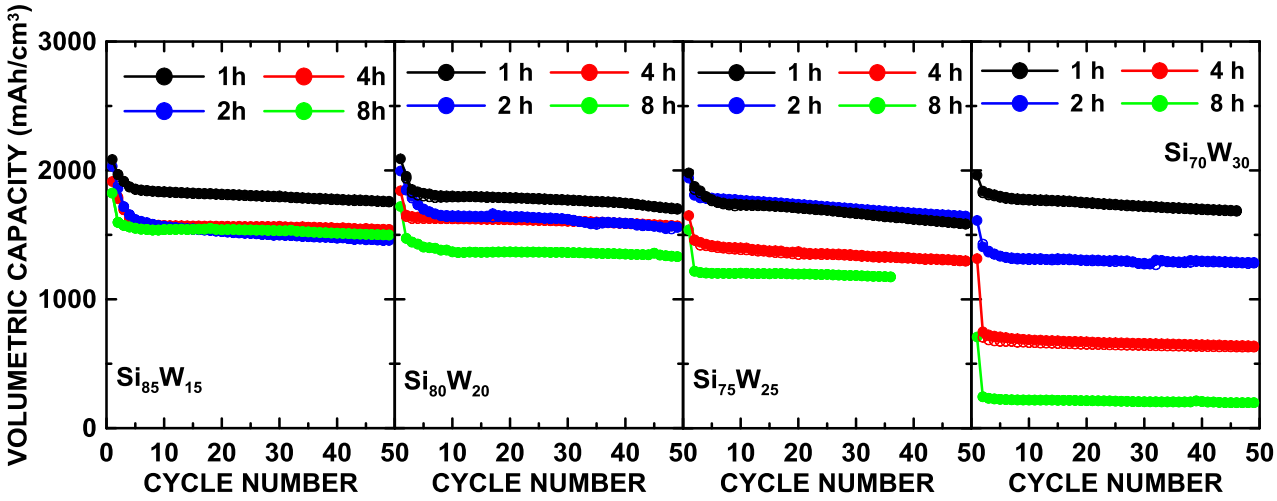

Figure 4.5 Volumetric capacity of ball milled $Si_{100-x}W_x$ versus cycle number, milling hours are indicated in different colors.

4.2 Electrochemical Performance of Alloys at Fixed Milling Time

In order to understand better the effect of alloy composition on electrochemical performance, the electrochemical performance of $Si_{100-x}W_x$ alloys made at the same milling time (4 h), but with different compositions is discussed in this section. Figure 4.6 shows the voltage curves (first three

cycles) and differential capacity curves (first three cycles and the 50th cycle) for the four 4 h milled samples made with different W content. There is a significant decrease in the capacity as the W content increases because of the increasing amount of the inactive Si_2W and, correspondingly, decreasing amount of active Si in each alloy. A small plateau at about 0.43 V during delithiation is observed for most of the 4 h milled alloys, which indicates the formation of crystalline $Li_{15}Si_4$. As shown above, this plateau can be completely suppressed with longer milling times. The differential capacity curves show this plateau as a peak during delithiation at about 0.43 V. This peak disappears after 50 cycles for all samples. Since the formation of $Li_{15}Si_4$ is associated with unconstrained Si (i.e., not bonded to an inactive phase), the $Li_{15}Si_4$ phase may be associated with loosely connected Si regions which can lose electrical connection during cycling, resulting in the observed preferential fade of the 0.43 V peak in the differential capacity. Again, unlike other Si-Ni, Si-Fe, and Si-B active/inactive alloys [45][47][49][91], no obvious voltage shift was observed in the 4 h milled Si-W alloys with different W contents.

Figure 4.7 shows the first lithiation and delithiation capacities of the 4 h ball milled $Si_{100-x}W_x$ (x = 15, 20, 25 and 30) alloys and the predicted capacities from XRD phase quantification. The observed first reversible capacity decreases as W content increases, changing from about 1000 mAh/g to 70 mAh/g, because of increasing formation of inactive Si_2W as the W content increases. The predicted capacities agree very well with the electrochemical results for $Si_{85}W_{15}$ and $Si_{80}W_{20}$ compositions, while the predicted values are slightly higher for those alloys with higher W contents (x = 25 and 30). As mentioned above, this may be due to some of the Si becoming isolated within inactive phases as the W content is increased.

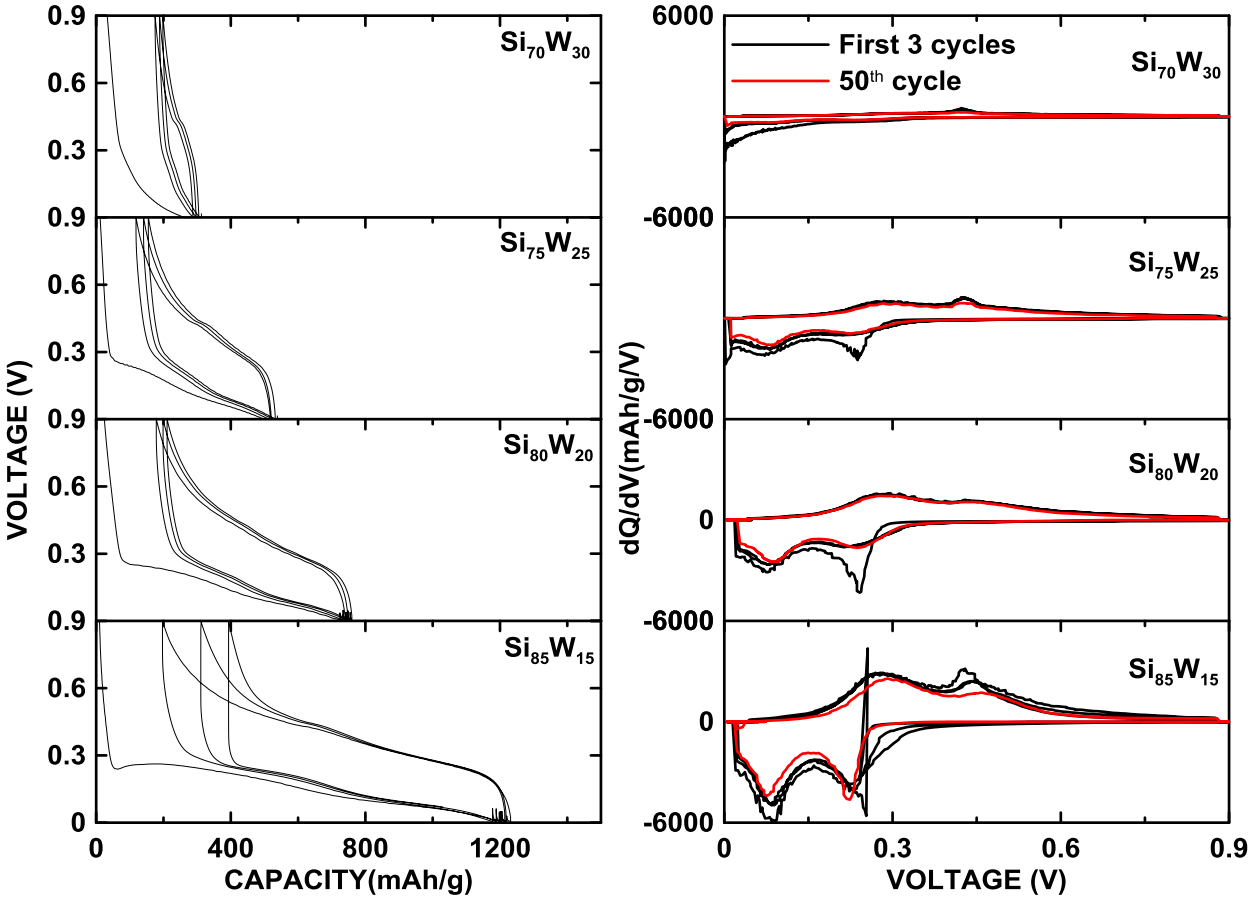

Figure 4.6 Voltage and differential capacity curves of 4 h ball milled $Si_{100-x}W_x$ (x = 15, 20, 25 and 30) alloys.

Figure 4.8 shows the cycling performance of 4 h ball milled $Si_{100-x}W_x$ made with different W contents. The top panel shows the specific capacity while the bottom panel indicates the volumetric capacity. The 4 h milled $Si_{85}W_{15}$ sample has rapid capacity fade during the first five cycles. This is typical behavior for alloys with excessively large capacity and volume expansion, which results in mechanical failure. The 4 h milled alloys at other compositions have stable cycling during the examined 50 cycles. It is also found that the volumetric capacity is less sensitive to the changes in the W content as compared with the specific capacity.

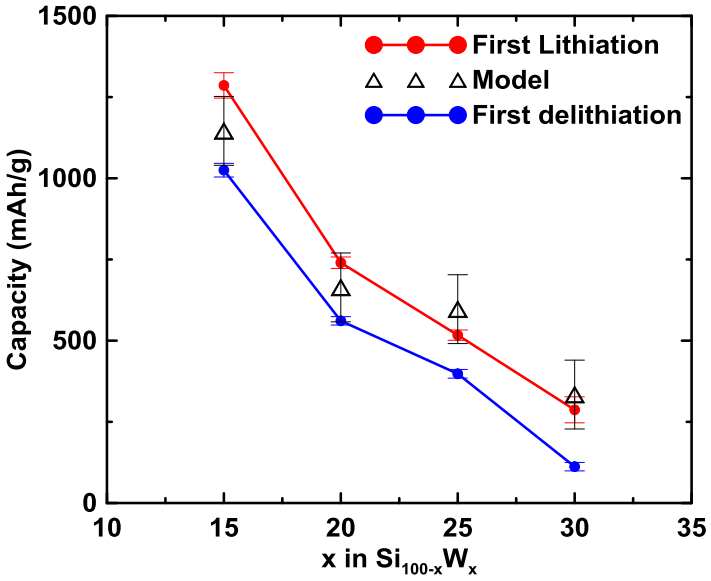

Figure 4.7 The first lithiation and delithiation capacities (error bars based on the standard deviation of 3-6 replicates) of 4 h milled $Si_{100-x}W_x$ (x = 15, 20, 25 and 30) alloys as measured in coin cells. Triangle symbols represent the predicted capacities from XRD phase quantification.

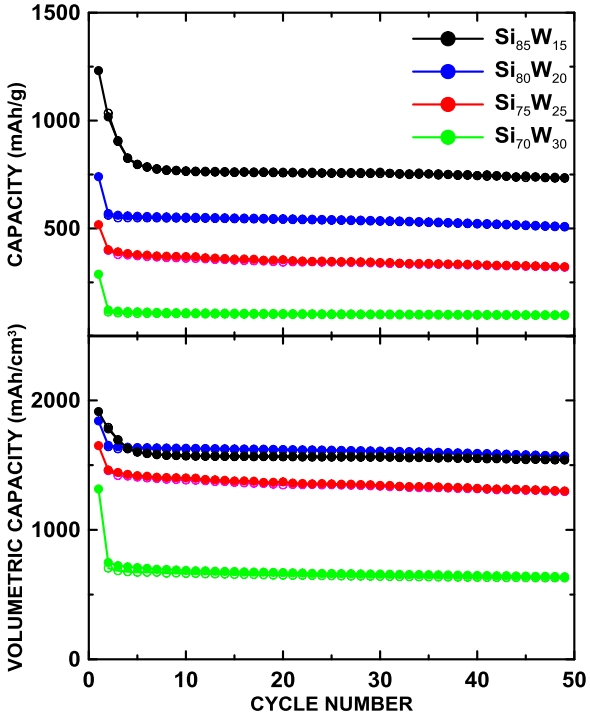

Figure 4.8 Specific (top) and volumetric (bottom) capacity of 4 h ball milled $Si_{100-x}W_x$ (x = 15, 20, 25, and 30) versus cycle number.

4.3 Electrochemical Performance of Annealed Samples

It was hoped that $Si_{100-x}W_x$ alloys could exhibit good thermal stability to enable high-temperature thermal processing. High temperature processing while maintaining the nanostructure is desirable to allow carbon coating, which can increase cycle life further [92]. Therefore, 4 h ball milled $Si_{100-x}W_x$ (x = 15, 20, 25 and 30) alloys were heated to high temperatures and their microstructure and electrochemistry were investigated. The diffraction patterns of ball milled Si-W alloys before and after annealing at 600°C and 800°C are shown in Figure 4.9. XRD patterns of 4 h ball milled Si-W alloys with different W content have similar phase content and comprise amorphous Si, nanocrystalline Si_2W, and residual crystalline W. The XRD patterns of 600°C annealed $Si_{100-x}W_x$ alloys are almost identical to the unheated $Si_{100-x}W_x$ alloys, while 800°C treatment causes crystallization of Si_2W. For compositions with low W content, a small shoulder appears at 28°, corresponding to crystallized Si.

Figure 4.10 shows the voltage profiles of Si-W alloys as milled and after different thermal treatments. The voltage profiles of all alloys are typical of Si-based alloys. The voltage curves of the 600°C annealed alloys are very similar to the as-milled alloys (discussed in section 4.2). This similarity between the as-milled alloys and the 600°C annealed alloys can also be found in the differential capacity curves shown in Figure 4.11. This similarity in the differential capacity curves indicates that the 600°C annealed alloys can still maintain very good $Li_{15}Si_4$ suppression, as evident by having no pronounced peak at 0.43 V. For the 800°C annealed alloys, a flat plateau is observed in the voltage curves for all examined Si-W alloys (Figure 4.10), and a sharp peak appears near 0.43 V in Figure 4.11 correspondingly. The sharpest 0.43 V peak appears for the 800°C annealed $Si_{85}W_{15}$ alloy, where the crystallization of Si can be identified from the XRD pattern

(Figure 4.9). The presence of the two-phase region peak seems to be coincidental with Si crystallization at 800°C. It is suspected that the microstructure of Si may have an effect on the $Li_{15}Si_4$ suppression [48]. Si crystallization is likely coincident with large Si regions in the grain structure. This means that there is likely a large amount of Si that is not connected with an inactive phase. Such free Si is associated with $Li_{15}Si_4$ formation.

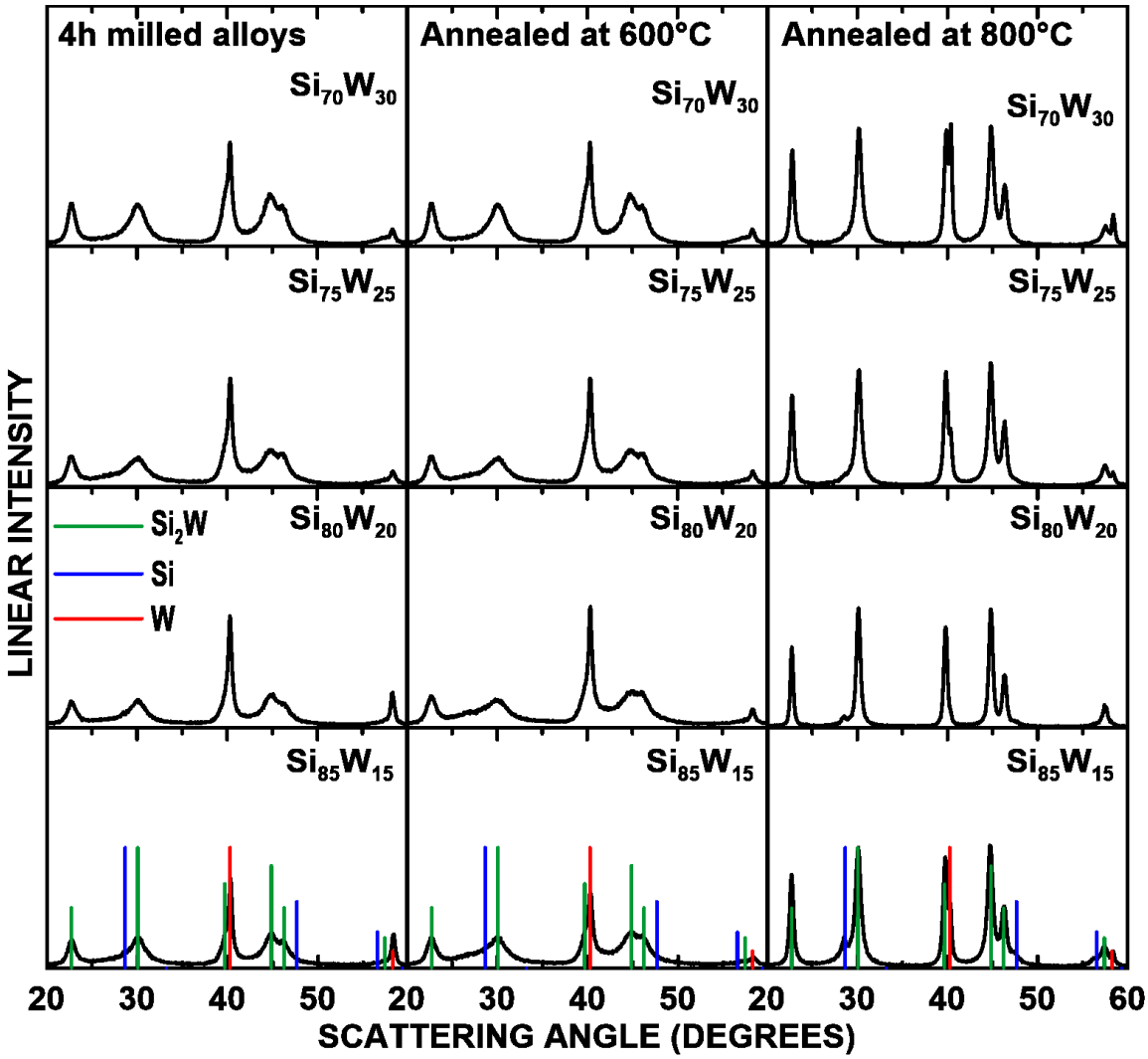

Figure 4.9 XRD patterns of 4 h milled $Si_{85}W_{15}$, $Si_{80}W_{20}$, $Si_{75}W_{25}$, and $Si_{70}W_{30}$ alloys as milled and after thermal annealing at 600°C and 800°C. Known phase peak positions and intensities are indicated by vertical lines.

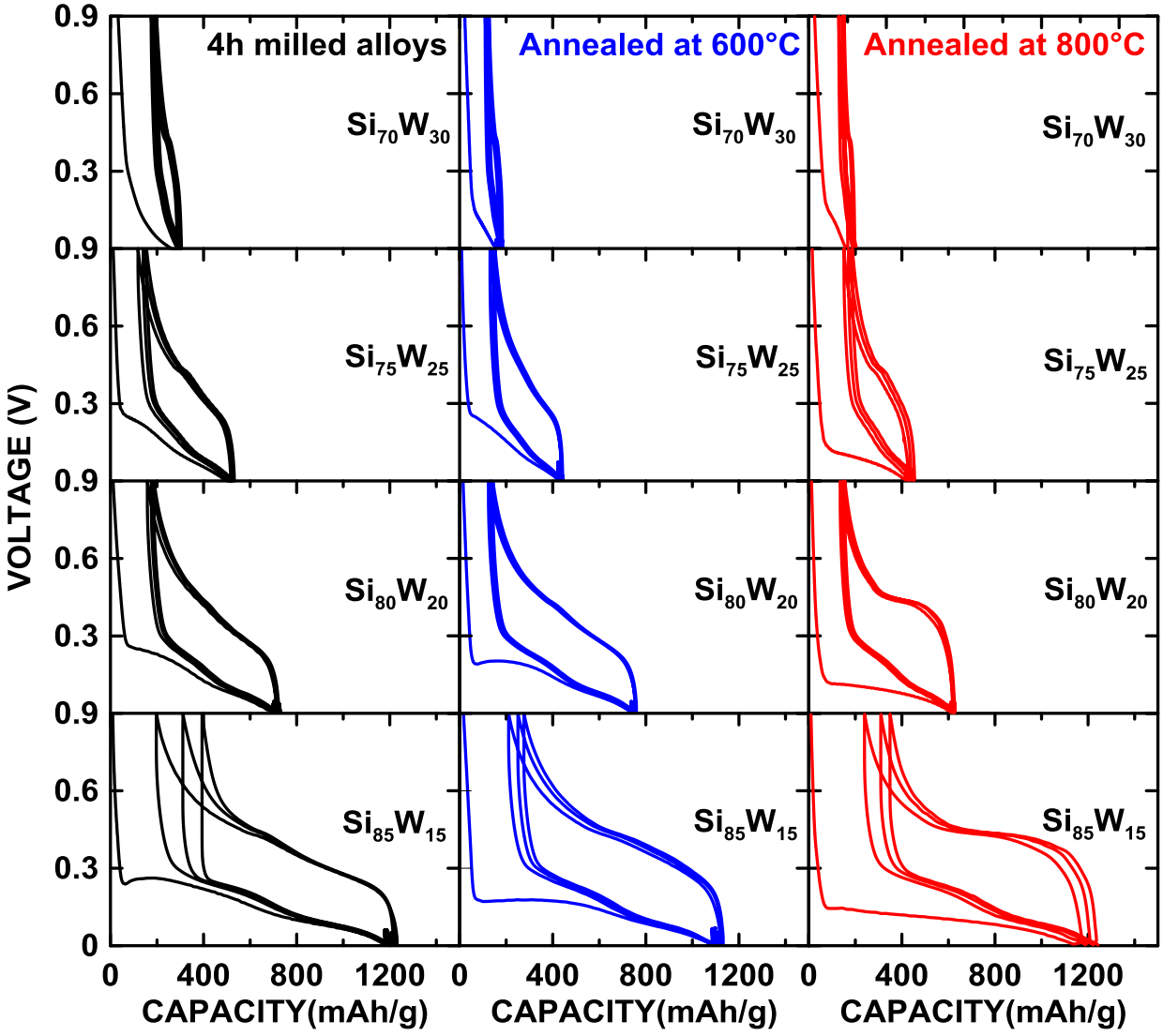

Figure 4.10 Voltage curves of 4 h milled $Si_{85}W_{15}$, $Si_{80}W_{20}$, $Si_{75}W_{25}$, and $Si_{70}W_{30}$ alloys as milled and after thermal annealing at 600°C and 800°C.

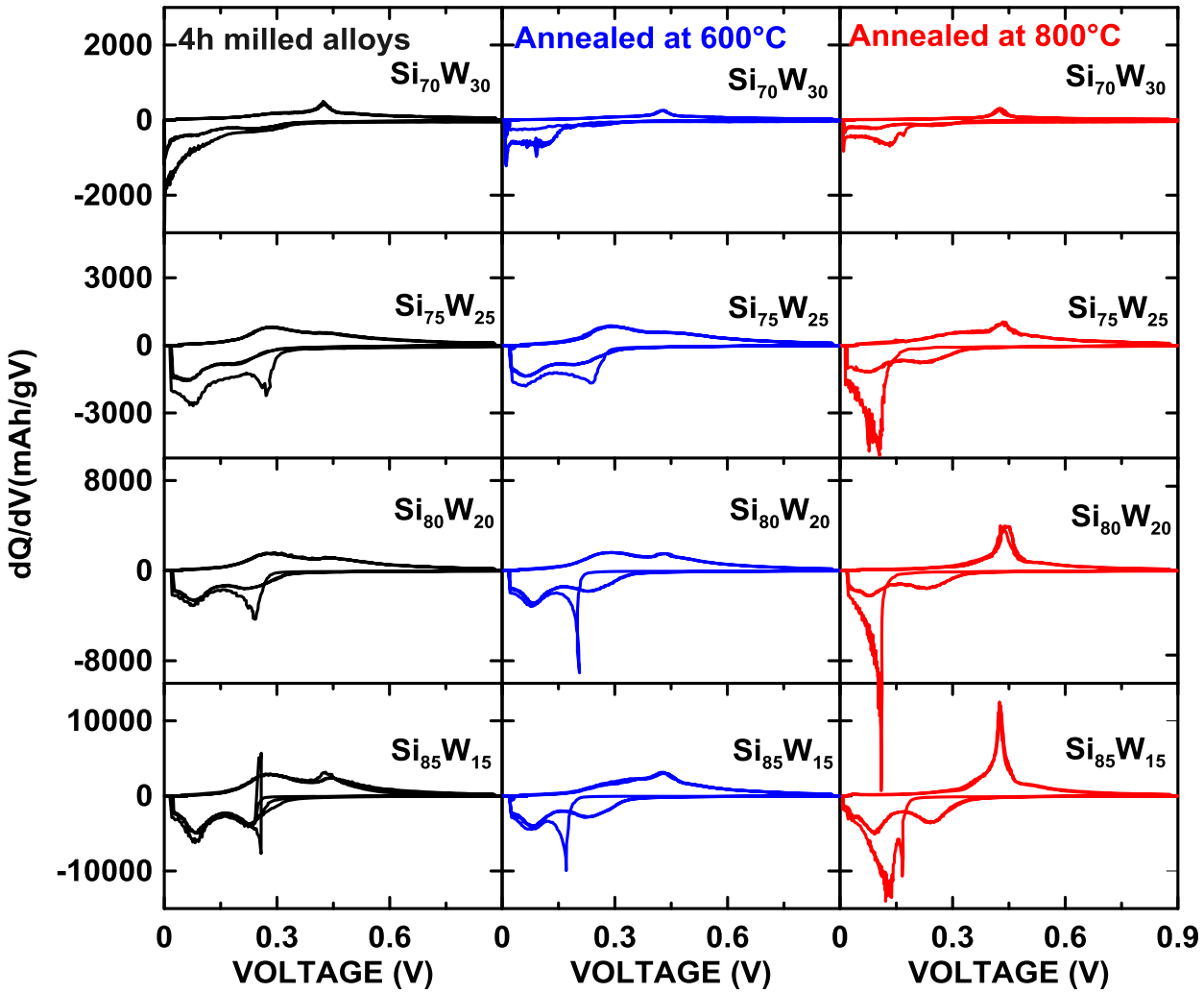

Figure 4.11 Differential capacity as a function of voltage for the alloys shown in Figure 4.10.

Figure 4.12 shows the first lithiation and delithiation capacities of Si-W alloys under different temperature treatments and their predicted capacities. As the temperature of the thermal treatment increases, a capacity reduction is observed in all four Si-W alloy compositions, possibly as a result of more inactive Si_2W being formed as the annealing temperature increases. The residual W in the unheated samples likely react with Si to form more inactive Si_2W during annealing, reducing the content of active Si. The predicted capacities are calculated from the quantified mole fractions of Si in the XRD patterns (assuming that all Si is active in the alloys and each Si atom can reversibly react with 3.75 Li atoms, while Si_2W and W are inactive). The capacity determined from XRD pattern phase analysis works well at all temperatures (as milled, 600°C annealed and 800°C annealed) and at lower W content (x = 15 and x = 20), where the predicted values are higher than the first delithiation capacity and lower than the first lithiation capacity, as discussed previously. However, the predicted values do not agree with the measured capacity of annealed alloys with higher W contents (x = 25 and 30). The Si in these samples may be more progressively encapsulated by the inactive phase and unavailable for cycling. For instance, although active Si is detected in the XRD pattern of the $Si_{70}W_{30}$ sample heated to 800°C, the material is essentially electrochemically inactive. Analysis of the microstructure of these alloys is needed to confirm this model.

The cycling performance of the alloys as milled and after annealing to 600°C and 800°C is shown in Figure 4.13 (in terms of specific capacity) and Figure 4.14 (in terms of volumetric capacity). The 600°C annealed $Si_{85}W_{15}$ and $Si_{80}W_{20}$ alloys exhibit specific capacities that are close to the unheated alloys, whereas the 600°C annealed $Si_{75}W_{25}$, 600°C annealed $Si_{70}W_{30}$ and 800°C annealed alloys at all compositions have decreased capacities. The reduced capacities are likely a result of more inactive Si_2W being formed during the high-temperature annealing step. The

residual W in the unheated samples likely reacts with Si to form this inactive phase during annealing. However, for $Si_{85}W_{15}$, $Si_{80}W_{20}$, and $Si_{75}W_{25}$, it was found that 600°C and 800°C heated samples show improved capacity retention, while their reversible capacity is nearly unchanged. As shown in Figure 4.14, the 800°C annealed $Si_{85}W_{15}$ and $Si_{80}W_{20}$ samples can maintain a high 1600 Ah/L capacity with almost no loss after 50 cycles. The 800°C annealed $Si_{75}W_{25}$ sample can maintain a volumetric capacity of around 1200 Ah/L after 50 cycles. This good thermal stability enables those alloys to be amenable towards high-temperature processing.

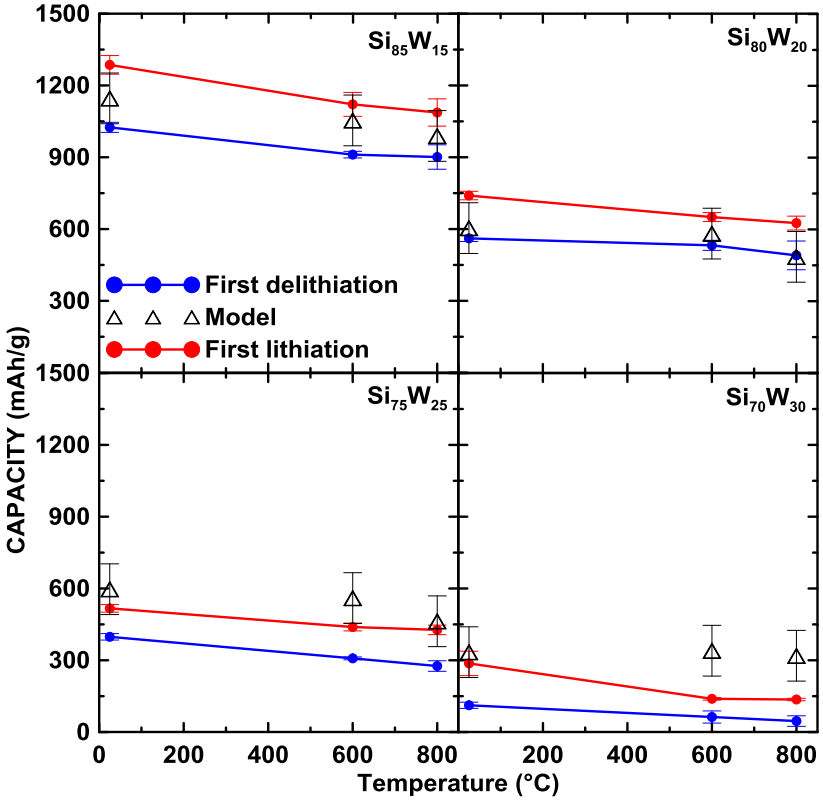

Figure 4.12 The first lithiation and delithiation capacities (error bars based on the standard deviation of 3-6 replicates) of Si-W alloys under different temperature treatments as measured in coin cells. Triangle symbols represent the predicted capacities from XRD phase quantification.

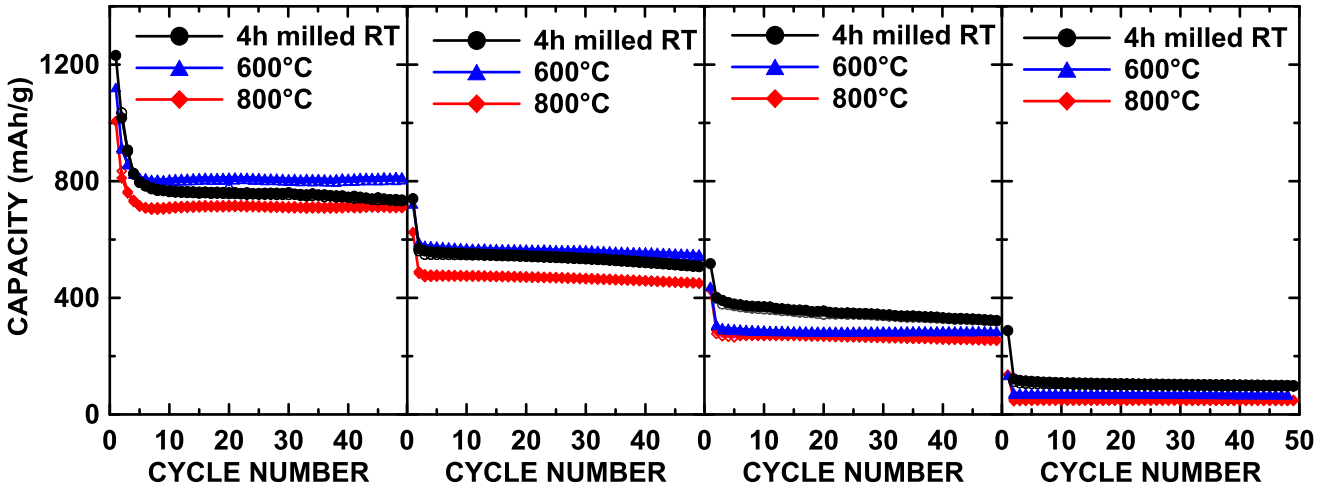

Figure 4.13 Specific capacity versus cycle number of alloys as milled and after annealing to 600°C and 800°C.

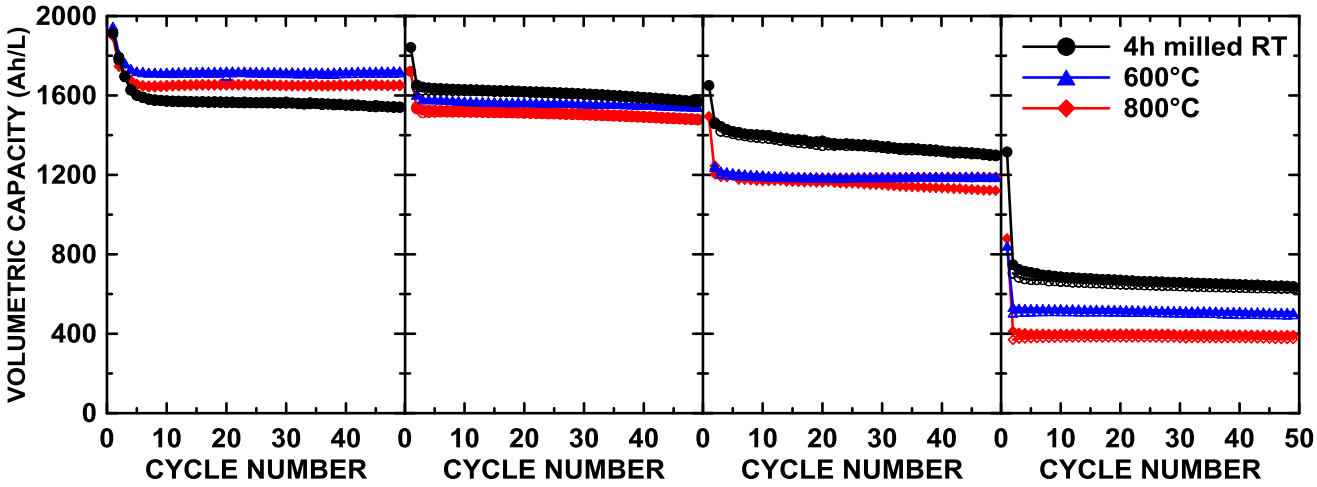

Figure 4.14 Cycling performance (volumetric capacity) of alloys as milled and after annealing to 600°C and 800°C.

4.4 Conclusion

In this chapter, the electrochemical behavior of ball milled $Si_{100-x}W_x$ alloys (x = 15, 20, 25 and 30) made at different milling times (1 h, 2 h, 4 h, and 8 h) was examined in Li cells. It was found that increasing milling time decreases the specific capacity as Si reacts with W to form inactive Si_2W during the milling process. It was also found that that increasing milling time can help improve the cycling stability and suppress the formation of $Li_{15}Si_4$. The 8 h milled $Si_{85}W_{15}$ alloy has a good balance of high volumetric capacity and good cycle life. The electrochemistry of $Si_{100-x}W_x$ alloys with different x values was also studied at a fixed milling time. Increasing the W content in the 4 h milled alloys was found to help suppress the formation of $Li_{15}Si_4$. The 4 h $Si_{80}W_{20}$ alloy exhibits a good overall performance (a reversible capacity of 1600 Ah/L and little formation of $Li_{15}Si_4$).

Selected ball milled $Si_{100-x}W_x$ (x = 15, 20, 25 and 30, milling time: 4 h) alloys were heated to test their thermal stability. As expected from XRD results, no significant changes can be observed between the voltage curves of the unheated and 600°C annealed alloys. The 600°C annealed alloys even show improved capacity retention. Although crystallization occurred in the 800°C annealed alloys and a more noticeable plateau at 0.43 V presented in the voltage curves, the 800°C annealed alloys still have good cycling stability with some decrease in the specific capacity. It is also found that the voltages curves of $Si_{100-x}W_x$ alloys with higher x value are less affected by the high-temperature treatment, as evident by no occurrence of the sharp peak at 0.43 V. In general, $Si_{100-x}W_x$ alloys have excellent thermal stability, even after being annealed to 800°C. Given the desire for high energy density, the 4 h milled $Si_{80}W_{20}$ alloy is an outstanding candidate among the examined alloys for use in commercial cells. It retains a volumetric capacity of 1600 Ah/L after 50 cycles with little $Li_{15}Si_4$ formation after high-temperature treatment.

CHAPTER 5 CONCLUSIONS AND FUTURE WORK

5.1 Conclusion

In this work, nanostructured $Si_{100-x}W_x$ (x = 15, 20, 25 and 30) alloys have been prepared by ball milling and the influence of milling time, W content and thermal treatments on the structure and electrochemistry were investigated. The XRD results suggest that the ball milled $Si_{100-x}W_x$ alloys are composed of amorphous Si, nanocrystalline Si_2W and residual crystalline W. The phase evolution, phase composition and grain size of ball milled Si-W alloys were quantitatively measured during the ball milling process. Ball milling was found to proceed in three stages with the amorphization of Si occurring after about 1 hour, followed by the reaction of Si with W to form Si_2W. After about 3 hours a steady state composition is reached. This milling process was successfully simulated by assuming constant volume element model and an activated process in which energy is accumulated after every collision. High W content Si-W alloys were found to form a W-rich cake at the side of the vial during the milling process, altering the final alloy composition.

Si-W alloys exhibit voltage profiles that are characteristic of amorphous Si. The presence of the inactive phase was found to suppress $Li_{15}Si_4$ formation during lithiation, resulting in improved cycling performance. The specific capacity suggests that amorphous Si is the only active phase while Si_2W and W are inactive with lithium. The 8 h milled $Si_{85}W_{15}$ and 4 h milled $Si_{80}W_{20}$ alloys exhibit good electrochemical performance, with little $Li_{15}Si_4$ formation, good cycling stability and high reversible volumetric capacities of ~1500 Ah/L or greater. Thermal stability was investigated for selected ball milled $Si_{100-x}W_x$ alloys (x = 15, 20, 25 and 30, milling time: 4 h). The Si-W alloys were found to have high thermal stability, with good cycling characteristics maintained, even after annealing to 800°C. The excellent thermal behavior enables the high-temperature processing while

maintaining a nanostructured morphology. This property is desirable for enabling carbon coating, which can increase cycle life further [92].

5.2 Future work

5.2.1 Comparisons to Other Si-M Systems

The mechanical milling method used in this study provides a convenient and scalable approach to synthesize nanostructured Si alloys with good electrochemical performance. The Obrovac group has investigated a series of Si-M alloys that synthesized through either magnetron sputtering or mechanical milling (Si-Ti, Si-V, Si-Cr, Si-Mn, Si-Fe, Si-Ni, Si-Cu, Si-Mo, Si-Mn and Si-W in this study). It is necessary to make comparisons between these different alloy materials both structurally and electrochemically. In Chapter 2, the milling process of Si-W alloys was successfully simulated by assuming a constant volume element model and an activated process in which energy is accumulated after every collision. The milling kinetics of Si-W alloys need to be compared in the future to other Si-M systems to assess manufacturability.

In addition, the presence of good thermally stability in Si-W alloys may correlate with the proprieties of the W phase. For example, the thermal stability of Si-Fe alloys prepared in the same way was examined. Figure 5.1 shows the resulting XRD patterns of unheated, 600°C annealed and 800°C annealed $Si_{80}Fe_{20}$. Unlike the 600°C annealed $Si_{80}W_{20}$ prepared similarly (see Figure 5.2), a small shoulder peak appears at 27.4° in the XRD pattern of a 600°C annealed $Si_{80}Fe_{20}$ alloy, indicating the formation of crystalline Si. However, the XRD patterns of 600°C annealed $Si_{100-x}W_x$ alloys are identical to those unheated. For 800°C annealed $Si_{80}Fe_{20}$, a distinct crystalline Si peak is observed. Only a small crystalline Si peak is observed in the 800°C annealed $Si_{80}W_{20}$ alloy.

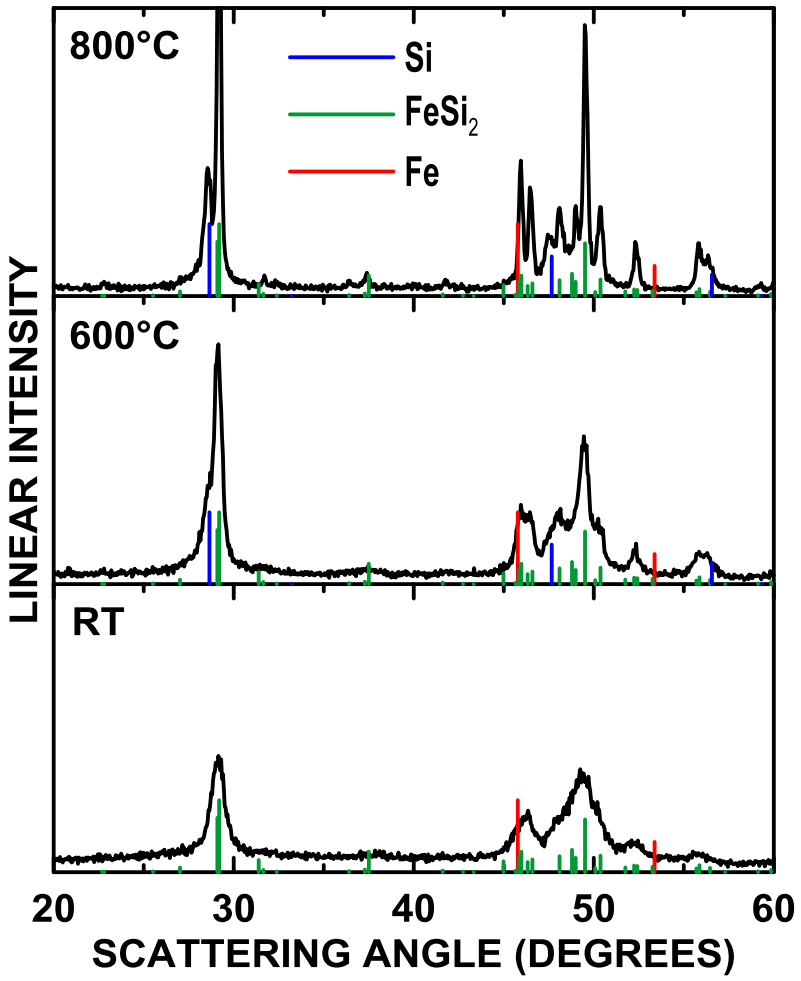

Figure 5.1 XRD patterns of unheated, 600°C annealed and 800°C annealed 4 h milled $Si_{80}Fe_{20}$.

The electrochemical performance of the alloys in Figure 5.1 and 5.2 are shown in Figure 5.3 and 5.4, respectively. For the $Si_{80}Fe_{20}$ alloy, a sharp peak at 0.43 V is evident both in 600°C annealed and 800°C annealed samples. In addition, 800°C annealed $Si_{80}Fe_{20}$ has a capacity fade. On the other hand, the $Si_{80}W_{20}$ alloy has excellent thermal stability at both annealing temperatures along with a comparable volumetric capacity maintained (~1500 mA/L). The difference in the thermal stability may correlate with the melting point of the silicide phase in each alloy. The

melting point of iron disilicide is 1212°C [93] while the melting point of tungsten disilicide is 2164°C [2]. Further comparisons between different Si-M systems are needed towards a full understanding of the thermal stability of Si-based alloys.

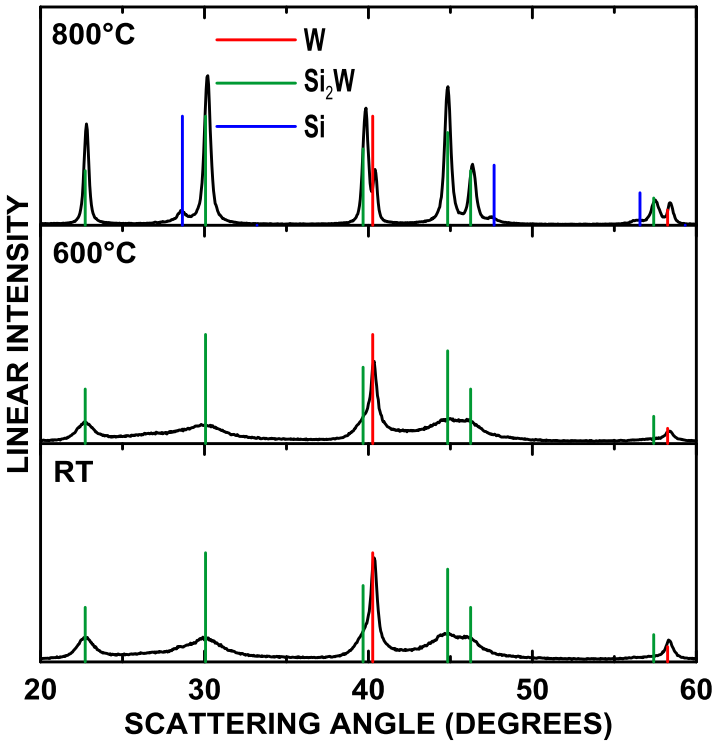

Figure 5.2 XRD patterns of unheated, 600°C annealed and 800°C annealed 4 h milled $Si_{80}W_{20}$.

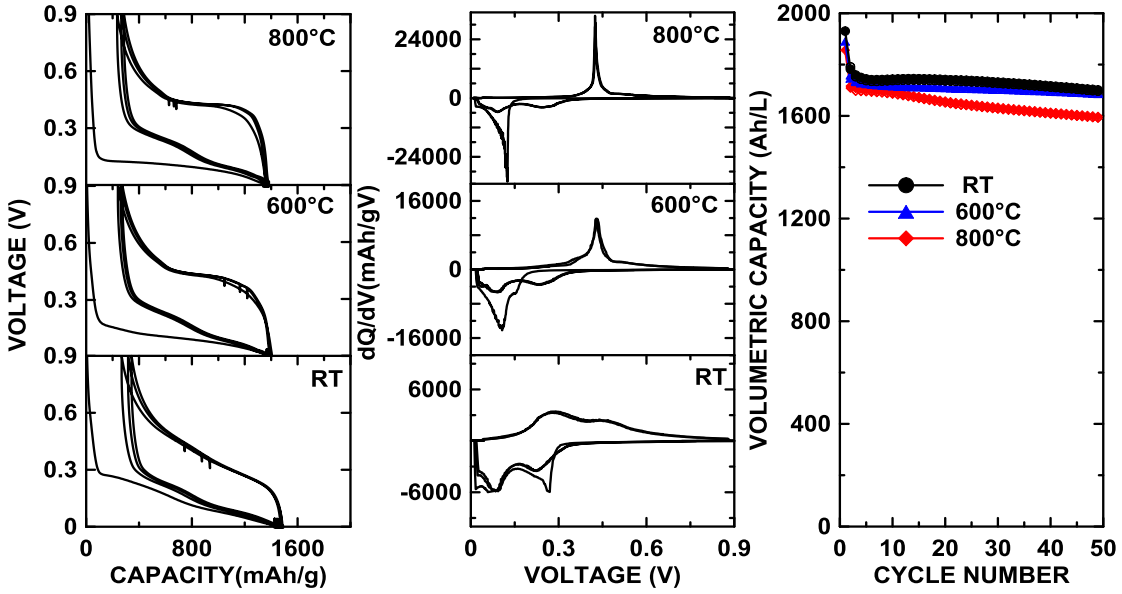

Figure 5.3 Electrochemical performance of 4 h milled $Si_{80}Fe_{20}$, 600°C annealed and 800°C annealed 4 h milled $Si_{80}Fe_{20}$ (From left to the right: voltage curves, differential curves, and cycling performance).

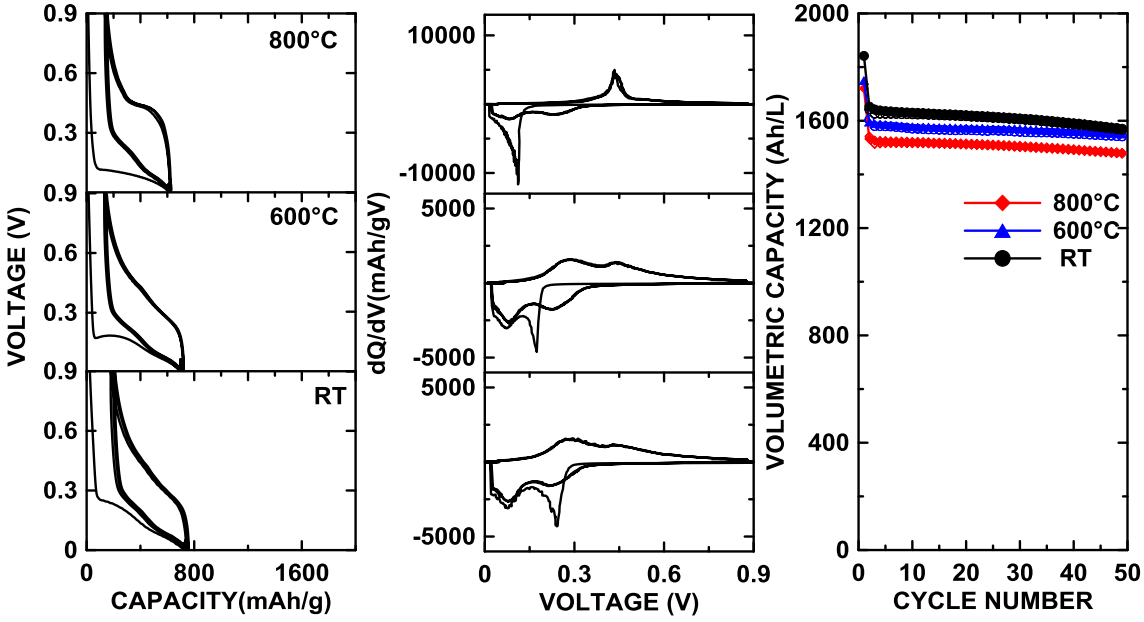

Figure 5.4 Electrochemical performance of 4 h milled $Si_{80}W_{20}$, 600°C annealed and 800°C annealed 4 h milled $Si_{80}W_{20}$ (From left to the right: voltage curves, differential capacity curves, and cycling performance).

5.2.2 Investigation of Contamination

The possibility for scaling up in manufacture is one of the major advantages of mechanical milling. However, the contamination from the milling media (balls and vial) is a serious problem [94]. For example, if stainless steel balls and vials are used, iron contamination may occur. Other milling media, like tungsten carbide or ceramics, can be used, but these are more expensive and contamination may still be a problem. It is said that the contamination problem is more serious for the high energy mills (e.g., the SPEX mill) while lower energy mills result in much less or negligible Fe contamination. The degree of contamination correlates with the properties of the powder being milled, chemical affinity of the power to the milling media and milling duration [94]. For instance, Eckert et al. show that the Fe contamination in milled powers depends on the hardness of the element being milled and the milling time. When milling soft elements such as Al, Cu, and Ni are SPEX milled, the iron contamination is well below 2 at.% even after extended milling (0.04 at.% Fe in Al and Cu after 24 hours of ball milling, and 1.6 at.% Fe in Ni after 40 h of ball milling). However, the Fe content exceeds 25 at.% after 8 h of milling in the case of hard elements such as Rh and Ir [95]. Some methods have been used to deal with contamination, such as the use of "process control agents". Mishurda *et al.* studied the effect of several process control agents on Fe contamination during the ball milling of $Ti_{50}Al_{48}W_2$ powders. It was found that boric acid and borax were effective in reducing Fe contamination (from 1.04 wt.% to 0.44 wt.% and 0.26 wt.%, respectively). Combined with the use of a “specially treated” vial (milling media coated with the alloy powder), the amount of Fe contamination can be reduced to 0.06 wt.% (with boric acid) and 0.09 wt.% (with borax) [96].

In this study, stainless steel balls and containers were used in a high energy ball mill. Iron contamination can be a problem. Therefore, it is important to study the iron contamination during this specified ball milling process. Ben Scott in our lab has shown that Mössbauer spectroscopy can be used to accurately quantify the amount of iron contamination. With the amount of contamination being identified, effective methods to minimize the contamination should be explored thereafter.

5.2.3 $Si_{100-x}W_x$ Alloy Optimization

It has been discussed in the introductory chapter that a stable SEI is desired to prevent further electrolyte decomposition and achieve long cycle life. However, it is not easy to maintain a stable SEI at a Si-based alloy electrode during cycling. This is because, upon the first lithiation, Si-based electrodes undergo volume expansion and a thin layer of SEI forms on the lithiated alloy surface. During delithiation, this SEI layer can be disturbed and fractured as electrode shrinks. The fractured SEI will cause fresh silicon surfaces be exposed to the electrolyte [97]. After many cycles, a very thick SEI layer with high resistance can form. The thick SEI layer may also result in electrical isolation of fractured particles and eventually lead to capacity fade [29].

Carbon coating, as a surface modification strategy, help stabilize the SEI layer of Si-based alloys. Not only that, the introduction of C can further buffer the volume expansion and improve the electrical conductivity of Si-based alloy materials [92]. However, carbon coating normally requires high-temperature processing (> 600°C). As discussed in Chapter 4, ball milled $Si_{100-x}W_x$ alloys exhibit excellent thermal stability even after annealing to 800°C. Therefore, carbon coatings should be considered as future work to optimize the $Si_{100-x}W_x$ alloy electrode.

Many studies have reported that nanostructured Si/C and SiO_x/C materials demonstrate excellent electrochemical performance [12][19][98][99][100]. In addition, the pre-lithiation method helps eliminate the irreversible capacity loss during the first cycle in SiO_x alloys, which greatly improves their energy density [18]. Good cycling staility is expected for SiO_x materials with optimum values of x [30]. Further optimizations on Si-based alloys may take advantage of the good performance of nanostructured Si/C and SiO_x/C (e.g., hybrid materials with metal alloys such as Si-W).

5.2.4 Furthering the Understanding of Si Alloy Electrochemistry

The understanding of electrochemical performance in this present study is mostly based on the knowledge of the lithiation/delithiation process of pure Si, where enormous and well-defined knowledge about this reaction has been obtained. However, different materials may exhibit different reaction mechanisms. Thus, it is important to learn these differences through more experimental characterization and modeling. Detailed studies of Si-based alloys and the effects of the microstructure on performance are highly desired. Research on the effects of volume expansion, deformation, stress evolution, and fracture of the electrode on the structural integrity, and electrochemical performance are needed [29]. The relation between the volume expansion and stress evolution to the observed electrochemical potential (such as the voltage plateau of $Li_{15}Si_4$) would be useful to study to better understand the physical processes occurring in an electrode structure during lithiation/delithiation.

Overall, more fundamental understanding of the electrochemistry and electrode development are required to clarify methods of preparing good Si-based alloys as negative electrodes via mechanical milling. Hopefully, the study presented here will help future researchers develop Si

containing anodes for Li-ion batteries with improved performance in a relatively economical and convenient way.

REFERENCES

[1] D. Linden, LINDEN'S HANDBOOK OF BATTERIES, 4th ed., McGraw-Hill, New York, 2011.

[2] K. Kimura, M. Nakamura, T. Hirano, J. Mater. Sci. 25 (1990) 2487–2492.

[3] J.M. Tarascon, M. Armand, Nature 414 (2001) 359–67.

[4] B. Scrosati, J. Hassoun, Y.-K. Sun, Energy Environ. Sci. 4 (2011) 3287.

[5] M. Yoshio, R.J. Brodd, A. Kozawa, eds., Lithium-Ion Batteries, Springer, New York, 2009.

[6] B. Scrosati, J. Garche, J. Power Sources 195 (2010) 2419–2430.

[7] M.S. Whittingham, Chem. Rev. 104 (2004) 4271–4302.

[8] A. Manthiram, J.C. Knight, S.T. Myung, S.M. Oh, Y.K. Sun, Adv. Energy Mater. 6 (2016).

[9] K. Xu, Chem. Rev. 104 (2004) 4303–4418.

[10] M.S. Ding, K. Xu, S.S. Zhang, K. Amine, G.L. Henriksen, T.R. Jow, J. Electrochem. Soc. 148 (2001) A1196.

[11] M.N. Obrovac, V.L. Chevrier, Chem. Rev. 114 (2014) 11444–11502.

[12] D. Larcher, S. Beattie, M. Morcrette, K. Edström, J.-C. Jumas, J.-M. Tarascon, J. Mater. Chem. 17 (2007) 3759.

[13] M.N. Obrovac, L. Christensen, D.B. Le, J.R. Dahn, J. Electrochem. Soc. 154 (2007) A849.

[14] M.D.F. and J.R.D. A.D.W.Todd, P.P.Ferguson, Int. J. Energy Res. (2010) 535–55.

[15] M.N. Obrovac, L.J. Krause, J. Electrochem. Soc. 154 (2007) A103.

[16] A. Hohl, T. Wieder, P.A. Van Aken, T.E. Weirich, G. Denninger, M. Vidal, S. Oswald, C. Deneke, J. Mayer, H. Fuess, J. Non. Cryst. Solids 320 (2003) 255–280.

[17] M.A. Al-Maghrabi, J. Suzuki, R.J. Sanderson, V.L. Chevrier, R.A. Dunlap, J.R. Dahn, J. Electrochem. Soc. 160160 (2013) 1587–1593.

[18] G. Ai, Z. Wang, H. Zhao, W. Mao, Y. Fu, R. Yi, Y. Gao, V. Battaglia, D. Wang, S. Lopatin, G. Liu, J. Power Sources 309 (2016) 33–41.

[19] M.L. Terranova, S. Orlanducci, E. Tamburri, V. Guglielmotti, M. Rossi, J. Power Sources 246 (2014) 167–177.

[20] N.-S. Choi, K.H. Yew, H. Kim, S.-S. Kim, W.-U. Choi, J. Power Sources 172 (2007) 404–409.

[21] Q. Fan, P.J. Chupas, M.S. Whittingham, Electrochem. Solid-State Lett. 10 (2007) A274–A278.

[22] A.D.W. Todd, P.P. Ferguson, J.G. Barker, M.D. Fleischauer, J.R. Dahn, J. Electrochem. Soc. 156 (2009) A1034.

[23] A.D.W. Todd, R.E. Mar, J.R. Dahn, J. Electrochem. Soc. 154 (2007) A597.

[24] A.D.W. Todd, R.E. Mar, J.R. Dahn, J. Electrochem. Soc. 153 (2006) A1998.

[25] Y. Tian, A. Timmons, J.R. Dahn, J. Electrochem. Soc. 156 (2009) A187.

[26] J. Li, D.B. Le, P.P. Ferguson, J.R. Dahn, Electrochim. Acta 55 (2010) 2991–2995.

[27] P.P. Ferguson, P. Liao, R.A. Dunlap, J.R. Dahn, J. Electrochem. Soc. 156 (2009) A13–A17.

[28] L. Christensen, D.B. Le, J. Singh, M.N. Obrovac, in:, Vienna, Austria, Conf. Abstr., 2009.

[29] M.T. McDowell, S.W. Lee, W.D. Nix, Y. Cui, Adv. Mater. 25 (2013) 4966–4985.

[30] J.-Y. Li, Q. Xu, G. Li, Y.-X. Yin, L.-J. Wan, Y.-G. Guo, Mater. Chem. Front. 44 (2017) 6749–6773.

[31] M.N. Obrovac, L. Christensen, Electrochem. Solid-State Lett. 7 (2004) A93–A96.

[32] J. Li, J.R. Dahn, J. Electrochem. Soc. 154 (2007) A156–A161.

[33] J. Li, A. Smith, R.J. Sanderson, T.D. Hatchard, R.A. Dunlap, J.R. Dahn, J. Electrochem. Soc. 156 (2009) A283.

[34] A.M. Wilson, J.R. Dahn, J. Electrochem. Soc. 142 (1995) 326.

[35] J.W. Choi, D. Aurbach, Nat. Rev. Mater. 1 (2016) 16013.

[36] A.M. Wilson, J. Electrochem. Soc. 142 (1995) 326.

[37] I. Ryu, J.W. Choi, Y. Cui, W.D. Nix, J. Mech. Phys. Solids 59 (2011) 1717–1730.

[38] S.P. Kim, A.C.T.V. Duin, V.B. Shenoy, J. Power Sources 196 (2011) 8590–8597.

[39] I.A. Courtney, J.R. Dahn, J. Electrochem. Soc. 144 (1997) 2045–2052.

[40] T.D. Hatchard, J.M. Topple, M.D. Fleischauer, J.R. Dahn, Electrochem. Solid-State Lett. 6 (2003) A129.

[41] T.D. Hatchard, J.R. Dahn, J. Electrochem. Soc. 151 (2004) A838–A842.

[42] O. Mao, R.L. Turner, I.A. Courtney, B.D. Fredericksen, M.I. Buckett, L.J. Krause, J.R. Dahn, Electrochem. Solid-State Lett. 2 (1999) 3–5.

[43] S.J. Lee, H.K. Baik, S.M. Lee, Electrochem. Commun. 5 (2003) 32–35.

[44] M.D. Fleischauer, J.M. Topple, J.R. Dahn, Electrochem. Solid-State Lett. 8 (2005) A137.

[45] Z. Du, R.A. Dunlap, M.N. Obrovac, J. Electrochem. Soc. 163 (2016) A2011–A2016.

[46] Y.L. Kim, H.Y. Lee, S.W. Jang, S.H. Lim, S.J. Lee, H.K. Baik, Y.S. Yoon, S.M. Lee, Electrochim. Acta 48 (2003) 2593–2597.

[47] Z. Du, S.N. Ellis, R.A. Dunlap, M.N. Obrovac, J. Electrochem. Soc. 163 (2016) A13–A18.

[48] Y. Wang, S. Cao, M. Kalinina, L. Zheng, L. Li, M. Zhu, M.N. Obrovac, J. Electrochem. Soc. 164 (2017) A3006–A3010.

[49] Z. Du, T.D. Hatchard, R.A. Dunlap, M.N. Obrovac, J. Electrochem. Soc. 162 (2015) A1858–A1863.

[50] S. Kawakami, M. Asao, Electrode Material for Anode of Rechargeable Lithium Battery, Electrode Structural Body Using Said Electrode Material, Rechargeable Lithium Battery Using Said Electrode Structural Body, Process for Producing Said Electrode Structural Body, and Process for, US006730434B1, 2004.

[51] P. Zuo, G. Yin, J. Alloys Compd. 414 (2006) 265–268.

[52] Y. Wang, J.M. Lee, X. Wang, Int. J. Hydrogen Energy 35 (2010) 1669–1673.

[53] X. Zhao, R.J. Sanderson, M.A. Al-Maghrabi, R.A. Dunlap, M.N. Obrovac, J. Electrochem. Soc. 164 (2017) A1165–A1172.

[54] K.M. Lee, Y.S. Lee, Y.W. Kim, Y.K. Sun, S.M. Lee, J. Alloys Compd. 472 (2009) 461–465.

[55] H.-Y. Lee, S.-M. Lee, J. Power Sources 112 (2002) 649–654.

[56] Z. Du, H. Liu, S.N. Ellis, R.A. Dunlap, M. Zhu, M.N. Obrovac, J. Electrochem. Soc. 163 (2016) A1275–A1279.

[57] T.D. Hatchard, A. Genkin, M.N. Obrovac, AIP Adv. 7 (2017).

[58] P. Le Brun, L. Froyen, L. Delaey, Mater. Sci. Eng. A 161 (1993) 75–82.

[59] M. Magini, A. Iasonna, F. Padella, Scr. Mater. 34 (1996) 13–19.

[60] G. Cocco, F. Delogu, L. Schiffini, J. Mater. Synth. Process. 8 (2000) 167–180.

[61] A.Q. He, Y.K. Wu, H.Q. Ye, D.X. Li, 31 (1996) 4165–4169.

[62] J.S. Benjamin, T.E. Volin, Metall. Trans. 5 (1974) 1929–1934.

[63] J.R. Harris, J.A.D. Wattis, J.V. Wood, Acta Mater. 49 (2001) 3991–4003.

[64] F. Miani, P. Matteazzi, D. Basset, J. Alloys Compd. 204 (1994) 151–156.

[65] I.F. Vasconcelos, R.S. de Figueiredo, J. Phys. Chem. B 107 (2003) 3761–3767.

[66] L.F. Novelline, R. A., & Squire, Squire's Fundamentals of Radiology., La Editorial, UPR, 2004.

[67] R.D. Deslattes, E.G. Kassler, P. Indelicato, L. De Billy, E. Lindroth, J. Anton, Rev. Mod. Phys. 75 (2003) 35–99.

[68] J. Camardese, Core-Shell Materials as Positive Electrodes in Lithium-Ion Batteries, Dalhousie University, 2015.

[69] J. Li, Study and Development of Layered Li-Ni-Mn-Co Oxide Positive Electrode Materials for Lithium Ion Batteries, Dalhousie University, 2016.

[70] JCPDS International Centre for Diffraction Data, PDF-2 (2002).

[71] F.H. Chung, J. Appl. Crystallogr. 7 (1974) 519–525.

[72] S. Hillier, Clay Miner. 35 (2000) 291–291.

[73] S.J. Chipera, D.L. Bish, Adv. Mater. Phys. Chem. 3 (2013) 47–53.

[74] H.M. Rietveld, J. Appl. Crystallogr. 2 (1969) 65–71.

[75] D.L. Bish, S.A. Howard, J. Appl. Cryst 21 (1988) 86–91.

[76] R.J. Hill, C.J. Howard, J. Appl. Crystallogr. 20 (1987) 467–474.

[77] M. Batchelder, G. Cressey, Clays Clay Miner. 46 (1998) 183–194.

[78] S.J. Chipera, D.L. Bish, J. Appl. Cryst 35 (2002) 744–749.

[79] G. Smith, D., Johnson, G., Scheible, A., Wims, A., Johnson, J., & Ullmann, Powder Diffr. 2 (1987) 73–77.

[80] P. Cressey, G., & Schofield, Powder Diffr. 11 (1996) 35–39.

[81] H. P. Klug and L. E. Alexander, X-Ray Diffraction Pro- Cedures for Polycrystalline and Amorphous Materials, John Wiley & Sons, Inc., New York, 1974.

[82] W. Zhou, Z.L. Wang, Scanning Microscopy for Nanotechnology: Techniques and Applications, Springer Science & Business Media, 2007.

[83] P. Echlin, Handbook of Sample Preparation for Scanning Electron Microscopy and X-Ray Microanalysis, Springer Science & Business Media, 2009.

[84] R.F. Egerton, Physical Principles of Electron Microscopy, Springer Science & Business Media, New York, 2005.

[85] R.A. Anani, A., & Huggins, J. Power Sources 38 (1992) 351–362.

[86] W. Zhang, J. Power Sources 196 (2011) 877–885.

[87] T.D. Hatchard, J.R. Dahn, J. Electrochem. Soc. 151 (2004) A838.

[88] I.F. Vasconcelos, R.S. De Figueiredo, Nanostructured Mater. 11 (1999) 935–946.

[89] C.C. Koch, J.D. Whittenberge, Intermetallics 4 (1996) 339–355.

[90] B.S. Murty, S. Ranganathan, Int. Mater. Rev. 43 (1998) 101–141.

[91] H. Liu, M. Zhu, Z. Du, M.N. Obrovac, J. Electrochem. Soc. 163 (2015) A192–A196.

[92] T. Kasukabe, H. Nishihara, S. Iwamura, T. Kyotani, J. Power Sources 319 (2016) 99–103.

[93] E. GroB, M. Riffel, J. Mater. Res. 10 (1995) 34–40.

[94] C.C. Koch, Nanostructured Mater. 9 (1997) 13–22.

[95] J. Eckert, J.C. Holzer, C.E. Krill, W.L. Johnson, J. Mater. Res. 7 (1992) 1751–1761.

[96] J. Mishurda, C. Suryanarayaua, F. Froes, Unpublished Work, 1994.

[97] H. Wu, G. Chan, J.W. Choi, I. Ryu, Y. Yao, M.T. McDowell, S.W. Lee, A. Jackson, Y. Yang, L. Hu, Y. Cui, Nat. Nanotechnol. 7 (2012) 310–315.

[98] A. Timmons, A.D.W. Todd, S.D. Mead, G.H. Carey, R.J. Sanderson, R.E. Mar, J.R. Dahn, J. Electrochem. Soc. 154 (2007) A865.

[99] C.-H. Doh, C.-W. Park, H.-M. Shin, D.-H. Kim, Y.-D. Chung, S.-I. Moon, B.-S. Jin, H.-S. Kim, A. Veluchamy, J. Power Sources 179 (2008) 367–370.

[100] D.L. Zhang, in:, Prog. Mater. Sci., 2004, pp. 537–560.

APPENDIX I

```
/*
 * To change this license header, choose License Headers in Project Properties.
 * To change this template file, choose Tools | Templates
 * and open the template in the editor.
 */
import java.util.*;
import java.util.concurrent.ThreadLocalRandom;

class Matrix implements Comparable<Matrix>{

   int A;
   int B;
   int C;
   double D;
   int E;
   int index;
   public Matrix()
   {
      this.A=0;
      this.B=0;
      this.C=0;
      this.D=0;
      this.E=0;
   }

   public Matrix(int a, int b, int c, int d, int e)
   {
      this.A = a;
      this.B = b;
      this.C = c;
      this.D = d;
      this.E = e;
   }

   public void set_A(int a)
   {
      this.A = a;
   }
   public void set_B(int b)
   {
      this.B = b;
   }
```

```
    public void set_C(int c)
    {
        this.C = c;
    }
    public void set_D(double d)
    {
        this.D = d;
    }
    public void set_E(int e){
        this.E = e;
    }

    public void increase_D(double energy)
    {
        this.D = this.D + energy;
    }
    public void set_index(int i)
    {
        this.index = i;
    }

    @Override
    public int compareTo(Matrix compareFruit) {

        double compareQuantity = ((Matrix) compareFruit).D;
        return (int)(this.D - compareQuantity);
    }
}

class Result {

    int M;
    int N;
    long L;
    int K;
    int COLLISION;
    int round;

    public Result()
    {
        M=N=round=0;
        K = 0;
        COLLISION = 0;
        L=0;
    }
```

```
}

class SimulationResult{
   Vector<Result> results = new Vector<>();
   Result [] r_array;

   public SimulationResult(Vector<Result> results, Result[] r_array){
      this.r_array = r_array;
      this.results = results;
   }
}

class Best_result
{
   double diff;
   Result [] best_result;
   int sample_size;
   double enery_E;
   double enery_barrier;
   Vector<Result> result1 = new Vector<Result>();

   public Best_result()
   {
      best_result = new Result[4];
      diff = Double.MAX_VALUE;
      for(int i = 0; i < 4; i++)
      {
         best_result[i] = new Result();
      }
      enery_E = 0;
      enery_barrier = 0;
   }
}


public class JavaApplication1 {


   //shuffle an int array
   static void shuffleClass(Matrix[] ar) {
      // If running on Java 6 or older, use `new Random()` on RHS here
      Random rnd = ThreadLocalRandom.current();
      for (int i = ar.length - 1; i > 0; i--) {
         int index = rnd.nextInt(i + 1);
         // Simple swap
```

```
            int a = ar[index].A;
            ar[index].A = ar[i].A;
            ar[i].A = a;
        }
    }

    static int binary_search_result(Vector<Result> r, int key) {
        int low = 0, high = r.size() - 1; // numElems is the size of the array i.e arr.size()
        while (low != high) {
            int mid = (low + high) / 2; // Or a fancy way to avoid int overflow
            int mid_result = r.get(mid).round;
            if (mid_result <= key) {
                low = mid + 1;
            } else {

                high = mid;
            }
        }
        return low;
    }

    static void generate_simulation(long L, int STEPS, int NUM_SAMPLE, int NUM, double
energy, double energy_barrier, Best_result b_r)
    {
//      System.out.println("generate_simulation => energy_barrier: " + energy_barrier );
        SimulationResult result1 = simulation(8776, 1224, 40, L, STEPS, NUM_SAMPLE,
NUM, energy, energy_barrier);

        if (result1.results.size() > 0)
        {

            for (int i = 0, j = 3; i < 4 && j >= 0; i++, j--) {
                int div = (int) Math.pow(2, j);
                int cur_value = STEPS / div;
                int cur_index = binary_search_result(result1.results, cur_value);
                if (cur_index - 1 < 0) {
                    cur_index = 1;
                }
                result1.r_array[i].round = result1.results.get(cur_index - 1).round;
                result1.r_array[i].M = result1.results.get(cur_index - 1).M;
                result1.r_array[i].N = result1.results.get(cur_index - 1).N;
                result1.r_array[i].L = result1.results.get(cur_index - 1).L;
                result1.r_array[i].K = result1.results.get(cur_index - 1).K;
                result1.r_array[i].COLLISION = result1.results.get(cur_index - 1).COLLISION;
            }
```

```
            //calculate the differation
            double[] real_result = {87.83443221, 81.61395212, 70.36951599, 65.96504052};

            double[] simul_result = new double[4];
            for (int i = 0; i < simul_result.length; i++) {
               simul_result[i] = (result1.r_array[i].M / (double) (result1.r_array[i].M +
result1.r_array[i].N + result1.r_array[i].L)) * 100;
            }

            double cur_diff = 0;
            for (int i = 0; i < simul_result.length; i++) {
               cur_diff = cur_diff +  Math.pow((real_result[i] - simul_result[i]), 2) / simul_result[i]
;
            }

            //store the results in the best array
            if (cur_diff < b_r.diff) {
               b_r.diff = cur_diff;
               for (int i = 0; i < result1.r_array.length; i++) {
                  b_r.best_result[i].round = result1.r_array[i].round;
                  b_r.best_result[i].M = result1.r_array[i].M;
                  b_r.best_result[i].N = result1.r_array[i].N;
                  b_r.best_result[i].L = result1.r_array[i].L;
                  b_r.best_result[i].K = result1.r_array[i].K;
                  b_r.best_result[i].COLLISION = result1.r_array[i].COLLISION;
               }

               b_r.result1 = result1.results;
               b_r.enery_E = energy;
               b_r.enery_barrier = energy_barrier;
            }
         }

      }

      static  SimulationResult simulation(int M, int N, int ECount, long L, int STEPS, int
NUM_SAMPLE, int NUM, double energy, double energy_barrier){
   //       System.out.println("simulation => energy_barrier: " + energy_barrier );
   //       System.out.println("In simulation(): M is: " + M  + " N is: " + N);
         //allocate double array
         int[] sample_Index = new int[NUM_SAMPLE];//used to store index of sample array

         //declear a matrix
         Matrix[] Mx = new Matrix[NUM];
```

```
for(int i = 0; i < Mx.length; i++)
{
   Mx[i] = new Matrix();
}

//initial array values
//set the first M array to be 1
for (int i = 0; i < M; i++) {
   Mx[i].A = 1;
}
//set the rest NUM - M to be 0
for (int i = M; i < NUM; i++) {
   Mx[i].A = 0;
}

//shuffle array A
shuffleClass(Mx);

//initial the rest arrays
for (int i = 0; i < NUM; i++)
{
   //System.out.println( arrayA[i]);
   if (Mx[i].A == 0)
   {
      if(ECount-- > 0){
         Mx[i].E = 1;
      }
      else{
         Mx[i].B = 1;
      }
   }
   else
   {
      Mx[i].B = 0;
      Mx[i].E = 0;
   }
   Mx[i].C = 0;
   Mx[i].D = 0;
   //store the index
   Mx[i].index = i;
}

//add all the result into an array list
ArrayList<Matrix> ar_mx = new ArrayList <Matrix>();
for(int i = 0; i < NUM; i++)
```

```
{
   ar_mx.add(Mx[i]);
}

//start to run iterations
int count = 0;
//set the random
Random random = ThreadLocalRandom.current();

Vector <Result> result = new Vector<Result>();
//put the results into an result array and free the previous vector
Result [] r_array = new Result [4];
for(int i = 0; i < r_array.length; i++)
{
   r_array[i] = new Result();
}


while (count++ <= STEPS) {
   //record the signiture values
   if(count == STEPS / 8)
   {
      r_array[0].M = M;
      r_array[0].L = L;
      r_array[0].N = N;
      r_array[0].round = count;
      r_array[0].K = NUM_SAMPLE;
      r_array[0].COLLISION = STEPS;

   }
   else if (count == STEPS / 4)
   {
      r_array[1].M = M;
      r_array[1].L = L;
      r_array[1].N = N;
      r_array[1].round = count;
      r_array[1].K = NUM_SAMPLE;
      r_array[1].COLLISION = STEPS;
   }
   else if (count == STEPS / 2)
   {
      r_array[2].M = M;
      r_array[2].L = L;
      r_array[2].N = N;
      r_array[2].round = count;
```

```
            r_array[2].K = NUM_SAMPLE;
            r_array[2].COLLISION = STEPS;
        }
        else if (count == STEPS)
        {
            r_array[3].M = M;
            r_array[3].L = L;
            r_array[3].N = N;
            r_array[3].round = count;
            r_array[3].K = NUM_SAMPLE;
            r_array[3].COLLISION = STEPS;
        }

        //get NUM_SAMPLES of valid input
        int count_sample = 0;

        while (count_sample < NUM_SAMPLE)
        {
            int index = random.nextInt(ar_mx.size() - 1);
            if(ar_mx.get(index).A + ar_mx.get(index).B + ar_mx.get(index).C != 0)
            {
                sample_Index[count_sample] = index;//store the found index into another index
array
                ar_mx.get(index).increase_D(energy);
                count_sample++;

            }

        }

        //get the sum of A and B
        double sum_A = 0, sum_B = 0;
        boolean valid_d = true;
        for (int i = 0; i < NUM_SAMPLE; i++)
        {
            //get sum A and sum B
            sum_A = sum_A + ar_mx.get(sample_Index[i]).A;
            sum_B = sum_B + ar_mx.get(sample_Index[i]).B;
            //this represents d_i >= 5
            ////////////////////////energy barrier
            if (ar_mx.get(sample_Index[i]).D < energy_barrier)
            {
                valid_d = false;
            }
        }
```

```
if (sum_A >= 5 && sum_B >= 2 && valid_d)
{

   for (int i = 0; i < NUM_SAMPLE; i++)
   {
      array_sample[i] = new Matrix();
      array_sample[i].A = ar_mx.get(sample_Index[i]).A;
      array_sample[i].B = ar_mx.get(sample_Index[i]).B;
      array_sample[i].C = ar_mx.get(sample_Index[i]).C;
      array_sample[i].D = ar_mx.get(sample_Index[i]).D;
      array_sample[i].index = sample_Index[i];
   }

   Arrays.sort(array_sample);

   int count_a = 0, count_c = 0, count_b = 0;
   for (int i = 0; i < array_sample.length; i++) {
      if (array_sample[i].A == 1 && count_a < 5) {
         ar_mx.get(array_sample[i].index).set_A(0);
         count_a++;
      }
      if (array_sample[i].A == 1 && count_c < 5) {
         ar_mx.get(array_sample[i].index).set_C(1);
         count_c++;
      }
      if (array_sample[i].B == 1 && count_b < 2) {
         ar_mx.get(array_sample[i].index).set_B(0);
         count_b++;
      }
   }

   int m = 0;
   int n = 0;
   for(int ar_count = 0; ar_count < array_sample.length; ar_count++){
      Matrix x = array_sample[ar_count];
      if(x.D > energy_barrier && x.A == 1){
         m += 1;
      }
      else if(x.B == 1 && x.D > energy_barrier){
         n += 1;
      }
   }
```

```
            System.out.println("m is: " + m + ", n is: " + n);

            if(n%2 == 0 && m/5 >= n/2){
               M = M - 5*(int)Math.round(n/2);
               N = N - n;
               L = L + 5*(int)Math.round(n/2);
            }
            else if(n%2 == 0 && m/5 < n/2){
               M = M - m;
               N = N - 2*(int)Math.round(m/5);
               L = L + m;
            }


            //remove the empty box
            for (int i = 0; i < ar_mx.size(); i++) {
               if (ar_mx.get(i).A + ar_mx.get(i).B + ar_mx.get(i).C == 0) {
                  ar_mx.remove(i);
               }
            }

            //reset the index
            //System.out.println(" Round " + count +": " + M + "," + N + "," + L);
            if (N > 0) {
               Result r = new Result();
               r.M = M;
               r.L = L;
               r.N = N;
               r.round = count;
               r.COLLISION = STEPS;
               r.K = NUM_SAMPLE;
               result.add(r);
            } else {
               break;
            }
         }
      }

      return new SimulationResult(result, r_array);
   }

   public static void main(String[] args) {

      Best_result b_r = new Best_result();
      //get all the input data
```

```
        Scanner scanner = new Scanner(System.in);
        System.out.println("Please input samples initial number: (k)"); //k start
        String string_s = scanner.nextLine();

        System.out.println("Please input initate energy: ");
        String string_energy = scanner.nextLine();
        System.out.println("Please input initate energy barrier: ");
        String string_energy_barrier = scanner.nextLine();
        System.out.println("Please input number of simulated collision at each step (collision initial number): ");
        String string_SETPS = scanner.nextLine();

        Random rand = new Random();
        Random r = new Random();

        // some important parameters
        int NUM = 10000;//total number of matrix
        long L = 0; //initial L to be zero
        int STEPS = Integer.valueOf(string_SETPS);//total number of iterations
        int NUM_SAMPLE = Integer.valueOf(string_s);
        double energy = Double.valueOf(string_energy);
        double ini_energy = energy;
        double ini_energy_barrier = Double.valueOf(string_energy_barrier);

        boolean stop = false;
        double variance = b_r.diff;
        int no_change = 0;
        while(!stop){
           int variable = rand.nextInt(4);
           switch (variable){
              case 0: //k
              {
                 int temp = r.nextInt(2);
                 if (temp == 0) {
                    if ((NUM_SAMPLE + 1) <= 10000) {
                       NUM_SAMPLE++;
                    }
                 } else if (temp == 1) {
                    if (NUM_SAMPLE > 1) {
                       NUM_SAMPLE--;
                    }
                 }
                 generate_simulation(L, STEPS, NUM_SAMPLE, NUM, ini_energy, ini_energy_barrier, b_r);
                 break;
```

```
            }
            case 1: //collision
            {
               int temp = r.nextInt(2);
               if (temp == 0) {
                  STEPS += 8;
               }
               else{
                  if (STEPS - 8 > 0) {
                     STEPS -= 8;
                  }
               }
               generate_simulation(L, STEPS, NUM_SAMPLE, NUM, ini_energy,
ini_energy_barrier, b_r);
               break;
            }
            case 2: //energy
            {
               int temp = r.nextInt(2);
               if (temp == 0) {
                  ini_energy += 0.01;
               }
               else {
                  if (ini_energy - 0.01 > 0) {
                     ini_energy -= 0.01;
                  }
               }
               generate_simulation(L, STEPS, NUM_SAMPLE, NUM, ini_energy,
ini_energy_barrier, b_r);
               break;
            }
            case 3: //energy_barrier
            {
               int temp = r.nextInt(2);
               if (temp == 0) {
                  ini_energy_barrier += 0.01;
               }
               else {
                  if (ini_energy_barrier - 0.01 > 0) {
                     ini_energy_barrier -= 0.01;
                  }
               }
               generate_simulation(L, STEPS, NUM_SAMPLE, NUM, ini_energy,
ini_energy_barrier, b_r);
               break;
```

```
                }
                default:
                    break;
            }

            double latest_variance = b_r.diff;
            if(latest_variance >= variance){
                no_change++;
                if(no_change >= 1){
                    stop = true;
                    System.out.println("Variance not changed more than 1000 times... Stopping
now...");
                    try{
                        Thread.sleep(2000);
                    }
                    catch (Exception ex){
                        ex.printStackTrace();
                    }
                }
            }
            else{
                variance = latest_variance;
                no_change = 0;
            }
        }


        //output the best running result
        for (int i = 0; i < b_r.result1.size(); i++) {
            System.out.println("Set1 at collision " + b_r.result1.get(i).round + " M=" +
b_r.result1.get(i).M
                    + " N=" + b_r.result1.get(i).N + " L=" + b_r.result1.get(i).L + " K=" +
b_r.result1.get(i).K + " COLLISION=" + b_r.result1.get(i).COLLISION);
        }

        System.out.printf("The best result with variation %f\n", variance);
        System.out.printf("The energy is  %f\n", b_r.enery_E);
        System.out.printf("The energy barrier is %f\n", b_r.enery_barrier);

        if(b_r.result1.size() > 0) {
            for (int i = 0, j = 3; i < b_r.best_result.length && j >= 0; i++, j--) {
                System.out.println("Set 1 at collision " + (b_r.best_result[i].COLLISION / (int)
Math.pow(2, j)) + " M=" + b_r.best_result[i].M +
                        " N=" + b_r.best_result[i].N + " L=" + b_r.best_result[i].L + " K=" +
b_r.result1.get(i).K + " COLLISION=" + b_r.result1.get(i).COLLISION);
```

```
            }
        }
    }
}
```

APPENDIX II

JOHN WILEY AND SONS LICENSE TERMS AND CONDITIONS

Feb 21, 2018

This Agreement between Yijia Liu ("You") and John Wiley and Sons ("John Wiley and Sons") consists of your license details and the terms and conditions provided by John Wiley and Sons and Copyright Clearance Center.

License Number	4293710896451
License date	Feb 21, 2018
Licensed Content Publisher	John Wiley and Sons
Licensed Content Publication	International Journal of Energy Research
Licensed Content Title	Tin-based materials as negative electrodes for Li-ion batteries: Combinatorial approaches and mechanical methods
Licensed Content Author	A. D. W. Todd,P. P. Ferguson,M. D. Fleischauer,J. R. Dahn
Licensed Content Date	Jan 14, 2010
Licensed Content Pages	21
Type of use	Dissertation/Thesis
Requestor type	University/Academic
Format	Print and electronic
Portion	Figure/table
Number of figures/tables	22
Original Wiley figure/table number(s)	Figure 22
Will you be translating?	No
Title of your thesis / dissertation	Graduate Student
Expected completion date	Mar 2018
Expected size (number of pages)	1
Requestor Location	Yijia Liu Apt 718 5885 Spring Garden Rd Halifax, NS B3H1Y3 Canada Attn:
Publisher Tax ID	EU826007151
Total	0.00 CAD

SPRINGER NATURE LICENSE
TERMS AND CONDITIONS

Feb 21, 2018

This Agreement between Yijia Liu ("You") and Springer Nature ("Springer Nature") consists of your license details and the terms and conditions provided by Springer Nature and Copyright Clearance Center.

License Number	4293711328893
License date	Feb 21, 2018
Licensed Content Publisher	Springer Nature
Licensed Content Publication	Nature Reviews Materials
Licensed Content Title	Promise and reality of post-lithium-ion batteries with high energy densities
Licensed Content Author	Jang Wook Choi, Doron Aurbach
Licensed Content Date	Mar 31, 2016
Licensed Content Volume	1
Licensed Content Issue	4
Type of Use	Thesis/Dissertation
Requestor type	academic/university or research institute
Format	print and electronic
Portion	figures/tables/illustrations
Number of figures/tables/illustrations	1
High-res required	no
Will you be translating?	no
Circulation/distribution	<501
Author of this Springer Nature content	no
Title	Graduate Student
Instructor name	M.N. Obrovac
Institution name	Dalhousie University
Expected presentation date	Mar 2018
Portions	Figure 2

Copyright Clearance Center

Note: Copyright.com supplies permissions but not the copyrighted content itself.

1 PAYMENT 2 REVIEW 3 CONFIRMATION

Step 3: Order Confirmation

Thank you for your order! A confirmation for your order will be sent to your account email address. If you have questions about your order, you can call us 24 hrs/day, M-F at +1.855.239.3415 Toll Free, or write to us at info@copyright.com. **This is not an invoice.**

Confirmation Number: 11700314
Order Date: 02/21/2018

If you paid by credit card, your order will be finalized and your card will be charged within 24 hours. If you choose to be invoiced, you can change or cancel your order until the invoice is generated.

Payment Information

Yijia Liu
yj441392@dal.ca
+1 (902) 995-0301
Payment Method: n/a

Order Details

Journal of the Electrochemical Society

Order detail ID:	71028263
Order License Id:	4293670135457
ISSN:	0013-4651
Publication Type:	Journal
Volume:	
Issue:	
Start page:	
Publisher:	ELECTROCHEMICAL SOCIETY,
Author/Editor:	ELECTROCHEMICAL SOCIETY

Permission Status: Granted

Permission type: Republish or display content
Type of use: Republish in a thesis/dissertation

Requestor type	Academic institution
Format	Electronic
Portion	chart/graph/table/figure
Number of charts/graphs/tables/figures	1
The requesting person/organization	Yijia Liu
Title or numeric reference of the portion(s)	Figure 9 from "A.M. Wilson, J.R. Dahn, J. Electrochem. Soc. 142 (1995) 326."
Title of the article or chapter the portion is from	N/A

Copyright Clearance Center

Confirmation Number: 11700312
Order Date: 02/21/2018

Customer Information

Customer: Yijia Liu
Account Number: 3001252150
Organization: Yijia Liu
Email: yj441392@dal.ca
Phone: +1 (902) 995-0301
Payment Method: Invoice

This is not an invoice

Order Details

Journal of the Electrochemical Society

Billing Status: **N/A**

Order detail ID:	71028257
ISSN:	0013-4651
Publication Type:	Journal
Volume:	
Issue:	
Start page:	
Publisher:	ELECTROCHEMICAL SOCIETY,
Author/Editor:	ELECTROCHEMICAL SOCIETY

Permission Status: Granted

Permission type: Republish or display content
Type of use: Republish in a thesis/dissertation
Order License Id: 4293661339201

Requestor type	Academic institution
Format	Electronic
Portion	chart/graph/table/figure
Number of charts/graphs/tables/figures	1
The requesting person/organization	Dalhousie University
Title or numeric reference of the portion(s)	Figure 1 from "M.N. Obrovac, L.J. Krause, J. Electrochem. Soc. 154 (2007) A103."
Title of the article or chapter the portion is from	N/A
Editor of portion(s)	N/A
Author of portion(s)	M. N. Obrovac and L. J. Krause
Volume of serial or monograph	154
Issue, if republishing an article from a serial	2
Page range of portion	A103
Publication date of portion	2007
Rights for	Main product
Duration of use	Current edition and up to 5 years
Creation of copies for the disabled	yes
	yes

Copyright Clearance Center

Confirmation Number: 11700307
Order Date: 02/21/2018

Customer Information

Customer: Yijia Liu
Account Number: 3001252150
Organization: Yijia Liu
Email: yj441392@dal.ca
Phone: +1 (902) 995-0301
Payment Method: Invoice

This is not an invoice

Order Details

Journal of the Electrochemical Society

Billing Status: **N/A**

Order detail ID:	71028249
ISSN:	0013-4651
Publication Type:	Journal
Volume:	
Issue:	
Start page:	
Publisher:	ELECTROCHEMICAL SOCIETY,
Author/Editor:	ELECTROCHEMICAL SOCIETY

Permission Status: Granted

Permission type: Republish or display content
Type of use: Republish in a thesis/dissertation
Order License Id: 4293660690495

Requestor type	Academic institution
Format	Electronic
Portion	chart/graph/table/figure
Number of charts/graphs/tables/figures	3
The requesting person/organization	Yijia Liu
Title or numeric reference of the portion(s)	Figure 6 in Alloy Design for Lithium-Ion Battery Anodes
Title of the article or chapter the portion is from	N/A
Editor of portion(s)	N/A
Author of portion(s)	Obrovac, M. N. Christensen, Leif Le, Dinh Ba Dahn, J. R.
Volume of serial or monograph	154
Issue, if republishing an article from a serial	9
Page range of portion	A853
Publication date of portion	2007
Rights for	Main product
Duration of use	Current edition and up to 5 years
Creation of copies for the disabled	yes
	yes